UNIVERSITÄT PADERBORN
Die Universität der Informationsgesellschaft

FAKULTÄT FÜR
ELEKTROTECHNIK,
INFORMATIK UND
MATHEMATIK

Fast Endless Polarization Control for Optical Communication Systems

Zur Erlangung des akademischen Grades

DOKTORINGENIEUR (Dr.-Ing.)

der Fakultät für Elektrotechnik, Informatik und Mathematik
der Universität Paderborn
vorgelegte Dissertation
von

Ariya Hidayat, M.Eng.
Surabaya (Indonesien)

Referent: Prof. Dr.-Ing. Reinhold Noé
Korreferent: Prof. Dr.-Ing. Rolf Schuhmann

Tag der mündlichen Prüfung: 04.09.2008

Paderborn, den 15.9.2008

Diss. EIM-E/243

Abstract

Automatic endless polarization controllers are important components for polarization division multiplex receivers, PMD (polarization-mode dispersion) compensators, coherent optical receivers, optical fiber sensors and switches, as well as other optical interferometric solutions. High-speed polarization changes in the transmission fibers must be tracked, without any interruption, in order to realize a near-perfect polarization matching. Thus, fast polarization controllers typically use electro-optic polarization transformers which currently offer the fastest response time.

In this work, a method to characterize commercial multistage polarization transformers has been investigated. It has been developed based on a quaternion analysis of the optical retarders. The polarization transformation of the retarder can be inferred accurately using a quaternion-based optimization on series of polarimetric measurement data. Based on the calibration result, the electro-optic polarization transformers can be calibrated and operated as linear retarders or fractional waveplates with a high degree of accuracy, already taking into account any of retarder's non-ideal characteristics.

The electro-optic retarders have been used in a polarization control system. The hardware for the system has been developed using affordable commercial off-the-shelf components. The characteristics and the performance of two polarization control algorithms have been extensively studied. An ultra-fast implementation of the linear retarder algorithm, running on an FPGA (field programmable gate array), has been realized and tested in a polarization tracking experiment. The retarder calibration data are stored as look-up tables for very fast access. The implementation of the control algorithm has been optimized, reaching a control iteration cycle of just 2 µs. In the tracking experiments, it was found that the controller was able to track up to 15000 rad/s polarization changes caused by rotating waveplates with the maximum polarization mismatch of only 0.14 rad, corresponding to a negligible intensity fluctuation of 0.02 dB. Truly endless operation was confirmed in a long term experiment. This polarization controller is thus suitable for polarization demultiplexing and PMD compensation.

Zusammenfassung

Automatische, endlose Polarisationsregelung ist ein wichtiger Bestandteil in Empfängern mit optischem Polarisationsdemultiplex, PMD-Kompensatoren (Polarisationsmodendispersion), kohärenten optischen Empfängern, faseroptischen Sensoren und Schaltern, sowie in anderen optisch interferometrischen Lösungen. Schnelle Polarisationsänderungen in der Übertragungsfaser müssen ohne Unterbrechungen nachverfolgt werden, um eine nahezu perfekte Übereinstimmung der Polarisationen zu erreichen. Typischerweise werden zur Polarisationsregelung elektrooptische Polarisationstransformatoren verwendet, um kurze Reaktionszeiten zu erreichen.

In dieser Arbeit wurde eine Methode zur Charakterisierung kommerzieller, mehrstufiger Polarisationstransformatoren auf Basis einer Quaternion-Analyse der optischen Retarder entwickelt. Die Polarisationtransformation der Retarder kann mithilfe einer Quaternion-Optimierung aus den gemessenen Polarisationsdaten gewonnen werden. Mit den Ergebnissen dieser Kalibrierung lassen sich die elektrooptischen Polarisationstransformatoren mit hoher Genauigkeit als lineare Retarder oder Wellenplatten betrieben, wobei die nichtidealen Charakteristiken der Retarder schon berücksichtigt werden.

Die elektrooptischen Retarder wurden in einem Polarisationregelsystem verwendet. Die Hardware dieses Systems wurde aus günstigen, kommerziellen Standardkomponenten entwickelt. Die Eigenschaften und Leistungsmerkmale zweier Polarisationsregelalgorithmen wurden ausführlich untersucht. Eine sehr schnelle Implementierung eines Regelalgorithmus für lineare Retarder wurde auf einem FPGA (field programmable gate array) realisiert und in einem Experiment überprüft. Die Daten aus der Retarderkalibrierung wurden für den schnellen Zugriff in Look-Up-Tabellen abgespeichert. Die Implementierung des Regelalgorithmus wurde optimiert und eine Ausführungszeit von nur 2 µs erreicht. Experimentell wurde herausgefunden, dass der Regler Polarisationsänderungen, die durch rotierende Wellenplatten verursacht wurden, bis zu einer Geschwindigkeit von 15000 rad/s mit einer maximalen Polarisationsabweichung von nur 0,14 Radiant, entsprechend eines geringen Intensitätsverlustes von 0,02 dB, nachverfolgen konnte. Echte endlose Regelung wurde durch ein Langzeitexperiment bestätigt. Damit erreicht dieser Polarisationsregler die Anforderungen von Polarisationsdemultiplex und PMD-Kompensation.

Publications

This dissertation is the result of collaborative research on the polarization aspects and advance modulation formats in optical communications systems, which have been published in various journals and conferences. Here is a list of relevant publications with the author's participation.

Conference Papers

1. B. Koch, **A. Hidayat**, H. Zhang, V. Mirvoda, M. Lichtinger, D. Sandel, R. Noé, "12 krad/s Endless Polarization Stabilization with Lithium Niobate Component", *IEEE LEOS Summer Topical 2008*, 21-23 July 2008, Acapulco, Mexico, Paper TuD2.4

2. B. Koch, **A. Hidayat**, H. Zhang, V. Mirvoda, M. Lichtinger, D. Sandel, R. Noé, "FPGA-basierte schnelle endlose Polarisationregelung mit Lithiumniobatbauelement", *9. ITG-Fachtagung Photonische Netze*, 28-29 April 2008, Leipzig, Germany

3. **A. Hidayat**, B. Koch, V. Mirvoda, H. Zhang, S. Bhandare, S.K. Ibrahim, D. Sandel, R. Noé, "Fast Optical Endless Polarization Tracking with $LiNbO_3$ Component", *Optical Fiber Communication Conference (OFC 2008)*, 24-28 February 2008, San Diego, USA, Paper JWA28

4. A. F. Abas, **A. Hidayat**, D. Sandel, S. Bhandare, R. Noé, "2.38 Tb/s (16×160 Gb/s) WDM Transmission over 292 km of fiber with 100 km EDFA-spacing and No Raman Amplification", *European Conference on Optical Communication (ECOC 2006)*, Cannes, France, 24-28 September 2006, Paper Tu1.5.2

5. H. Zhang, A. Fauzi Abas, **A. Hidayat**, D. Sandel, S. Bhandare, F. Wüst, B. Milivojevic, R. Noé, M. Lapointe, Y. Painchaud, M. Guy, "Tunable Dispersion Compensation Experiment in 5.94 Tb/s WDM Transmission System", *Asia-Pacific Optical Communications Conference (APOC 2005)*, 6–10 November 2005, Shanghai, China, Session 3a, Paper 6021-20

6. **A. Hidayat**, A. Fauzi Abas, D. Sandel, S. Bhandare, H. Zhang, F. Wüst, B. Milivojevic, R. Noé, M. Lapointe, Y. Painchaud, M. Guy, "5.94 Tb/s capacity of a multichannel tunable -700 to -1200 ps/nm dispersion compensator", *European Conference on Optical Communication (ECOC 2005*), 25-29 September 2005, Glasgow, Scotland, Paper We1.2.5

7. **A. Hidayat**, S. Bhandare, D. Sandel, A. Fauzi Abas, H. Zhang, B. Milivojevic, R. Noé, M. Guy, M. Lapointe, "Adaptive 700...1350 ps/nm chromatic dispersion compensation in 1.6 Tbit/s (40×40 Gbit/s) DPSK and ASK transmission experiments over 44...81 km of SSMF", *6. ITG-Fachtagung Photonische Netze*, 2-3 May 2005, Leipzig, Germany

8. B. Milivojevic, A. Fauzi Abas, **A. Hidayat**, S. Bhandare, D. Sandel, R. Noé, M. Guy, M. Lapointe, "160 Gbit/s, 1.6 bit/s/Hz RZ-DQPSK Polarization- Multiplexed Transmission over 230 km Fiber with TDC", *European Conference on*

Optical Communication (ECOC 2004), September 5-9, 2004, Stockholm, Sweden, Paper We1.5.5

9. A. Fauzi Abas Ismail, D. Sandel, **A. Hidayat**, B. Milivojevic, S. Bhandare, H. Zhang, R. Noé, "2.56 Tbit/s, 1.6 bit/s/Hz, 40 Gbaud RZ-DQPSK polarization division multiplex transmission over 273 km of fiber", *Ninth Optoelectronics and Communications Conference/Third International Conference on Optical Internet (OECC/COIN 2004)*, Yokohama, Japan, July 12-16, 2004, Paper PD1-4

Journal Papers

1. **A. Hidayat**, B. Koch, V. Mirvoda, H. Zhang, M. Lichtinger, D. Sandel and R. Noé, "Optical 5 krad/s Endless Polarisation Tracking", *IEE Electronics Letters*, Vol. 44, No. 8, pp. 546-548, 2008

2. B. Koch, **A. Hidayat**, H. Zhang, V. Mirvoda, M. Lichtinger, D. Sandel, R. Noé, "Optical Endless Polarization Stabilization at 9 krad/s with FPGA-Based Controller", *IEEE Photonics Technology Letters,* Vol. 20, 2008, pp. 961-963

3. **A. Hidayat**, A. Fauzi Abas, D. Sandel, S. Bhandare, H. Zhang, F. Wüst, B. Milivojevic, R. Noé, M. Lapointe, Y. Painchaud, M. Guy, "5.94 Tb/s (40×2×2×40 Gbit/s) capacity of FBG-based multichannel tunable -700 to -1200 ps/nm dispersion compensator", *Journal of Optical Communications*, Vol. 27, 2006, No. 1, pp. 17-19

4. A. Fauzi Abas, **A. Hidayat**, D. Sandel, B. Milivojevic, R. Noè, "100 km fiber span in 292 km, 2.38 Tb/s (16×160 Gb/s) WDM DQPSK polarization division multiplex transmission experiment without Raman amplification", *Optical Fiber Technology*, 13 (2007) 46-50

5. A.F. Abas, B. Milivojevic, **A. Hidayat**, S. Bhandare, D. Sandel, H. Zhang, R. Noé, "2.38 Tbit/s, 1.49 bit/s/Hz (16×4×40 Gbit/s) RZ-DQPSK polarization division multiplex transmission over 273 km of fiber", *Electrical Engineering*, 6 July 2005

6. B. Milivojevic, A. F. Abas, **A. Hidayat**, S. Bhandare, D. Sandel, R. Noé, M. Guy, M. Lapointe, "1.6-bit/s/Hz, 160-Gbit/s, 230-km RZ-DQPSK Polarization Multiplex Transmission with Tunable Dispersion Compensation", *IEEE Photonics Technology Letters*, Vol. 17, 2005, pp. 495-497

List of Figures

Symbols and Abbreviations

Symbols

θ	azimuth of polarization ellipse
ϵ	ellipticity of polarization ellipse
$\mathbf{S}$	Stokes vector
$\mathbf{J}$	Jones matrix
$\mathbf{M}$	Mueller matrix
$\mathbf{G}$	reduced Mueller matrix
$\mathbf{\Omega}$	rotation axis
φ	phase retardation
ψ	eigenmode orientation
γ	fast axis angle
$\mathcal{Q}$	quarter-wave plate quaternion
$\mathcal{H}$	half-wave plate quaternion
$\mathcal{L}$	linear retarder quaternion
$\mathcal{P}$	phase shifter quaternion
M	mode converter quaternion
C	circular retarder quaternion

Abbreviations

ADC	Analog-to-Digital Converter
BER	Bit Error Rate
DAC	Digital-to-Analog Converter
DPSK	Differential Phase-Shift Keying
DQPSK	Differential Quadrature Phase-Shift Keying
FEC	Forward Error Correction
FPGA	Field Programmable Gate Array
HWP	Half-Wave Plate
NRZ	Non Return-to-Zero
PBS	Polarization Beam Splitter
PMD	Polarization Mode Dispersion
RAM	Random Access Memory
RUT	Retarder Under Test
RZ	Return-to-Zero
SDRAM	Synchronous Dynamic RAM
VGA	Video Graphics Array
VHDL	VHSIC Hardware Description Language
VHSIC	Very-High-Speed Integrated Circuits
WDM	Wavelength-Division Multiplexing

Contents

Chapter 1

Introduction

Fiber-optic communication systems are now ubiquitous in the long-haul, metro and access networks. The world's current and future telecommunication structures rely on the optical networks deployed world-wide. The increased usage and demand for Internet multimedia rich applications certainly means a traffic growth in all network areas. The next generation of optical communication system is expected to fulfill this demand by pushing the performance to achieve a high capacity and highly efficient transmission.

In a wavelength-division multiplexing (WDM) system, more than one optical carrier with different wavelengths is modulated and transmitted together in a single optical fiber [1]. Using this technology, the transmission capacity is multiplied by the number of the transmitted channels. Erbium-doped fiber amplifiers (EDFA) allow all these WDM channels to be amplified optically and thereby eliminates the need for the expensive per-channel regeneration. With a total of 273 channels, a transmission capacity of 10.92 Tb/s has been demonstrated [2].

A further increase in the transmission capacity can be reached by using spectrally-efficient modulation formats. With differential quadrature phase-shift keying (DQPSK), two bits per symbol are transmitted resulting in the doubling of the channel capacity [3, 4, 5]. A total capacity of 6 Tb/s in 151 DQPSK channels has been demonstrated [6]. Further capacity doubling is possible by using polarization division multiplexing (PolDM) where two modulated signals are launched in two orthogonal polarizations [7, 8]. The combination of both proves to be an effective way to quadruple the bit rate [9, 10]. At 40 Gbaud, this corresponds to a 160 Gb/s channel capacity (Appendix C). A record-breaking 25.6 Tb/s capacity has been reported using 160 channels of polarization multiplexed DQPSK signals [11]. Beside the potentials, there is also a big challenge in implementing a receiver for polarization-multiplexed signals, namely to properly perform the demultiplexing because the state of polarization of the signals likely changes during the transmission. A fully automatic polarization demultiplexer therefore needs to track any polarization fluctuations in the transmission fiber, ideally fast enough so that the two polarization channels can be demodulated properly. Crosstalk between the polarization channels occurs where there is a non-negligible polarization mismatch.

Coherent optical detection is attractive due to its better sensitivity compared to the direct detection method. In a coherent receiver, the received signal and the local oscillator signal are combined in an interferometer, which means that polarization matching between the received signal and its local oscillator is critical [12]. One of the methods to ensure polarization matching is to use a polarization controller [13] which continuously adjusts the polarization state of the local oscillator signal to match that of the received signal. Since the received signal is subject to polarization rotations along the fiber, the speed requirement of the controller is high because it must be capable of tracking fast polarization changes. Even a short period of polarization mismatch may cause a loss of data. In addition, other optical components which rely on the interferometric method, such as fiber sensors, photonic switches, and all-optical regenerators, also have the prob-

lem of polarization dependence. This problem is solved either by using polarization insensitive devices or an automatic polarization controller.

Faster modulation techniques may bring the bit rate further towards 100 Gb/s or more [14]. At this very high bit rate, optical signal impairment due to the polarization-mode dispersion (PMD) becomes one of the major obstacles [15, 16] and therefore necessitates the use of PMD compensators. A distributed PMD compensator comprises a number of differential group delay (DGD) sections with a polarization transformer in between [17]. The PMD is equalized when the PMD compensator "mirrors" the DGD vectors of the fiber. Since PMD is a stochastic phenomenon, inherently instantaneous DGD can change within a period of as short as few milliseconds to as long as a few days. The PMD compensator must adjust the polarization transformers to track these changes.

Fast, automatic endless polarization controllers are arguably important components for future optical communication systems. Many polarization control experiments have been reported in the last two decades. Earlier experiments made use of slow mechanical (or electro-mechanical) polarization transformers which limit their actual applications. Electro-optic retardation waveplates currently offer the best response time and hence quickly become the natural choice as the control elements for fast polarization stabilization. The control algorithm is generally implemented in a digital circuit for the fastest possible execution. Ideally the polarization controller should be as fast, if not faster, than the microsecond timescale polarization changes in the fiber trunk that have been observed in field trials [18, 19].

The motivation behind this work is to realize an ultra-fast automatic polarization controller suitable for polarization demultiplexing and PMD compensation. For practical reasons, the controller employs commercial electro-optic polarization transformers and other standard, off-the-shelf components. Its fast operation is achieved by implementing the control algorithm in configurable hardware. The performance of the controller is analyzed when it stabilizes rapidly varying random polarization states. Because it is intended to be used for polarization demultiplexing, the polarization mismatch must be as low as possible.

The rest of this dissertation is organized as follows. In Chapter 2, the working principle of the electro-optic retarder, an important control element for a fast polarization control system, is described. Non-ideal characteristics of such a retarder must be analyzed and properly compensated, and a practical method to perform the characterization and calibration is presented. In Chapter 3, a detailed mathematical analysis of important endless polarization control algorithms is given. The architecture and implementation for a hardware-based digital controller for polarization stabilization are investigated. The performance of the controller is experimentally analyzed. Finally, Chapter 4 concludes the dissertation.

Chapter 2

Characterization of Electro-Optic Linear Retarders

2.1 Polarization Transformers

A transverse monochromatic lightwave which propagates in the z direction, denoted as $E(z,t)$, can be represented as the vector sum of two perpendicular fields $E_x(z,t)$ and $E_y(z,t)$, with

$$\begin{aligned} E_x(z,t) &= \hat{\mathbf{x}} E_{0,x} e^{j(\omega t - kz)}, \\ E_y(z,t) &= \hat{\mathbf{y}} E_{0,y} e^{j(\omega t - kz + \varphi)}, \end{aligned} \tag{2.1}$$

where k is the propagation constant, ω is the frequency, and φ is the relative phase difference between the fields.

The *state of polarization* of the lightwave is described by the *polarization ellipse* (figure 2.1) which is the path traced by the end of real part of $E(z,t)$, as seen by an observer looking towards $z = -\infty$ [20]. This ellipse is characterized by the angle of the major axis of the ellipse to the $x-$axis, denoted as θ, and the ratio between the major axis and minor axis, denoted as ϵ. They are often called the *azimuth* and *ellipticity* of the polarization ellipse, respectively. If a and b are half of the length of the major axis and minor axis of the polarization ellipse, then it holds

$$\tan \epsilon = \pm \frac{b}{a}, \tag{2.2}$$

with the sign $\pm$ describes the direction of the movement (clockwise or counterclockwise) of the real part of $E(z,t)$.

For a linearly polarized wave, the phase difference between $E_x(z,t)$ and $E_y(z,t)$ is $2n\pi$ where $n = 0, 1, 2, 3, \ldots$, $\epsilon = 0$ and the polarization ellipse is reduced to a line with an angle of θ to the $x-$axis. Special cases of linear polarization are horizontal polarization ($\theta = 0$), vertical polarization ($\theta = \pi/2$), $+45°$polarization ($\theta = \pi/4$), and $-45°$polarization ($\theta = -\pi/4$).

For a circularly polarized wave, the phase difference between $E_x(z,t)$ and $E_y(z,t)$ is $\pm\pi/2 + 2n\pi$ where $n = 0, 1, 2, 3, \ldots$. In this case, the major axis and the minor axis of the ellipse are of the same length and therefore the ellipse becomes a circle, regardless of the azimuth θ. The two cases of circular polarizations are right circular polarization ($\varphi = -\pi/2 + 2n\pi$) and left circular polarization ($\varphi = \pi/2 + 2n\pi$).

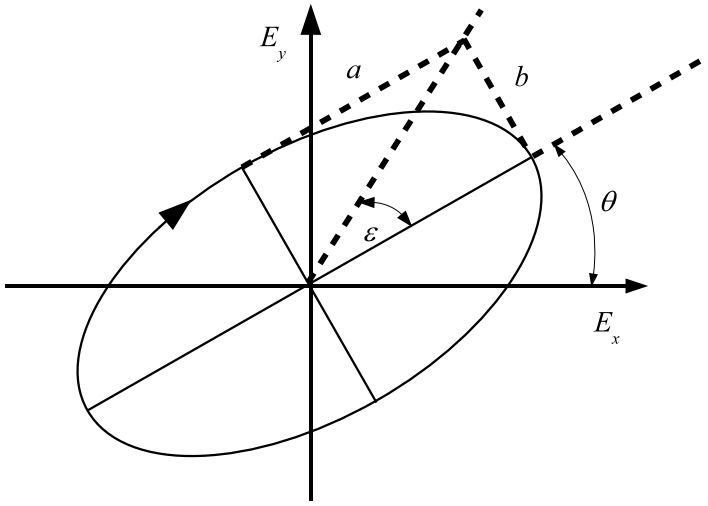

Figure 2.1: Polarization ellipse

2.1.1 Representations of Polarization Transformations

Jones Vector and Stokes Vector

In equation 2.1, generally the factor $e^{j(\omega t - kz)}$ describes the propagation of the wave and therefore does not affect the shape of the polarization ellipse. Dropping this factor allows the polarization state to be represented by the *Jones vector* [21]

$$\mathbf{E} = \begin{bmatrix} E_{0,x}(t)e^{j\varphi_x} \\ E_{0,y}(t)e^{j\varphi_y} \end{bmatrix}, \tag{2.3}$$

where $E_{0,x}(t)$ and $E_{0,y}(t)$ are the instantaneous scalar components of $\mathbf{E}$ and φ_x and φ_y are the phase of each x and y components. For polarization analysis, only the relative magnitude and phase difference between x and y components are important. The Jones vector can be normalized by dividing it with $|\mathbf{E}|\, e^{j\varphi}$ which yields $\begin{bmatrix} E_x & E_y \end{bmatrix}^T$ with $|E_x|^2 + |E_y|^2 = 1$. Sometimes the normalized Jones vector is written with the imaginary part of E_x chosen to be 0.

General elliptical polarization with an azimuth of θ and an ellipticity of ϵ can be described by the normalized Jones vector [20]

$$\mathbf{E} = \begin{bmatrix} \cos\theta\cos\epsilon + j\sin\theta\sin\epsilon \\ \sin\theta\cos\epsilon - j\cos\theta\sin\epsilon \end{bmatrix}. \tag{2.4}$$

Another way to represent the state of polarization is by using the *Stokes vector* [22]. A monochromatic lightwave with the Jones vector $\begin{bmatrix} E_x & E_y \end{bmatrix}^T$ has the corresponding Stokes vector

$$\mathbf{S} = \begin{bmatrix} S_0 \\ S_1 \\ S_2 \\ S_3 \end{bmatrix} = \begin{bmatrix} \left\langle |E_x|^2 + |E_y|^2 \right\rangle \\ \left\langle |E_x|^2 - |E_y|^2 \right\rangle \\ \left\langle 2\Re(E_x E_y^*) \right\rangle \\ \left\langle 2\Im(E_x E_y^*) \right\rangle \end{bmatrix}, \tag{2.5}$$

where $\langle\cdot\rangle$ denotes the averaging operator. The elements S_0, S_1, S_2, S_3 are also known as the *Stokes parameters*. Dividing the Stokes parameters by S_0 yields the normalized

Stokes vector ($S_0 = 1$ and is often dropped). Although a normalized Stokes vector consists of three elements, it has only two degree-of-freedom because (for fully polarized light) $S_1^2 + S_2^2 + S_3^2 = 1$.

General elliptical polarization with an azimuth of θ and an ellipticity of ϵ can be described by the normalized Stokes vector

$$\mathbf{S} = \begin{bmatrix} \cos 2\epsilon \cos 2\theta \\ \cos 2\epsilon \sin 2\theta \\ \sin 2\epsilon \end{bmatrix}. \tag{2.6}$$

Jones Matrix and Mueller Matrix

If a lightwave passes a lossless optical medium, its state of polarization may change. The polarization transformation can be described mathematically using *Jones matrix* [21] or *Mueller matrix* [23].

Using a complex 2×2 Jones matrix $\mathbf{J}$, an input polarization $\mathbf{E_i}$ is transformed into the output state $\mathbf{E_o}$ according to

$$\mathbf{E_o} = \mathbf{J}\mathbf{E_i}. \tag{2.7}$$

If the Stokes vectors for input polarization and output polarization are denoted as $\mathbf{S_i}$ and $\mathbf{S_o}$, respectively, then using a real 4×4 Mueller matrix $\mathbf{M}$, the polarization transformation can be written as

$$\mathbf{S_o} = \mathbf{M}\mathbf{S_i}. \tag{2.8}$$

For normalized Stokes vectors $\mathbf{S_i}$ and $\mathbf{S_o}$, the transformation matrix is simplified to a real 3×3 reduced Mueller matrix $\mathbf{G}$, where again

$$\mathbf{S_o} = \mathbf{G}\mathbf{S_i}. \tag{2.9}$$

If the elements of Mueller matrix $\mathbf{M}$ and reduced Mueller matrix $\mathbf{G}$ are denoted as m_{ij} $(i, j = 0, 1, 2, 3)$ and g_{ij} $(i, j = 0, 1, 2)$, then it holds

$$g_{ij} = m_{i+1,j+1}. \tag{2.10}$$

Generally, the reduced Mueller matrix $\mathbf{G}$ describes a rotation in the Stokes space. For an optical medium which has an eigenmode of $\mathbf{\Omega} = [\ \Omega_\mathrm{x} \quad \Omega_\mathrm{y} \quad \Omega_\mathrm{z}\ ]^T$ and introduces phase difference of φ between the two transmitted eigenmodes, the reduced Mueller matrix $\mathbf{G}$ is obtained using Rodrigues' rotation formula

$$\mathbf{G} = \mathbf{I} + \widetilde{\mathbf{\Omega}} \sin\varphi + \widetilde{\mathbf{\Omega}}^2(1 - \cos\varphi), \tag{2.11}$$

with

$$\widetilde{\mathbf{\Omega}} = \begin{bmatrix} 0 & -\Omega_z & \Omega_y \\ \Omega_z & 0 & -\Omega_x \\ -\Omega_y & \Omega_x & 0 \end{bmatrix}, \tag{2.12}$$

which gives

$$\mathbf{G} = \begin{bmatrix} \Omega_x^2 + (\Omega_y^2 + \Omega_z^2)\cos\varphi & \Omega_x\Omega_y(1-\cos\varphi) - \Omega_z\sin\varphi & \Omega_x\Omega_z(1-\cos\varphi) + \Omega_y\sin\varphi \\ \Omega_x\Omega_y(1-\cos\varphi) + \Omega_z\sin\varphi & \Omega_y^2 + (\Omega_x^2 + \Omega_z^2)\cos\varphi & \Omega_y\Omega_z(1-\cos\varphi) - \Omega_x\sin\varphi \\ \Omega_x\Omega_z(1-\cos\varphi) - \Omega_y\sin\varphi & \Omega_y\Omega_z(1-\cos\varphi) + \Omega_x\sin\varphi & \Omega_z^2 + (\Omega_x^2 + \Omega_y^2)\cos\varphi \end{bmatrix}. \tag{2.13}$$

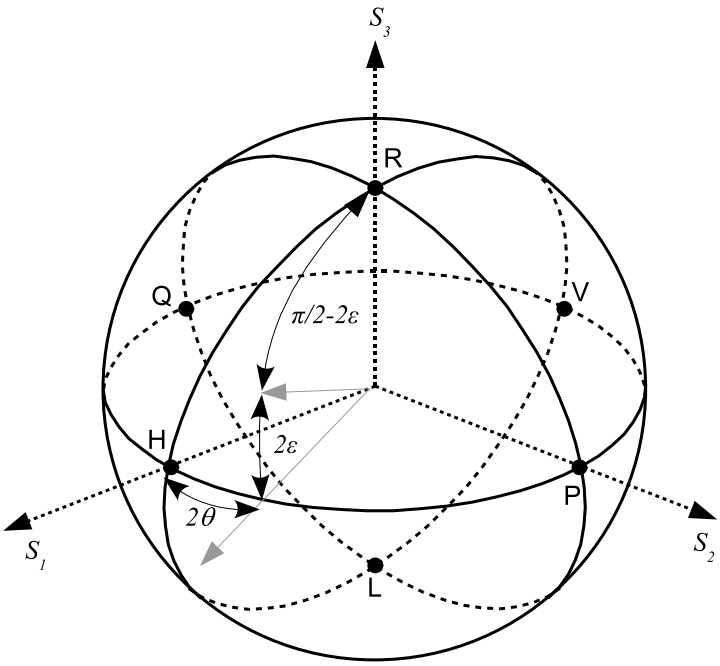

Figure 2.2: Poincaré sphere

For N cascaded optical medium $\mathbf{G_1}, \mathbf{G_2}, \mathbf{G_3}, \cdots, \mathbf{G_N}$, the total polarization transformation $\mathbf{G}$ is

$$\mathbf{G} = \mathbf{G_N} \cdots \mathbf{G_3 G_2 G_1}. \tag{2.14}$$

Poincaré Sphere

The three normalized Stokes parameters for an elliptical polarization with an azimuth of θ and an ellipticity of ϵ (equation 2.6) are the spherical coordinates of a point in a unit sphere with an azimuth of 2θ and a zenith of $\pi/2 - 2\epsilon$ [24]. The spherical surface occupied by elliptical polarization states is known as the *Poincaré sphere* (figure 2.2). Linear polarizations, such as horizontal polarization (H), vertical polarization (V), $+45°$ polarization (P), and $-45°$ polarization (Q), reside on the S_1S_2 great circle ("equator") while circular polarizations, right (R) and left (L), reside on the intersections of S_1S_3 and S_2S_3 great circles ("poles").

On the Poincaré sphere, the polarization transformation by the reduced Mueller matrix $\mathbf{G}$ can be visualized easily because geometrically it corresponds to a rotation. Figure 2.3 shows a transformation from polarization state A to B as a rotation φ around the axis $\mathbf{\Omega}$ (dashed arrow) with $\mathbf{G}$, φ, and $\mathbf{\Omega}$ as in equation 2.11.

Quaternion

There are several ways to represent a rotation mathematically: rotation angle and axis, transformation matrix, Euler angles and Hamilton's *quaternion* [25]. Throughout this dissertation, quaternion is extensively used for rotation analysis because of its simple representation and mathematical operations[1]. In addition, because polarization trans-

[1] Although, rather surprisingly, quaternion is hardly employed in literature on polarization analysis.

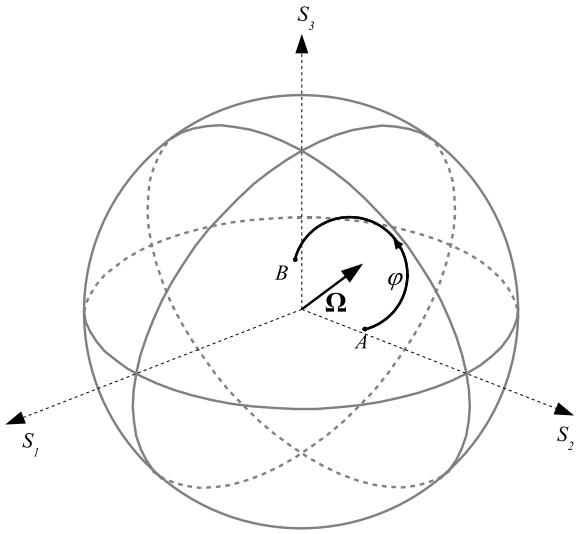

Figure 2.3: Polarization transformation as a rotation on the Poincaré sphere

formation analysis is often depicted on the Poincaré sphere, quaternion has also the advantage of a direct relation to the geometrical representation of the transformation.

Generalized polarization transformation which is equivalent to a rotation of φ around the axis $\mathbf{\Omega}$ on the Poincaré sphere can be described by the quaternion[2]

$$\mathcal{G} = \cos\frac{\varphi}{2} + \sin\frac{\varphi}{2}\mathbf{\Omega}. \tag{2.15}$$

Using this quaternion, the input polarization with the normalized Stokes vector $\mathbf{S_i}$ is transformed to the output polarization with normalized Stokes vector $\mathbf{S_o}$ according to (using equation A.13)

$$\mathbf{S_o} = \mathcal{G}\mathbf{S_i}\mathcal{G}^*. \tag{2.16}$$

2.1.2 Optical Retarders as Polarization Transformers

A *waveplate*, also known as *retarder*, has a fast and a slow axis. If a plane wave passes through a waveplate, the electrical field component along the fast axis propagates with a smaller refraction index compared to the component along the slow axis. This characteristic is known as *birefringence* or *double refraction* [26]. At the output of the waveplate, a relative phase (*retardation*) is introduced between the two components. It depends on the thickness of the waveplate. In a fractional waveplate, this phase delay is set to a fraction of the wavelength. The two most common fractional wave plates are quarter-wave plate and half-wave plate. If the axis of the waveplate can be freely rotated, it is often called a *rotatable* waveplate.

Quarter-wave plate

In a *quarter-wave plate*, the phase difference is $(4n+1)\pi/2$ with $n = 0, 1, 2, ...$, which corresponds to a delay of $(4n+1)\lambda/4$ where λ is the wavelength. The minimum delay is thus a quarter of the wavelength, hence the name. If γ denotes the angle between the a fast axis of a rotatable quarter-wave plate and the x-component of the field, then on

[2]To distinguish quaternions from other symbols, quaternions are printed out in calligraphic typeface.

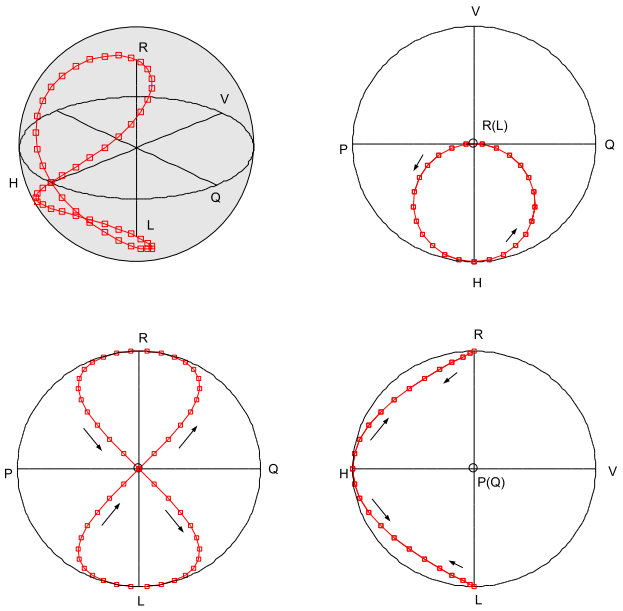

Figure 2.4: Transformation of horizontal polarization by a rotatable quarter-wave plate

the Poincaré sphere, the waveplate can be represented by a $\pi/2$ rotation around the axis $[\ \cos 2\gamma \quad \sin 2\gamma \quad 0\ ]^T$ or by the following unit quaternion

$$\mathcal{Q}(\gamma) = \frac{1}{2}\sqrt{2}(1 + \mathbf{i}\cos 2\gamma + \mathbf{j}\sin 2\gamma). \tag{2.17}$$

A rotatable quarter-wave plate can be used to transform a linear polarization to a circular polarization and vice versa. In addition, all elliptical polarization states can also be reached by a quarter-wave plate having certain linear polarization at its input. Figure 2.4 shows the trajectory of the result of horizontal polarization transformation by a rotatable waveplate $\mathcal{Q}(\gamma)$ for $\gamma = 0...\pi$. For other linear polarization states at the input, the trajectory is just rotated around the S_3 axis.

Half-wave plate

In a *half-wave plate*, the phase difference is $(2n+1)\pi$ with $n = 0, 1, 2, ...$, which corresponds to a delay of $(2n+1)\lambda/2$. The minimum delay is half of the wavelength. If γ denotes the angle between the fast axis of a rotatable half-wave plate and the x-component of the field then, on the Poincaré sphere, the waveplate can be represented by a π rotation around the axis $[\ \cos 2\gamma \quad \sin 2\gamma \quad 0\ ]^T$ or by the following unit quaternion

$$\mathcal{H}(\gamma) = \mathbf{i}\cos 2\gamma + \mathbf{j}\sin 2\gamma. \tag{2.18}$$

A rotatable half-wave plate can be used to transform a right circular polarization into a left circular or vice versa. Linear polarization states will remain linear when being passed to a rotatable half-wave plate, however both its Stokes components S_1 and S_2 will be changed. Figure 2.5 shows the trajectory of the transformation result of an elliptical polarization, denoted by the small circle, by a rotatable waveplate $\mathcal{H}(\gamma)$ for $\gamma = 0...\pi/5$.

A half-wave plate can be realized by cascading two quarter-wave plates with the same orientation axis. For $\mathcal{Q}(\gamma_2)\mathcal{Q}(\gamma_1)$ where $\gamma_2 = \gamma_1 = \gamma$, then it holds

$$\mathcal{H}(\gamma) = \mathcal{Q}(\gamma)\mathcal{Q}(\gamma). \tag{2.19}$$

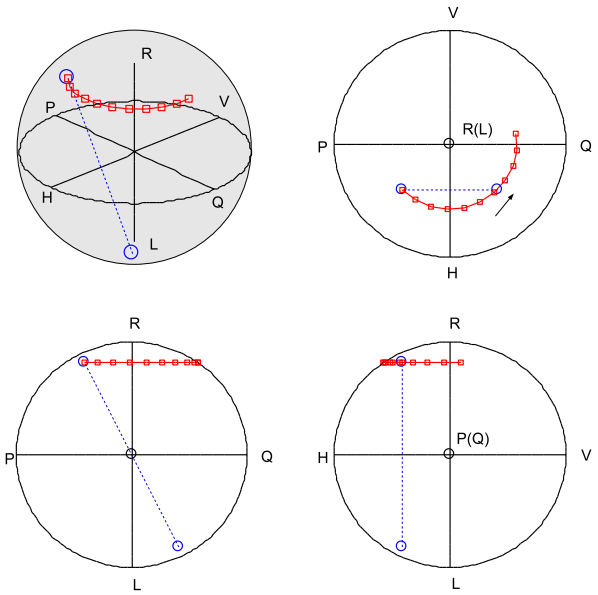

Figure 2.5: Transformation of elliptical polarization by a rotatable half-wave plate

Linear retarder

A *linear retarder* is a generalized form of half- or quarter-wave plates. It is characterized not only by the fast axis angle γ, but also by the retardation φ. On the Poincaré sphere, polarization transformation by a linear retarder is equivalent to a rotation of φ around the axis $[\ \cos 2\gamma \quad \sin 2\gamma \quad 0\ ]^T$. Thus, like the two fractional waveplates, the rotation axis of a linear retarder lies on the S_1S_2 plane. It also can be represented by the following unit quaternion

$$\mathcal{L}(\gamma,\varphi) = \cos\frac{\varphi}{2} + \mathbf{i}\sin\frac{\varphi}{2}\cos 2\gamma + \mathbf{j}\sin\frac{\varphi}{2}\sin 2\gamma. \tag{2.20}$$

It can be seen that quarter-wave plate and half-wave plate are just linear retarders with retardation of $-\pi/2$ and π respectively. This can be verified by substituting the retardation $\varphi = -\pi/2$ (for quarter-wave plate) and $\varphi = \pi$ (for half-wave plate) into the above equation and comparing the result with equation 2.17 and 2.18.

A linear retarder with a retardation between 0 and π is always able to transform a circular polarization to *any* elliptical polarization states and vice versa. This can be analyzed as follows. When circular polarization, $[\ 0 \quad 0 \quad \pm 1]^T$ on the Stokes space or unit quaternion $\pm\mathbf{k}$, is transformed by a linear retarder $\mathcal{L}(\gamma,\varphi)$, the rotation can be written as

$$\mathbf{S}' = \mathcal{L}(\gamma,\varphi)(\pm\mathbf{k})\mathcal{L}^*(\gamma,\varphi). \tag{2.21}$$

Substituting $\mathcal{L}(\gamma,\varphi)$ from equation 2.20 gives

$$\mathbf{S}' = \begin{bmatrix} \sin\varphi\sin 2\gamma \\ -\sin\varphi\cos 2\gamma \\ \cos\varphi \end{bmatrix}. \tag{2.22}$$

Comparing $\mathbf{S}'$ with the Stokes vector of elliptical polarization with an azimuth of ϑ and an ellipticity of ε (equation 2.6) yields

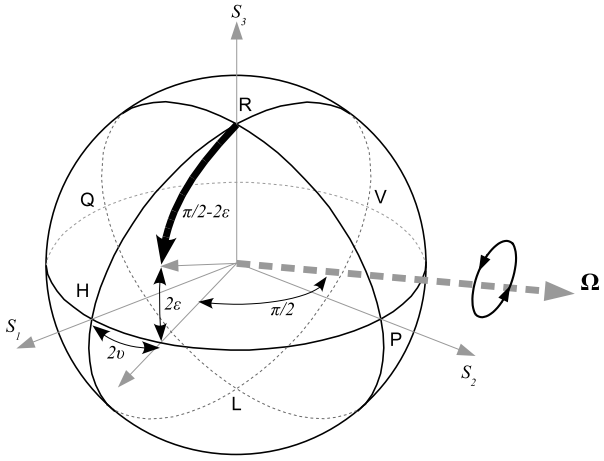

Figure 2.6: Transformation of circular polarization by a linear retarder

$$\varphi = \pi/2 - 2\varepsilon, \tag{2.23}$$
$$\gamma = \pm(\pi/2 + 2\vartheta). \tag{2.24}$$

On the Poincaré sphere, this transformation can be easily explained. As shown in figure 2.6, the axis $\mathbf{\Omega}$ (dashed arrow) should be placed a quadrature farther than the double azimuth (2ϑ) of the target elliptical polarization. The amount of retardation ($\pi/2 - 2\varepsilon$) corresponds to the necessary rotation (black thick arrow) to reach the target elliptical polarization from right circular polarization. If the input is left circular polarization, either the rotation axis must be moved additionally by π (or an odd multiple of π) or the direction of the rotation must be reversed.

Babinet compensator [27] and *Soleil-Babinet compensator* [28] are other types of variable retarders. They are called compensators due to earlier uses to *compensate* the phase delay between two field components in orthogonal polarizations. To do this, the compensators must be able to introduce a specific amount of positive *and* negative retardations. A Babinet compensator is a cascade of a linear retarder and a fractional waveplate. The fast axis of the linear retarder is orthogonal to the fast axis of the waveplate. When the retardation of the linear retarder equals that of the fractional waveplate, the total retardation is zero. By changing the linear retarder to have a less or more retardation, the total retardation can be varied in the positive and negative range [29]. A Soleil-Babinet compensator is another variant where two linear retarders (instead of only one) are placed in front of the fractional waveplate.

Phase Shifter

A *phase shifter* is a special case of a linear retarder where angle $\gamma = 0$. On the Poincaré sphere, polarization transformation by a phase shifter is equivalent to a rotation of φ around the axis S_1. It can be represented by the following unit quaternion

$$\mathcal{P}(\varphi) = \cos\frac{\varphi}{2} + \mathbf{i}\sin\frac{\varphi}{2}. \tag{2.25}$$

Mode Converter

A *mode converter* is a special case of a linear retarder where angle $\gamma = \pi/4$. On the Poincaré sphere, polarization transformation by a phase shifter is equivalent to a rotation of φ around the axis S_2. It can be represented by the following unit quaternion

$$\mathcal{M}(\varphi) = \cos\frac{\varphi}{2} + \mathbf{j}\sin\frac{\varphi}{2}. \tag{2.26}$$

Circular Retarder

A *circular retarder* is a variable retarder which transforms an input polarization by a rotation around the fixed axis S_3 and retardation φ. It can be represented by the following unit quaternion

$$\mathcal{C}(\varphi) = \cos\frac{\varphi}{2} + \mathbf{k}\sin\frac{\varphi}{2}. \tag{2.27}$$

A circular retarder can be realized by cascading two rotatable half-wave plates. If the rotations of waveplates are denoted by $\mathcal{H}(\gamma_1)$ and $\mathcal{H}(\gamma_2)$, then the total rotation is

$$\mathcal{H}(\gamma_2)\mathcal{H}(\gamma_1) \quad = \quad \cos(\pi - 2\gamma_1 - 2\gamma_2) + \mathbf{k}\sin(\pi - 2\gamma_1 - 2\gamma_2). \tag{2.28}$$

which is, according to equation 2.27, a circular retarder $\mathcal{C}(\varphi)$ with $\varphi = 4(\gamma_1 + \gamma_2)$.

2.2 Electro-Optic Linear Retarders

Polarization transformers can be realized by mechanical constructions which apply controlled changes to the properties of the fiber, for example by introducing squeezing [30] or bending [31]. However, electro-optic polarization retarder [32, 33] is currently is the most promising solution for a compact, reliable and responsive polarization transformer [34]. In the following section, a method to characterize electro-optic polarization retarders is presented. Using the characterization result, it is possible to find the polarization transformation of the device as a function of applied electrode voltages with a very high degree of accuracy.

2.2.1 Operating Principle

The electro-optic polarization transformer using $LiNbO_3$ (lithium niobate) crystals is shown in figure 2.7 [32]. It comprises of z-propagated waveguide on an x-cut substrate with three symmetrical electrodes (V_1, V_2, and V_3). If the middle electrode is grounded ($V_3 = 0$), the horizontal field component E_y in the region of the waveguide is induced by $V_1 - V_2$, while the vertical field component E_x is induced by $V_1 + V_2$.

The polarization transformation of the device depicted on the Poincaré sphere is shown in figure 2.8. Its phase retardation φ and eigenmode orientation ψ are determined by

$$\varphi \quad \sim \quad \sqrt{E_x^2 + E_y^2}, \tag{2.29a}$$

$$\tan(\psi - \pi/2) \quad \sim \quad \frac{E_x}{E_y}. \tag{2.29b}$$

The polarization transformer is thus a linear retarder. The eigenmode of the device lies in the S_1S_2 plane. From equation 2.29b, it can be seen that the eigenmode is endlessly

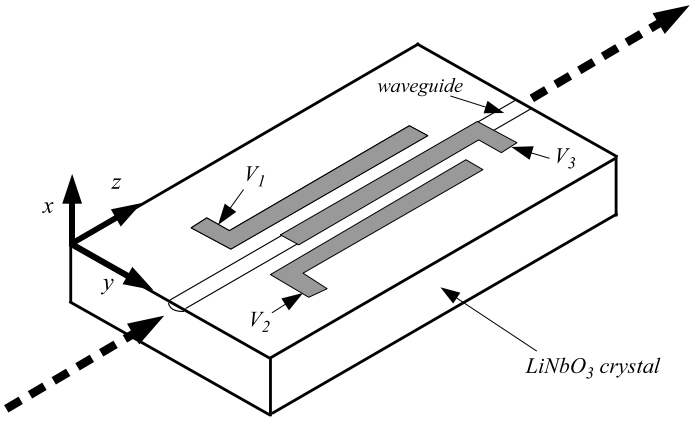

Figure 2.7: Structure of an x-cut z-propagation lithium niobate retarder

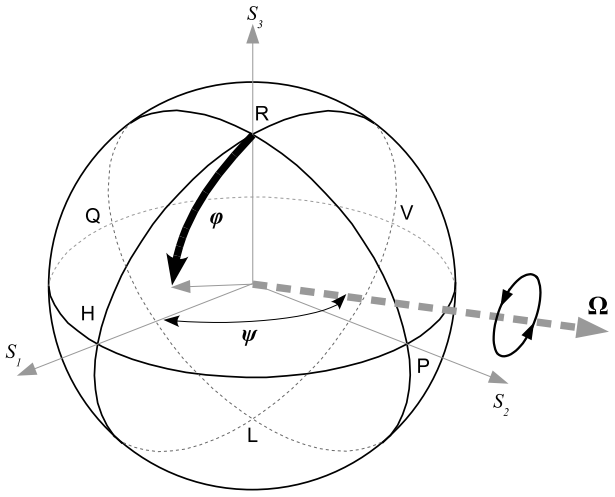

Figure 2.8: Polarization transformation of a lithium niobate retarder

Figure 2.9: Picture of EOSPACE multistage electro-optic polarization transformer

rotated even with a limited range of V_1, V_2. A circular polarization at the input of the device can be transformed into any elliptical polarization provided that V_1, V_2 can introduce a retardation in the range of $0...\pi$.

Several stages of electro-optic polarization transformer can be cascaded. Figure 2.9 shows a picture of a commercial electro-optic polarization transformer from EOSPACE which consists of 8 cascaded stages with a total insertion loss of $< 3\,dB$.

2.2.2 Quaternion Model

A model of electro-optic polarization transformer can be used to determine its operation as a function of electrode voltages, as well as to identify the electrode voltages needed to achieve a specific polarization conversion [35]. Polarization transformation of any retarders can be represented by a quaternion and thus, the model that is presented here is basically the quaternion model as a function of the applied voltages.

Based on equations 2.29a and 2.29b, suppose that:

$$\begin{aligned} E_x &= \kappa_x(V_1 + V_2 - V_{o,x}), \\ E_y &= \kappa_y(-V_1 + V_2 - V_{o,y}), \\ \varphi &= \frac{\pi}{V_\pi}\sqrt{E_x^2 + E_y^2}. \end{aligned}$$

,

then it follows

$$\cos\psi = \frac{\kappa_x(V_1 + V_2 - V_{o,x})}{\sqrt{\kappa_x^2(V_1 + V_2 - V_{o,x})^2 + \kappa_y^2(-V_1 + V_2 - V_{o,y})^2}}, \tag{2.30a}$$

$$\sin\psi = \frac{\kappa_y(-V_1 + V_2 - V_{o,y})}{\sqrt{\kappa_x^2(V_1 + V_{2-V_{o,x}})^2 + \kappa_y^2(-V_1 + V_2 - V_{o,y})^2}}, \tag{2.30b}$$

$$\varphi = \frac{\pi}{V_\pi}\sqrt{\kappa_x^2(V_1 + V_2 - V_{o,x})^2 + \kappa_y^2(-V_1 + V_2 - V_{o,y})^2}. \tag{2.30c}$$

The quaternion model of a linear retarder is thus

$$\begin{aligned}\mathcal{L}(V_1,V_2) \;=\; & \cos\frac{\pi}{2V_\pi}\sqrt{\kappa_x^2(V_1+V_2-V_{o,x})^2+\kappa_y^2(-V_1+V_2-V_{o,y})^2}+\\ & (\mathbf{i}\frac{\kappa_x(V_1+V_2-V_{o,x})}{\sqrt{\kappa_x^2(V_1+V_2-V_{o,x})^2+\kappa_y^2(-V_1+V_2-V_{o,y})^2}}+\\ & \mathbf{j}\frac{\kappa_y(-V_1+V_2-V_{o,y})}{\sqrt{\kappa_x^2(V_1+V_2-V_{o,x})^2+\kappa_y^2(-V_1+V_2-V_{o,y})^2}})\cdot\\ & \sin\frac{\pi}{2V_\pi}\sqrt{\kappa_x^2(V_1+V_2-V_{o,x})^2+\kappa_y^2(-V_1+V_2-V_{o,y})^2} \qquad (2.31)\end{aligned}$$

If the quaternion components (except the $\mathbf{k}$ component) in the above equations are denoted as L_0, L_1 and L_2, where $\mathcal{L}(V_1,V_2) = L_0(V_1,V_2) + \mathbf{i}L_1(V_1,V_2) + \mathbf{j}L_2(V_1,V_2)$, then each of these components defines a parametric surface as a function of V_1 and V_2. The contour plots for the quaternion components of an exemplary linear retarder with $\kappa_x = 1$, $\kappa_y = 0.8$, $V_\pi = 75$ V, $V_{o,x} = 10$ V, and $V_{o,y} = -20$ V are shown in figure 2.10.

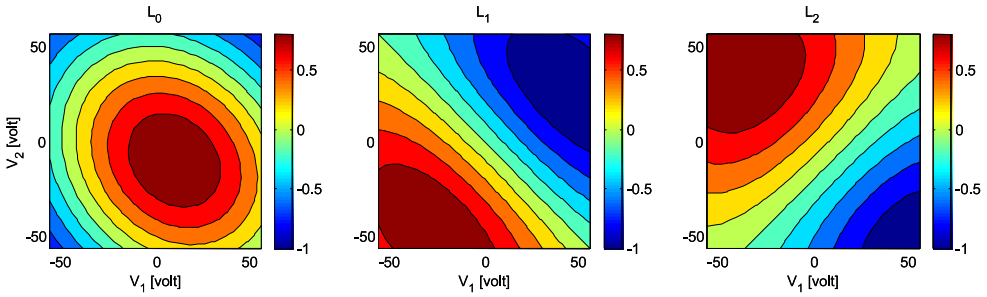

Figure 2.10: Contour of quaternion components of a linear retarder

Several observations can be made from these contour plots:

1. The constants κ_x and κ_y define the ellipticity of the contour lines in the contour plot for L_0. For the case where $\kappa_x = \kappa_y$, the contour lines will form circles instead of ellipses.

2. The offset voltages $V_{o,x} = 10$ V, and $V_{o,y} = -20$ V determine the center of the ellipses formed by the contour lines in the contour plot for L_0. This is because $L_0(V_1,V_2) = 1$ at the center of the ellipses which means zero retardation, which is achieved when $V_1 + V_2 = V_{o,x}$ and $-V_1 + V_2 = V_{o,y}$.

3. $\forall\, V_1 + V_2 = V_{o,x} : L_1(V_1,V_2) = 0$.

4. $\forall\, -V_1 + V_2 = V_{o,y} : L_2(V_1,V_2) = 0$.

2.2.3 Characterization

Compared to other polarization transformer models [35], the quaternion model has the advantage that it can be used to directly identify the eigenmode and the retardation for specific electrode voltages. In addition, rather than applying elimination procedures systematically (as in [35]) in order to get the model parameters, it is a simpler to characterize the retarder so that the quaternion can be obtained for the whole operation range of the electrode voltages [36].

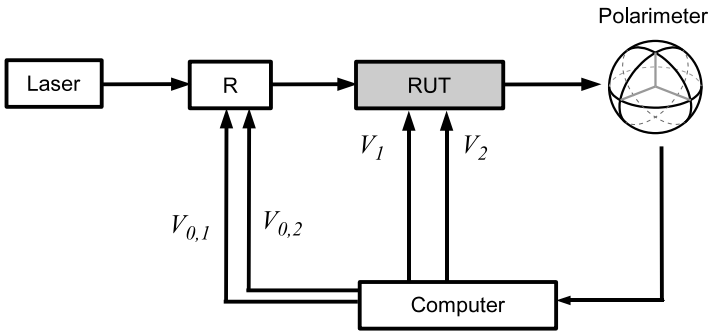

Figure 2.11: Experiment setup for retarder characterization

The experiment setup to perform characterization on an electro-optic retarder is shown in figure 2.11. The state of polarization $\mathbf{S}$ after the laser is fixed but unknown. Retarder R transforms this polarization for the Retarder Under Test (RUT). Additional polarization transformation after RUT, attributed among others to fiber connector, are unknown as well. However, this is generally fixed, at least during the characterization process. The Stokes parameters of polarization state $\mathbf{S}'$ which is measured by the polarimeter is

$$\mathbf{S}' = \mathcal{Q}_t \mathbf{S} \mathcal{Q}_t^*, \tag{2.32}$$

where $\mathcal{Q}_t$ denotes the unit quaternion representing total polarization transformation, defined as

$$\mathcal{Q}_t = \mathcal{Q}_f \mathcal{L}(V_1, V_2) \mathcal{Q}_R, \tag{2.33}$$

where $\mathcal{Q}_f$ is arbitrary transformation after RUT, $\mathcal{L}(V_1, V_2)$ is the transfer function of RUT, and $\mathcal{Q}_R$ is the rotation by retarder R.

First, the Stokes parameters $\overline{S_i}$ is obtained by measuring the output polarization of the RUT when setting the RUT electrodes to voltages $V_{b,1}, V_{b,2}$. If the polarization set at the input of the RUT (which is unknown) is denoted as S_i, its relation to $\overline{S_i}$ is described as

$$\overline{\mathbf{S_i}} = \mathcal{Q}_f \mathcal{Q}_b \mathbf{S_i} \mathcal{Q}_b^* \mathcal{Q}_f^*, \tag{2.34}$$

where $\mathcal{Q}_b = \mathcal{L}(V_{b,1}, V_{b,2})$ and $\mathcal{Q}_f$ accounts for arbitrary unknown rotation after the RUT, attributed among others to the fiber pigtail, cable and connectors. Although $\mathcal{Q}_f$ is not known, generally it is constant, at least during the measurement.

When voltages V_1, V_2 are applied to the RUT, the polarization $\mathbf{S_o}(V_1, V_2)$ observed by the polarimeter is:

$$\mathbf{S_o}(V_1, V_2) = \mathcal{Q}_f \mathcal{L}(V_1, V_2) \mathbf{S_i} \mathcal{L}(V_1, V_2)^* \mathcal{Q}_f^*. \tag{2.35}$$

From $\mathbf{S_o}(V_1, V_2)$ and the reference set $\overline{\mathbf{S_i}}$, it is possible to find $\hat{\mathcal{Q}}_k$ such as

$$\mathbf{S_o}(V_1, V_2) = \hat{\mathcal{Q}}_k(V_1, V_2) \overline{\mathbf{S_i}} \hat{\mathcal{Q}}_k^*(V_1, V_2). \tag{2.36}$$

This is known as the absolute orientation problem for which non-iterative solutions are available (Appendix B). More precisely, here only rotation needs to be considered as the transformation because there is no translation. At least three data points for $\overline{\mathbf{S_i}}$ and for $\mathbf{S_o}(V_1, V_2)$ are necessary to infer $\hat{\mathcal{Q}}_k(V_1, V_2)$. For convenience, retarder R is chosen

to be another electro-optic retarder so that different $\overline{\mathbf{S_i}}$ and $\mathbf{S_o}(V_1, V_2)$ are obtained by changing the electrode voltages $V_{0,1}, V_{0,2}$ applied to R.

Eliminating $\overline{S_i}$ gives an alternative expression for $\mathbf{S_o}(V_1, V_2)$

$$\mathbf{S_o}(V_1, V_2) = \hat{\mathcal{Q}}_k(V_1, V_2)\mathcal{Q}_f Q_b \mathbf{S_i} \mathcal{Q}_b^* \mathcal{Q}_f^* \hat{\mathcal{Q}}_k^*(V_1, V_2). \tag{2.37}$$

Comparing the above equation with equation 2.35 gives

$$\mathcal{Q}_f \mathcal{L}(V_1, V_2)\mathbf{S_i}\mathcal{L}(V_1, V_2)^* \mathcal{Q}_f^* = \hat{\mathcal{Q}}_k(V_1, V_2)\mathcal{Q}_f Q_b \mathbf{S_i} \mathcal{Q}_b^* \mathcal{Q}_f^* \hat{\mathcal{Q}}_k^*(V_1, V_2), \tag{2.38}$$

which is simplified to

$$\mathcal{Q}_f \mathcal{L}(V_1, V_2) = \hat{\mathcal{Q}}_k(V_1, V_2)\mathcal{Q}_f Q_b. \tag{2.39}$$

Solving for $\mathcal{L}(V_1, V_2)$ yields

$$\mathcal{L}(V_1, V_2) = \mathcal{Q}_f^{-1} \hat{\mathcal{Q}}_k(V_1, V_2)\mathcal{Q}_f \mathcal{Q}_b. \tag{2.40}$$

If the voltages $V_{b,1}, V_{b,2}$ are chosen so that $\mathcal{Q}_b = \mathcal{L}(V_{b,1}, V_{b,2}) = 1$, then the above equation is simplified to

$$\mathcal{L}(V_1, V_2) = \mathcal{Q}_f^{-1} \hat{\mathcal{Q}}_k(V_1, V_2)\mathcal{Q}_f. \tag{2.41}$$

which means that $\mathcal{L}(V_1, V_2)$ is just $\hat{\mathcal{Q}}_k(V_1, V_2)$ with its coordinate system rotated by $\mathcal{Q}_f^{-1}$. Arbitrary constant rotation of the coordinate system like this typically can be ignored. However, it is useful to choose an estimate of $\mathcal{Q}_f$ so that $\mathcal{L}(V_1, V_2)$ is as close as possible to the birefringence model of a linear retarder (equation 2.31), since the characterized device is a linear retarder anyway. If the estimates of $\mathcal{Q}_f$ and $\mathcal{L}(V_1, V_2)$ are denoted as $\hat{\mathcal{Q}}_f$ and $\hat{\mathcal{L}}(V_1, V_2)$ respectively, then it follows

$$\hat{\mathcal{L}}(V_1, V_2) = \hat{\mathcal{Q}}_f^{-1} \hat{\mathcal{Q}}_k(V_1, V_2)\hat{\mathcal{Q}}_f. \tag{2.42}$$

Because $\hat{\mathcal{Q}}_f$,$\hat{\mathcal{Q}}_k$, and $\hat{\mathcal{L}}(V_1, V_2)$ are all quaternions, they can be written as

$$\begin{aligned}
\hat{\mathcal{Q}}_f &= \hat{Q}_{f,0} + \mathbf{i}\hat{Q}_{f,1} + \mathbf{j}\hat{Q}_{f,2} + \mathbf{k}\hat{Q}_{f,3}, \\
\hat{\mathcal{Q}}_k(V_1, V_2) &= \hat{Q}_{k,0}(V_1, V_2) + \mathbf{i}\hat{Q}_{k,1}(V_1, V_2) + \mathbf{j}\hat{Q}_{k,2}(V_1, V_2) + \mathbf{k}\hat{Q}_{k,3}(V_1, V_2), \\
\hat{\mathcal{L}}(V_1, V_2) &= \hat{L}_0(V_1, V_2) + \mathbf{i}\hat{L}_1(V_1, V_2) + \mathbf{j}\hat{L}_2(V_1, V_2) + \mathbf{k}\hat{L}_3(V_1, V_2),
\end{aligned} \tag{2.43}$$

then using equation 2.42, the $\mathbf{i}$, $\mathbf{j}$, and $\mathbf{k}$ components of $\hat{\mathcal{L}}(V_1, V_2)$ are

$$\begin{aligned}
\hat{L}_1(V_1, V_2) &= \hat{Q}_{k,1}(V_1, V_2)(\hat{Q}_{f,0}^2 + \hat{Q}_{f,1}^2 - \hat{Q}_{f,2}^2 - \hat{Q}_{f,3}^2) + \\
&\quad \hat{Q}_{k,2}(V_1, V_2)(2\hat{Q}_{f,0}\hat{Q}_{f,3} + 2\hat{Q}_{f,1}\hat{Q}_{f,2}) + \\
&\quad \hat{Q}_{k,3}(V_1, V_2)(2\hat{Q}_{f,1}\hat{Q}_{f,3} - 2\hat{Q}_{f,0}\hat{Q}_{f,2}),
\end{aligned} \tag{2.44a}$$

$$\begin{aligned}
\hat{L}_2(V_1, V_2) &= \hat{Q}_{k,1}(V_1, V_2)(2\hat{Q}_{f,1}\hat{Q}_{f,2} - 2\hat{Q}_{f,0}\hat{Q}_{f,3}) + \\
&\quad \hat{Q}_{k,2}(V_1, V_2)(\hat{Q}_{f,0}^2 - \hat{Q}_{f,1}^2 + \hat{Q}_{f,2}^2 - \hat{Q}_{f,3}^2) + \\
&\quad \hat{Q}_{k,3}(V_1, V_2)(2\hat{Q}_{f,0}\hat{Q}_{f,1} + 2\hat{Q}_{f,2}\hat{Q}_{f,3}),
\end{aligned} \tag{2.44b}$$

$$\begin{aligned}
\hat{L}_3(V_1, V_2) &= \hat{Q}_{k,1}(V_1, V_2)(2\hat{Q}_{f,1}\hat{Q}_{f,3} + 2\hat{Q}_{f,2}\hat{Q}_{f,0}) + \\
&\quad \hat{Q}_{k,2}(V_1, V_2)(2\hat{Q}_{f,2}\hat{Q}_{f,3} - 2\hat{Q}_{f,1}\hat{Q}_{f,0}) + \\
&\quad \hat{Q}_{k,3}(V_1, V_2)(\hat{Q}_{f,0}^2 - \hat{Q}_{f,1}^2 - \hat{Q}_{f,2}^2 + \hat{Q}_{f,3}^2),
\end{aligned} \tag{2.44c}$$

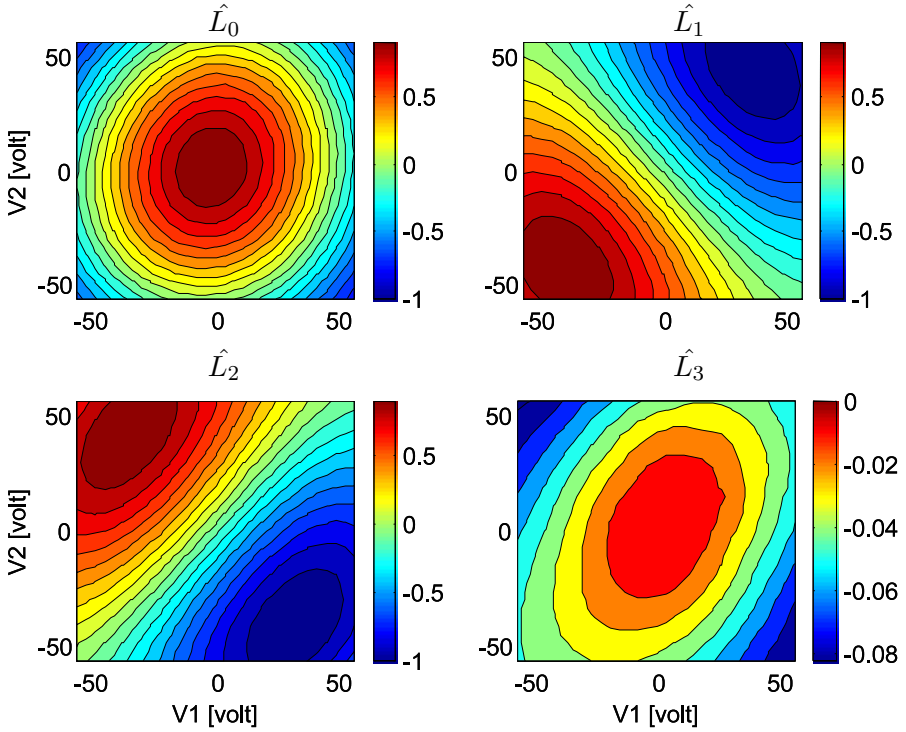

Figure 2.12: Characterization result of a lithium-niobate retarder

To have $\hat{\mathcal{L}}(V_1, V_2)$ as a linear retarder, $\hat{\mathcal{Q}}_f$ must be chosen so that the characteristics of the components $\hat{\mathcal{L}}(V_1, V_2)$ match those of a linear retarder, based on observations of figure 2.10 described previously.

By defining a cost function $J(\hat{\mathcal{Q}}_f)$ as

$$\begin{aligned} J(\hat{\mathcal{Q}}_f) \quad = \quad & \sum_i \hat{L}_1^2(V_{b,1} + i, V_{b,2} - i) + \\ & \sum_i \hat{L}_2^2(V_{b,1} + i, V_{b,2} + i) + \\ & \sum_i \sum_j \hat{L}_3^2(V_i, V_j), \end{aligned} \tag{2.45}$$

then $\hat{\mathcal{Q}}_f$ can be obtained using iterative multidimensional optimization with $J(\hat{\mathcal{Q}}_f)$ as the minimization criteria. For this particular optimization problem, particle swarm optimization algorithm [37] was found to give accurate solutions with a satisfactory convergence speed.

Figure 2.12 shows the characterization result of a lithium-niobate electro-optic retarder. The electrode voltages are swept over the range $(-56\,V,\, 56\,V)$ with a voltage quantization of $3.75\,V$. It was found that $V_{b,1} = 1.73\,V$ and $V_{b,2} = -1.39\,V$. The characterization result matches with the birefringence model shown previously in figure 2.10. As can be seen from the contour plot of $\hat{L}_3$, the $\mathbf{k}$ component of $\hat{\mathcal{L}}(V_1, V_2)$ is not completely zero. However it is very close to zero especially in the vicinity of the centers of the ellipses formed by the contour lines of $\hat{L}_1$ where the retardation is small.

2.2.4 State-Space Model

The response of an x-cut, z-propagated waveguide lithium-niobate linear retarder is increased by a finite buffer layer isolation [34]. The retarder therefore does not give fully instantaneous response. If such a retarder is employed in an automatic polarization control system, this non-rectangular step response may limit the tracking speed [38]. It is thus interesting to analyze the transient-stage retarder response in order to find the limitation of its operation in a polarization controller.

From the quaternion model of an electro-optic linear retarder, the retardation φ can be described (using the time-invariant state-space form [39]) by the following linear system

$$\frac{d\mathbf{x}(t)}{dt} = \mathbf{A}\mathbf{x}(t) + \mathbf{B}\begin{bmatrix} V_1(t) & V_2(t) \end{bmatrix}, \tag{2.46a}$$

$$\varphi(t) = \mathbf{C}\mathbf{x}(t), \tag{2.46b}$$

where $x(t)$ is the state vector, $\mathbf{A}$ is the state matrix, $\mathbf{B}$ is the input matrix and $\mathbf{C}$ is the output matrix.

The linear retarder can be operated with $V_1 = V_2$ (only the field component E_x is applied) or $V_1 = -V_2$ (only the field component E_y is applied), where it acts like a mode converter and a phase shifter, respectively [40]. Without a loss of generality, here only the case $V_3 = 0$ is considered. The state-space model is thus simplified and discretized to

$$\mathbf{x_1}(k+1) = \mathbf{A_1}\mathbf{x_1}(k) + \mathbf{B_1}V_1(k), \tag{2.47a}$$

$$\varphi_1(k) = \mathbf{C_1}\mathbf{x_1}(k). \tag{2.47b}$$

The model parameters $\mathbf{A_1}$, $\mathbf{B_1}$, and $\mathbf{C_1}$ can be estimated by system identification methods [41]. It is common to measure the input and output sequences of the system experimentally and then optimize the model parameters to fit the model's dynamic to the observations.

For this analysis, a pseudo-random binary sequence (PRBS) with the shortest pulse width of 1 ms as the input excitation $V_1(t)$ was used to trigger the retarder and then $\varphi_1(t)$ was recorded with a sampling rate of 10 MHz. The result is shown in figure 2.13 where the dotted line and the solid line denote the retarder input voltage and normalized output retardation, respectively. In this figure, the response is shown only for about 30 ms, although it was actually measured and further analyzed for a duration of up to 250 ms.

From the measurement data, the *N4SID* subspace identification algorithm [42, 43] was used to estimate the model parameters. The discrete state-space model was specified for a sampling period of 10 μs and an order of 4. The optimal parameters were found as

$$\mathbf{A_1} = \begin{bmatrix} 0.1349 & -0.5721 & 0.5607 & 0.2577 \\ -0.1765 & 0.8701 & 0.6144 & 0.1723 \\ 0.0112 & 0.0091 & 0.8156 & -0.3929 \\ 0.0002 & 0 & -0.0296 & -0.3524 \end{bmatrix}, \tag{2.48a}$$

$$\mathbf{B_1} = \begin{bmatrix} -0.8563 \\ -0.1739 \\ 0.0115 \\ 0.0019 \end{bmatrix}, \tag{2.48b}$$

$$\mathbf{C_1} = \begin{bmatrix} -0.9773 & -0.2111 & 0.0177 & 0.0001 \end{bmatrix}. \tag{2.48c}$$

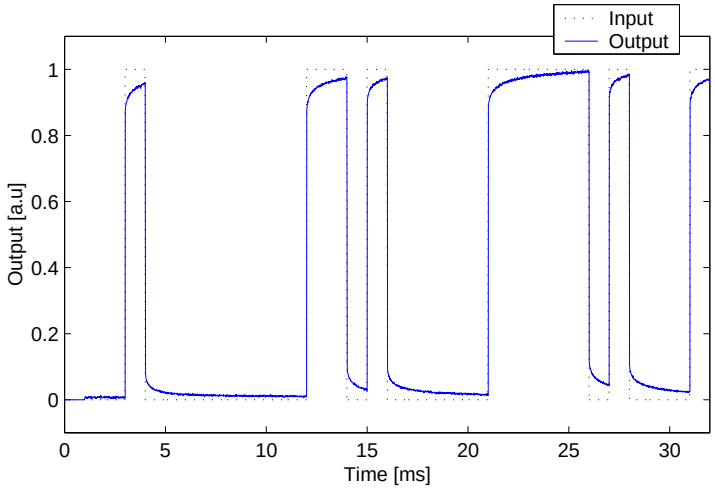

Figure 2.13: Measured output of a linear retarder with pseudo-random input pulses

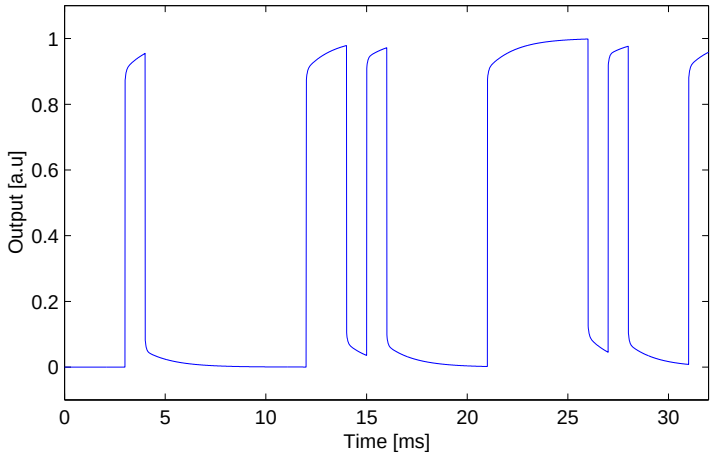

Figure 2.14: Output of the estimated state-space model

Figure 2.14 shows the response of the estimated model, which is similar to the actual retarder response shown in figure 2.13. Although the model is only of the fourth order, the estimation error already reaches a mean and a standard deviation of $7.16 \cdot 10^{-3}$ and $4.36 \cdot 10^{-3}$, respectively. A more accurate estimation, if necessary, can be obtained by increasing the order of the state-space model.

It has been suggested that the response of the electro-optic can be improved by electrical equalization [38]. The state-space model that is presented here could be used to synthesize an equalizer if this were necessary.

2.3 Calibrated Retarders

Using the quaternion model of a linear retarder (equation 2.20), the necessary voltages which correspond to a specific retardation and eigenmode can be calculated. Graphically, this is also clear from the contour plots of the quaternion components of the linear retarder (figure 2.10 and 2.12). For example, since a contour line in the contour plot for L_0 is the locus for constant retardation, voltages that trace along this contour line rotate

the eigenmode and thus operate the linear retarder like a rotating fractional waveplate.

2.3.1 Linear Retarder Operation

For an ideal linear retarder, the voltages which correspond to a certain rotation are functions of the model parameters (κ_x, κ_y, V_π, $V_{o,x}$, and $V_{o,y}$). For an electro-optic linear retarder that has been characterized, these voltages can be inferred from the characterization result. This can be formulated as follows. The unit quaternion of the characterized linear retarder for electrode voltages V_1, V_2 must represent a retardation of φ and the eigenmode of $[\ \cos\psi \quad \sin\psi \quad 0\ ]^T$, written as

$$\hat{\mathcal{L}}(V_1, V_2) = \cos\frac{\varphi}{2} + \mathbf{i}\sin\frac{\varphi}{2}\cos\psi + \mathbf{j}\sin\frac{\varphi}{2}\sin\psi. \tag{2.49}$$

$\hat{\mathcal{L}}(V_1, V_2)$ is obtained from the optimization process in the characterization procedure (equation 2.42). However, $\hat{\mathcal{L}}(V_1, V_2)$ is not a continuous two-dimensional function of the electrode voltages V_1, V_2 since V_1, V_2 are swept with a quantization of $3.75\,V$. If there exist integer values i_1, i_2, j_1, j_2 such as $i_1\Delta V < V_1 < i_2\Delta V$ and $j_1\Delta V < V_2 < j_2\Delta V$ where ΔV denotes the voltage quantization, then $\hat{\mathcal{L}}(V_1, V_2)$ can be approximated by two-dimensional spherical linear interpolation (equation A.17) using the following set of equations:

$$\begin{aligned}
\hat{\mathcal{L}}(V_1, j_1\Delta V) &= \frac{\sin(i_2 - V_1/\Delta V)\delta_1}{\sin\delta_1}\hat{\mathcal{L}}(i_1\Delta V, j_1\Delta V) + \\
&\quad \frac{\sin(V_1/\Delta V - i_1)\delta_1}{\sin\delta_1}\hat{\mathcal{L}}(i_2\Delta V, j_1\Delta V), && (2.50a)\\
\hat{\mathcal{L}}(V_1, j_2\Delta V) &= \frac{\sin(i_2 - V_1/\Delta V)\delta_2}{\sin\delta_2}\hat{\mathcal{L}}(i_1\Delta V, j_2\Delta V) + \\
&\quad \frac{\sin(V_1/\Delta V - i_1)\delta_2}{\sin\delta_2}\hat{\mathcal{L}}(i_2\Delta V, j_2\Delta V), && (2.50b)\\
\hat{\mathcal{L}}(V_1, V_2) &= \frac{\sin(j_2 - V_2/\Delta V)\delta}{\sin\delta}\hat{\mathcal{L}}(V_1, j_1\Delta V) + \\
&\quad \frac{\sin(V_2/\Delta V - j_1)\delta}{\sin\delta}\hat{\mathcal{L}}(V_1, j_2\Delta V), && (2.50c)
\end{aligned}$$

with

$$\begin{aligned}
\cos\delta_1 &= \hat{\mathcal{L}}(i_1\Delta V, j_1\Delta V)\cdot\hat{\mathcal{L}}(i_2\Delta V, j_1\Delta V), && (2.51a)\\
\cos\delta_2 &= \hat{\mathcal{L}}(i_1\Delta V, j_2\Delta V)\cdot\hat{\mathcal{L}}(i_2\Delta V, j_2\Delta V), && (2.51b)\\
\cos\delta &= \hat{\mathcal{L}}(V_1, j_1\Delta V)\cdot\hat{\mathcal{L}}(V_1, j_2\Delta V). && (2.51c)
\end{aligned}$$

By defining a cost function

$$\begin{aligned}
J(V_1, V_2) &= [\hat{\mathcal{L}}(V_1, V_2) - \\
&\quad (\cos\frac{\varphi}{2} + \mathbf{i}\sin\frac{\varphi}{2}\cos\psi + \mathbf{j}\sin\frac{\varphi}{2}\sin\psi)]^2, && (2.52)
\end{aligned}$$

V_1, V_2 can be obtained using two-dimensional optimization steps with $J(V_1, V_2)$ as the minimization criteria. With V_1, V_2 for a given rotation (retardation φ and eigenmode orientation ψ) obtained from the characterization result, it is then possible to operate

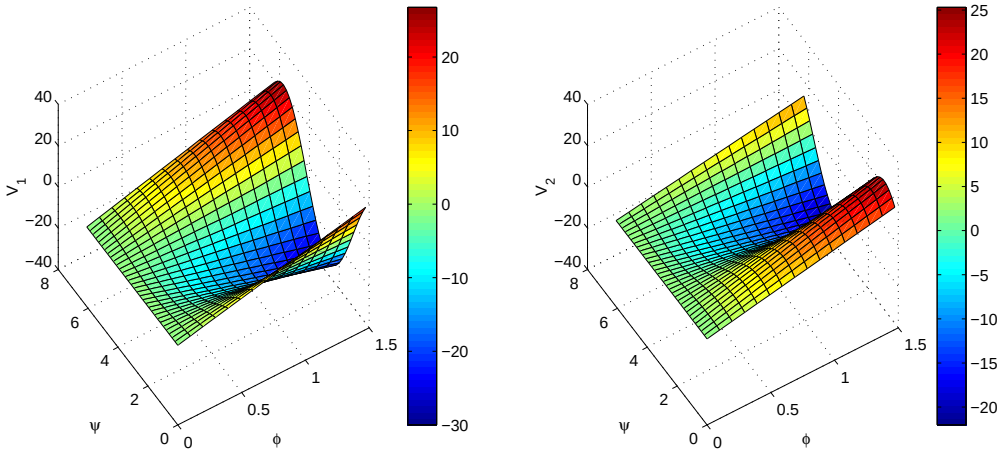

Figure 2.15: Calibrated retarder voltages for different retardation and eigenmode orientation

the electro-optic retarder to realize a specific polarization transformation. This is also sufficiently true even if the retarder inhibits a somewhat non-ideal behavior. Thus, using these steps it can be said that the retarder is *calibrated*.

Figure 2.15 shows the surface plots of the voltages V_1, V_2 as functions of retardation $\varphi\,(0 \ldots \pi/2)$ and eigenmode orientation $\psi\,(0 \ldots 2\pi)$ obtained using the above optimization procedure for the electro-optic linear retarder for which the characterization result is already shown in figure 2.12.

2.3.2 Fractional Waveplate Operation

To operate a linear retarder as a quarter-wave plate, the retardation φ is simply set to $\pi/2$. This means, the cost function $J(V_1, V_2)$ for the optimization procedure to find V_1, V_2 is simplified to

$$J(V_1, V_2) \quad = \quad [\hat{\mathcal{L}}(V_1, V_2) - \frac{1}{2}\sqrt{2}(1 - \mathbf{i}\cos\psi - \mathbf{j}\sin\psi)]^2. \tag{2.53}$$

Figure 2.16 shows voltages V_1, V_2 for 32 different quarter-wave plate axis orientations $\psi\,(0 \ldots \pi)$ again for the electro-optic linear retarder for which the characterization result is already shown in figure 2.12. If the quaternions $\hat{\mathcal{L}}(V_1, V_2)$ for the different axis orientation are used to transform a circular polarization, the result will be linear polarizations, as shown on the Poincaré sphere in figure 2.17. The resulting polarization states mismatch between the transformed trajectory and linear polarization states has a root mean square error of only 0.0176. It proves that V_1, V_2 in figure 2.16 really operate the calibrated linear retarder as a quarter-wave plate with a high degree of accuracy.

For half-wave plate operation, the voltages will be suitably doubled because now the retardation φ equals π.

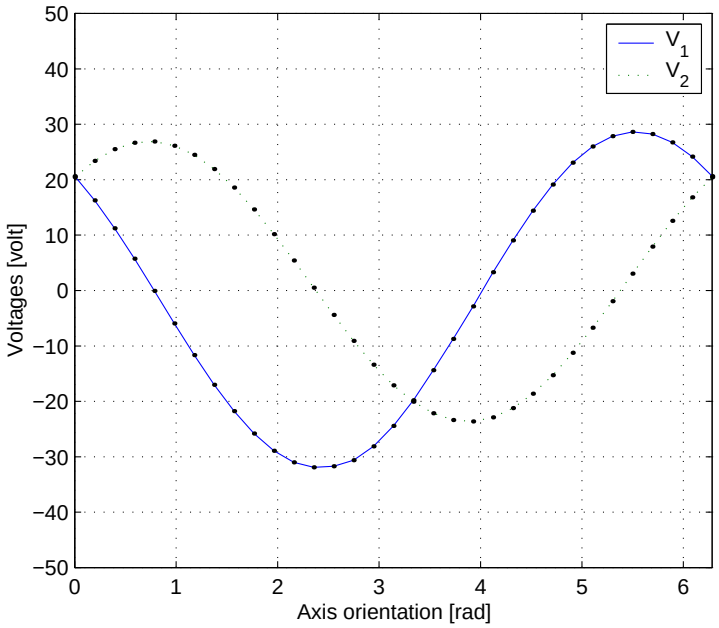

Figure 2.16: Retarder voltages for quarter-wave plate operation

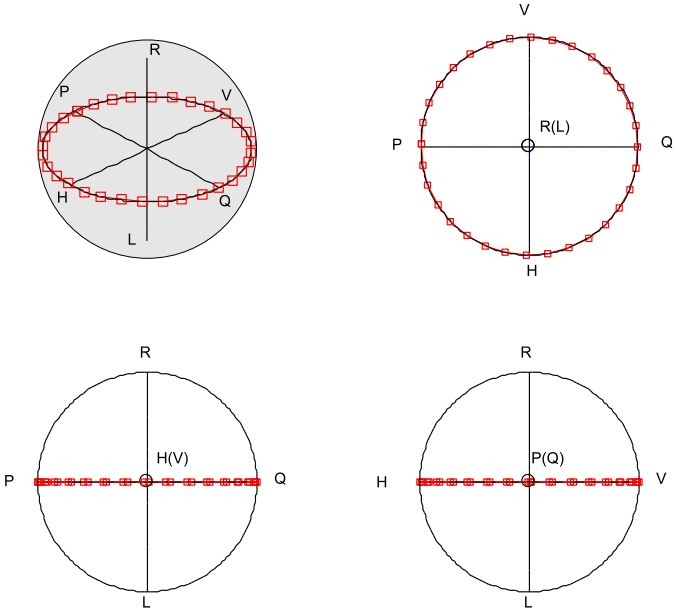

Figure 2.17: Circular polarization transformation by a calibrated quarter-wave plate

Chapter 3

FPGA-Based Polarization Control System

3.1 Polarization Control Algorithms

An automatic polarization controller has the task of transforming an input state of polarization into an output state of polarization subject to certain conditions. In a system where the optical signal needs to be coupled into a polarization sensitive device, the polarization controller must perform the polarization transformation so that the output polarization always matches the required polarization state for the device. If the input polarization is time-variant, this implies a polarization tracking since the necessary polarization transformation is also time-variant. This holds also for a varying output polarization state. Thus, a common structure to implement an automatic polarization controller is a feedback control system.

An early application of automatic polarization control is for optical coherent receivers. In such a receiver, the received signal and the local oscillator signal are combined in an interferometer and then detected with a photo detector. The photo intensity is

$$I \quad \propto \quad \cos^2(\varphi/2), \tag{3.1}$$

where φ denotes the angle (on the Poincaré sphere) between the polarization state of the received signal and the polarization state of the local oscillator. The intensity vanishes when the polarization states are orthogonal ($\varphi = \pi$). Maximum intensity is obtained only when $\varphi = 0$ which occurs only when both polarization states match perfectly. Intensity optimization can be achieved by using a polarization controller for the local oscillator signal so that its polarization state match that of the received signal. However, the polarization state of the received signal continuously changes due to the temperature, vibration and other mechanical disturbances on the transmission fiber and therefore necessitates the use of automatic polarization control.

The first attempts at polarization stabilization used a polarimeter to give a feedback signal to the polarization transformer [44, 45]. The polarimeter measured the current polarization state and delivered two error signals corresponding to the amount of retardation corrections required to bring the input polarization to the target output polarization. Two independent proportional-integral controllers were driven by the error signals in order to adjust the retardation of the two waveplates. Because a polarimeter is needed, it can not be used in a system where the output polarization can not be measured or is not available, for example in a coherent receiver. However, this can be easily remedied since the intensity detected by the receiver (equation 3.1) serves as the feedback signal [46, 47]. When this feedback signal is maximized, it indicates matched polarization states.

Other common polarization stabilization configurations are illustrated in figure 3.1. A varying input polarization is to be stabilized into a fixed output polarization, for example if the signal is to be processed further by a polarization sensitive device. A polarizer

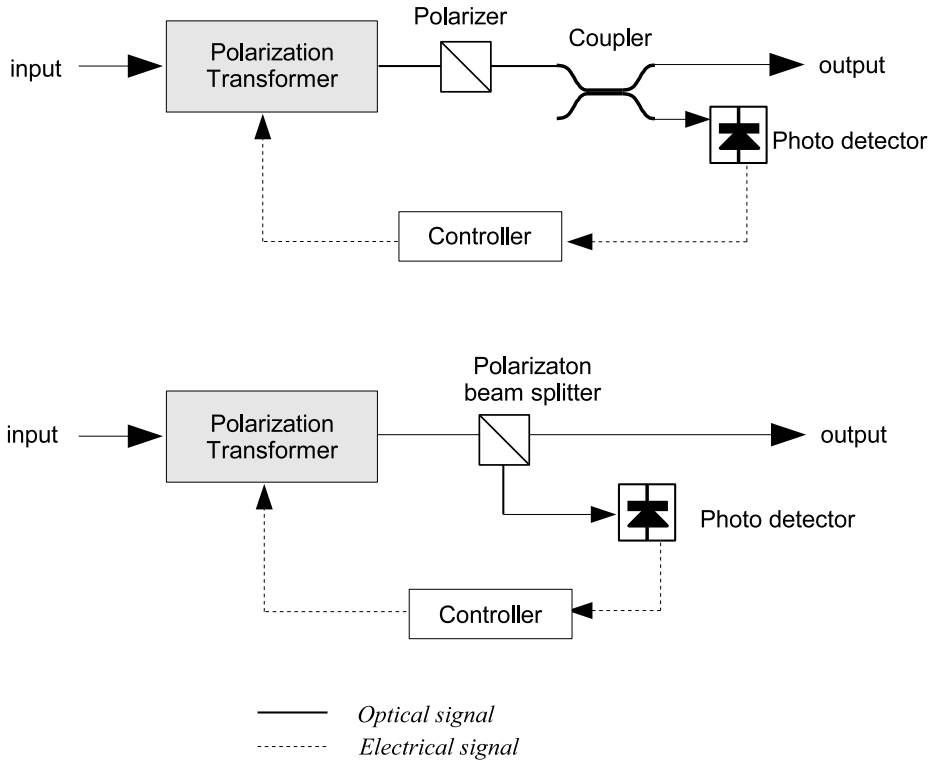

Figure 3.1: Polarization stabilization configurations

which passes only one polarization state (which matches its transmission axis) can be used to get a fixed polarization optical signal. The intensity at its output depends on the polarization matching similar to the relation in equation 3.1 but now with φ denoting the angle between the input polarization state and the polarizer axis. If the intensity is maximized by the controller, the output of the polarizer will have a fixed polarization and a maximum optical intensity. Another variant is by using a polarization beam splitter that outputs two orthogonal polarizations. In this configuration, the intensity at one of its output should be minimized so that the other output will have a maximum optical intensity.

In a polarization division multiplex transmission, two modulated data streams in two orthogonal polarizations are launched into the transmission fiber. At the receiver, the two polarizations stay generally orthogonal. However, their absolute polarization states are unknown due to random polarization changes in the fiber. A receiver must therefore demultiplex the signal into two polarization channels before the data stream in each of the channel can be correctly demodulated. Usually a setup similar to figure 3.1 (bottom) is implemented, but with both outputs of the polarization beam splitter connected to the subsequent demodulation circuit. In addition, since *both* polarization channels contain data, the feedback signal can not continue to be obtained anymore from a simple photo detector at only *one* optical output of the beam splitter. One solution is to electrically mix the demodulated electrical signal and recovered clock and use the result as the feedback signal since it is proportional to the optical intensity of the selected polarization channel [48]. Another alternatives is to use correlation signal or interference signal between the two polarization channels, each being inversely related to the degree of polarization matching in the beam splitter [49, 50].

3.1.1 Design Considerations

Polarization Transformers

An important factor that determines the performance of an automatic polarization controller is the speed of the polarization transformer that is used as the control element. In its early development, fiber squeezers with electromechanical driving were common choices [44, 47, 51, 52]. A fiber squeezer can be treated as a retardation waveplate with a *fixed* eigenmode and a *variable* retardation. Therefore a cascade of few fiber squeezers (with unequal eigenmodes) is necessary to realize an arbitrary polarization transformation. The same principle can be applied to electro-optic polarization transformers with fixed axes [45, 53, 54] which can operate at a higher speed compared to the fiber squeezers. Rotating fractional waveplates implemented as electro-optic devices [55], liquid crystals [56, 57, 58] or magnetic Faraday rotators [59, 60] can also be used as the polarization transformers. Nowadays, commercial automatic polarization controllers typically use electro-optic polarization transformers [61, 62] because currently electro-optic devices offer the fastest response time.

Figure 3.2 shows the photointensity in equation 3.1 as a function of polarization transfomer driving signals, if the polarization transfomer has a circular polarization at its input and the target polarization is horizontal (left) or +45°(right). Since this intensity is related to the polarization matching, the controller generally dithers or modulates the driving signals and detects the changes in the feedback signal to infer the degree of polarization state matching [63], similar to the principle of a lock-in amplifier. The amount of dithering must be chosen to be small enough so that it does not introduce considerable signal fluctuation but at the same time large enough so that the corresponding changes in the feedback signal is still not submerged in noises. Figure 3.3 illustrates the different changes in the feedback signal $I(\alpha)$ as a function of the operating point α when the low-amplitude parasitic modulation is applied to α at different points. The controller essentially obtains $\partial I(\alpha)/\partial\alpha$ (positive at point P, negative at point R) and uses it to apply the necessary correction to bring α to the optimal value (point Q). Since only (instantaneous) $\partial I(\alpha)/\partial\alpha$ is important, not the absolute value of $I(\alpha)$, the controller tolerates slow fluctuations of the intensity.

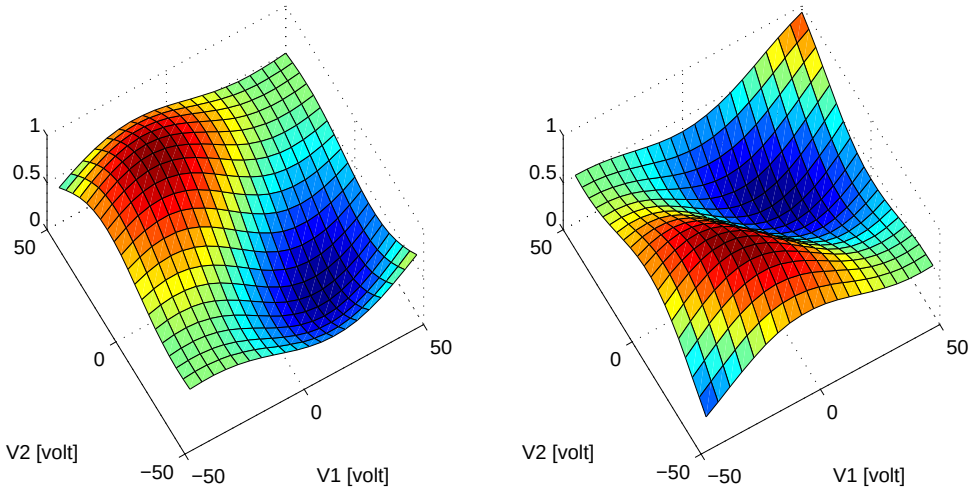

Figure 3.2: Photointensity as a function of the driving signals for horizontal (left) and +45°(right) target polarization

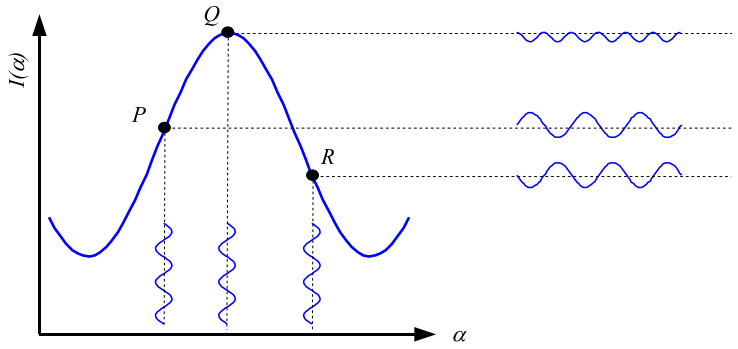

Figure 3.3: Dithering effect at different operating points

For polarization transformers with finite retardation range (such as fiber squeezers and linear electro-optic retarders), at some point the controller must be able to perform *unwinding* whenever one of the polarization transformer reaches the retardation limit. [51, 64]. This is carried out in order to bring the operating point back within its range. On the other hand, polarization transformers like rotating fractional waveplates do not need unwinding [55]. Therefore, the algorithm for automatic polarization control is unsurprisingly related to the type of the polarization transformer used in the system.

Endless Control

In addition, for practical applications, an automatic polarization must be able to continuously maintain polarization matching in the case of rapidly varying changes in the input and/or output polarization states, even if the polarization states wander many or possibly an infinite number of times around the Poincaré sphere. This is often referred to as *endless control*. When the controller can not track the polarization changes, momentary polarization mismatch will occur and this is unacceptable since such an interruption may cause loss of data. If the controller employs polarization transformers with a finite retardation range and one of the polarization transformers needs unwinding, the controller must carry out the unwinding procedure without affecting the overall polarization transformation and thus also polarization matching [47, 52]. Because polarization transformer unwinding essentially has the objective of moving back its operating point to the retardation range, it is also called *reset*. Strictly speaking, reset generally refers to a large change in the controller driving signals (for example, electrode voltages for lithium niobate waveplate) to track an infinitesimal polarization change [65, 66].

The mathematical definition of an endless operation (similar to [66]) is described as follows. Without loss of generality, it is assumed that the polarization transformers comprise N cascaded retarders $\mathcal{Q}_i(\alpha_i),\ i = 1 \dots N$ with α_i defines the physical parameters of the retarder. The total polarization transformation is

$$\mathcal{Q}_R(\alpha_N, \alpha_{N-1}, \dots, \alpha_2, \alpha_1) = \mathcal{Q}_N(\alpha_N)\mathcal{Q}_{N-1}(\alpha_{N-1}) \cdots \mathcal{Q}_2(\alpha_2)\mathcal{Q}_1(\alpha_1). \tag{3.2}$$

The controller is to transform a sequence of input polarization states $S_{i,1}, S_{i,2}, \cdots$ to a sequence of output polarization states $S_{o,1}, S_{o,2}, \cdots$. The conditions for an endless and deterministically reset-free operation of the controller are:

1. There exist $\alpha_{i,n},\ i = 1 \dots N$ such that

$$S_{o,n} = \mathcal{Q}_R^*(\alpha_{i,n}) S_{i,n} \mathcal{Q}_R(\alpha_{i,n}) \qquad n = 0, 1, \dots \tag{3.3}$$

2. Parameters $\alpha_{i,n}$ *always* lie within the operating limitations of the retarders

3. There is an absolute constant $0 < C_Q < \infty$ such that

$$\max_{i=1\ldots N} |\alpha_{i,n} - \alpha_{i,n-1}| \leq C_Q(\|S_{i,n} - S_{i,n-1}\| + \|S_{o,n} - S_{o,n-1}\|) \qquad n > 0. \quad (3.4)$$

The last condition guarantees that the changes in the physical parameters of the polarization transformers when the controller responds to a certain change in the input and/or output polarization will be well defined within a certain limit. The controller is called *reset-free* only when this condition is fulfilled.

Tracking Speed Limit

To judge the performance of an automatic polarization control system, it is necessary to know its worst-case tracking speed. Because the polarization transformer has limited response time, the theoretical tracking speed limit can be analyzed by finding one or more sequences in the input and/or output polarization states that put the highest load on the controller. Put another way, the worst-case sequence causes the controller to operate on its limit which mathematically means that $\max_{i=1\ldots N} |\alpha_{i,n} - \alpha_{i,n-1}|$ reaches its maximum value.

Assume the polarization transformer is a cascade of two fiber squeezers [1]. The axes of the fiber squeezers are inclined by $\pi/4$ rad to each other, this is equivalent to $\pi/2$ distance between the eigenmodes on the Poincaré sphere. The arrangement can also be thought as a combination of a phase shifter $\mathcal{P}(V_P)$ followed by a mode converter $\mathcal{M}(V_M)$ with (according to equation 2.25 and 2.26)

$$\mathcal{P}(V_P) = \cos\frac{1}{2}\frac{V_P}{V_{P,\pi}} + \mathbf{i}\sin\frac{1}{2}\frac{V_P}{V_{P,\pi}}, \quad (3.5a)$$

$$\mathcal{M}(V_M) = \cos\frac{1}{2}\frac{V_M}{V_{M,\pi}} + \mathbf{j}\sin\frac{1}{2}\frac{V_M}{V_{M,\pi}}, \quad (3.5b)$$

where V_P, V_M are the normalized driving signals for the fiber squeezers and $V_{P,\pi}, V_{M,\pi}$ are the driving signals for π retardation. The total polarization transformation is

$$\begin{aligned}\mathcal{Q}(V_P, V_M) &= \mathcal{M}(V_M)\mathcal{P}(V_P) \\ &= \cos\frac{1}{2}\frac{V_M}{V_{M,\pi}}\cos\frac{1}{2}\frac{V_P}{V_{P,\pi}} + \mathbf{i}\cos\frac{1}{2}\frac{V_M}{V_{M,\pi}}\sin\frac{1}{2}\frac{V_P}{V_{P,\pi}} + \\ &\quad \mathbf{j}\sin\frac{1}{2}\frac{V_M}{V_{M,\pi}}\cos\frac{1}{2}\frac{V_P}{V_{P,\pi}} - \mathbf{k}\sin\frac{1}{2}\frac{V_M}{V_{M,\pi}}\sin\frac{1}{2}\frac{V_P}{V_{P,\pi}}. \end{aligned} \quad (3.6)$$

For ease of visualization, the quaternion components in the above equations are denoted as Q_0, Q_1, Q_2 and Q_3, where $\mathcal{Q}(V_P, V_M) = Q_0(V_P, V_M) + \mathbf{i}Q_1(V_P, V_M) + \mathbf{j}Q_2(V_P, V_M) + \mathbf{k}Q_3(V_P, V_M)$. The contour plots for these quaternion components are shown in figure 3.4 with V_P, V_M in the operation range of $1\ldots3$, corresponding to a retardation range (of the mode converter and phase shifter) of $\pi\ldots3\pi$.

From the contour plot of Q_0, it is obvious that $V_P = 2, V_M = 2$ is the "center point", any contour lines will circle this center point. The contour line with the longest perimeter

[1] Two fiber squeezers do not permit endless control, this arrangement is only given as an illustration.

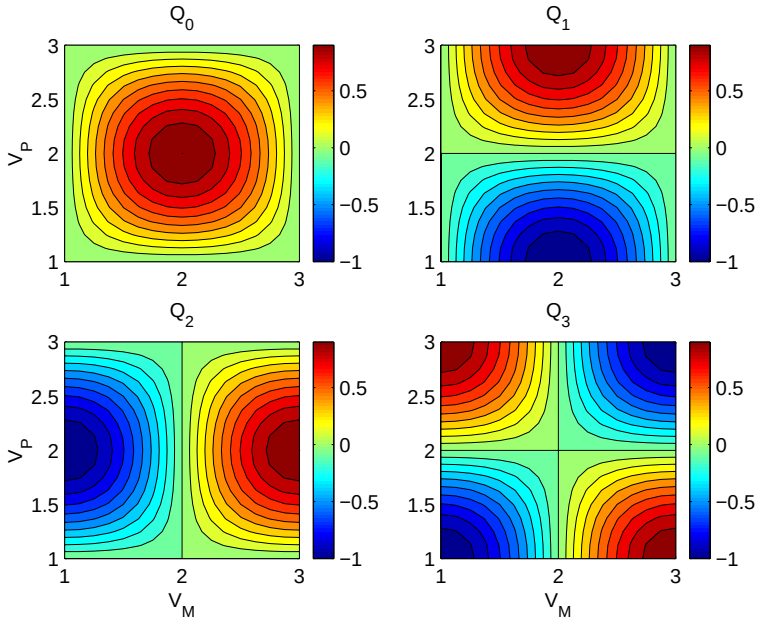

Figure 3.4: Contours of quaternion components of cascaded fiber squeezers

is $Q_0 = 0$ which is along the border of the contour plot. This particular contour line can also be specified by the parametric equation ($t = 0 \ldots 1$)

$$V_P(t) = 2 + (1 - |4t| + |4t - 1| + |4t - 2| - |4t - 3|), \tag{3.7a}$$
$$V_M(t) = 2 + (1 - |4t - 1| + |4t - 2| + |4t - 3| - |4t - 4|). \tag{3.7b}$$

This polarization transformer is then used in an automatic polarization control system where the input polarization state is circular. The driving signals $V_P(t), V_M(t)$ according to the above equation will transform the circular input polarization into a trajectory $R - V - L - H - R - P - L - Q - R$ as depicted in figure 3.5. If this trajectory is to be tracked by the controller (and assuming that the controller can track it perfectly), then it is the worst-case polarization state sequence for this type of polarization transformer since the accumulated driving signals (on the voltage plane V_P,V_M) reach the maximum value.

3.1.2 Linear Retarder Algorithm

A linear retarder, as described in subsection 2.1.2, has two parameters: the axis angle γ and the retardation φ. When using Poincaré sphere analysis, the double azimuth angle ψ is often used instead of the axis angle γ, with $\psi = 2\gamma$. The unit quaternion that represents a linear retarder is

$$\mathcal{L}(\psi, \varphi) = \cos\frac{\varphi}{2} + \mathbf{i}\sin\frac{\varphi}{2}\cos\psi + \mathbf{j}\sin\frac{\varphi}{2}\sin\psi. \tag{3.8}$$

Operation Principle

For polarization stabilization where either the input polarization or output polarization is fixed, a linear retarder is a natural choice for the polarization transformer. As shown geometrically in figure 2.6, a linear retarder with a retardation between 0 and π is

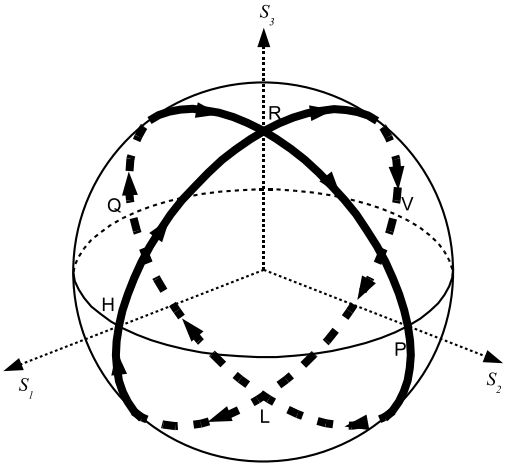

Figure 3.5: Worst-case tracking trajectory for a polarization controller using cascaded fiber squeezers

always able to transform a circular polarization to *any* elliptical polarization states and vice versa.

The controller for a linear retarder must continuously adjust both ψ and φ to maximize the feedback signal, typically using a gradient peak-search algorithm. In each iteration, the controller determines the gradients for ψ and φ which bring the intensity to its peak value [40, 67]. As described in Chapter 2, for a calibrated electro-optic linear retarder, ψ and φ can be determined by the electrode voltages and vice versa. It is thus possible (but not necessary) for the controller to directly dither (or modulate) the electrode voltages, obtain the partial derivative of the feedback signal with respect to the electrode voltages and then adjust the electrode voltages in the direction which maximizes the feedback signal [67, 68].

Reset Mechanism

An electro-optic linear retarder which is operated with a finite range of electrode voltages has a retardation limit, as previously mentioned in Chapter 2. If the retarder is used by an automatic polarization controller, at certain conditions reset must be carried out so that the electro voltages will not go out of range. This reset mechanism is illustrated graphically in figure 3.6.

The trajectory formed by the normalized electrode voltages V_1, V_2 (left) corresponds to the bold line on the Poincaré sphere (right), if the retarder has a right circular polarization at its input. The section $H - M_1$ brings the horizontal polarization into a state in the vicinity of the right circular polarization. The arc $M_1 - M_2 - M_3$, when compared to the quaternion plots of a linear retarder (2.10), realizes a *constant* retardation of $\pi - \triangle\varphi$ with $\triangle\varphi \approx 0$ and can be represented as

$$\mathcal{L}(\psi, \triangle\varphi) \approx \triangle\varphi/2 + \mathbf{i}\cos\psi + \mathbf{j}\sin\psi, \tag{3.9}$$

with $\psi = \pi/2 \ldots 3\pi/2$. This transforms a right circular polarization into polarization states with the approximated Stokes parameters $\begin{bmatrix} \triangle\varphi\sin\psi & \triangle\varphi\cos\psi & -1 \end{bmatrix}^T$. These polarization states circle the left circular polarization with a radius of $\triangle\varphi$. The output polarization continues to march to the vertical polarization state when the electrode voltages move from M_3 to V. In this last section, the electro voltages do not increase

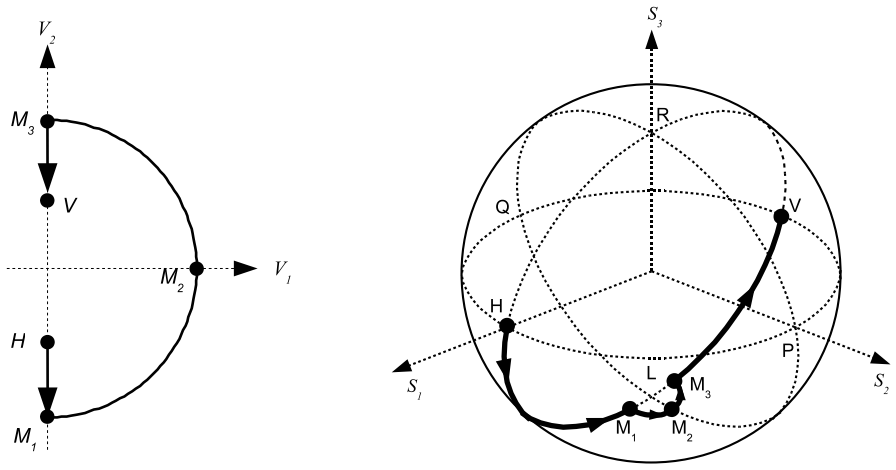

Figure 3.6: Reset scheme for the linear retarder algorithm

again and thus stay within the range.

For the case $\triangle\varphi = 0$, the arc $M_1 - M_2 - M_3$ corresponds to only one polarization state, namely the left circular polarization. This is the key to performing the reset step. When the controller must track the varying output polarization along the trajectory $H - L - V$, it must "rotate" the electro voltages along the half-circle arc so that the electro voltages do not go outside the operating range. As long as the reset is carried out quickly and the controller keeps the condition $\triangle\varphi = 0$, no polarization mismatch will occur because the retarder maintains the polarization transformation during the reset period.

This analysis also shows that (excluding the above reset procedure) the polarization states that circle the left circular polarization will be the worst-case tracking trajectory for this algorithm. The electrode voltages necessary to track this trajectory can be written parametrically ($t = 0 \ldots 1$) as

$$V_1(t) = \cos(2\pi t) - \triangle V, \tag{3.10a}$$
$$V_2(t) = \sin(2\pi t) - \triangle V, \tag{3.10b}$$

where $\triangle V \approx 0$ so that reset is not triggered yet. The tracking speed limit will be determined by the time needed by the controller to track this particular trajectory.

Since reset can affect the control speed, it must be appropriately handled. A strategy to speed up the reset procedure is by using two or more linear retarders in cascade. For a two-retarder configuration, this approach could be as simple as using the first retarder for transforming the input polarization as long as the retardation is within the limit and then switching to the second retarder whenever the first retarder is being reset. The controller will continue to use the second retarder until it needs reset and then the first retarder takes the main role of polarization transformation again [68].

3.1.3 Cascaded Fractional Waveplates Algorithm

A variable retarder formed by cascading a quarter-wave plate, a half-wave plate and a quarter-wave plate, all endlessly rotatable, is known to be able to perform arbitrary polarization transformation [36, 69]. For optimal response speed, the fractional wave-plates are typically realized as integrated optics [55]. They can also be implemented by cascading simpler types of retarders [70, 71].

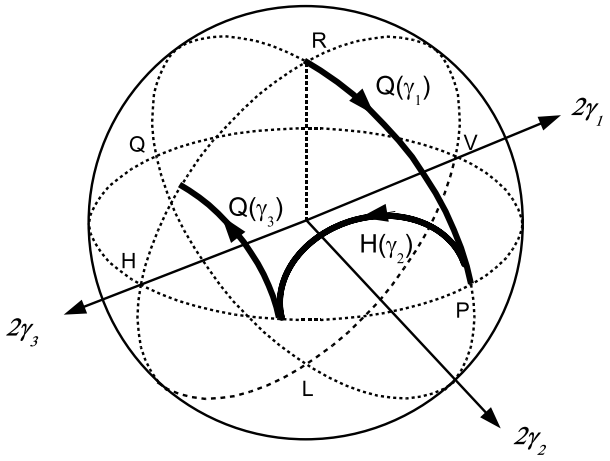

Figure 3.7: Transformation of a circular polarization by three fractional waveplates

Operation Principle

If each waveplate is *independently* adjustable, it gives a total number of three degree-of-freedom. Transformation from a static, arbitrary polarization into another static, arbitrary polarization however can be specified using only two degree-of-freedom, for example a rotation axis for a fixed non-zero rotation angle. Thus, there are many possible combinations of the waveplate orientations that correspond to a specific polarization transformation. The easiest is as follows: the first quarter-wave plate transforms the elliptical input polarization into a linear polarization, the half-wave plate rotates this linear polarization along the S_1S_2 great circle so that it can be transformed by the last quarter-wave plate to reach the target polarization.

If the rotations of the first quarter-wave plate, the half-wave plate and the second quarter-wave plate are denoted as $\mathcal{Q}(\gamma_1)$, $\mathcal{H}(\gamma_2)$, and $\mathcal{Q}(\gamma_3)$, respectively, then based on equation 2.17 and 2.18, the total transformation is

$$\mathcal{R}(\gamma_1,\gamma_2,\gamma_3) \;=\; \mathcal{Q}(\gamma_3)\mathcal{H}(\gamma_2)\mathcal{Q}(\gamma_1). \tag{3.11}$$

Straightforward but lengthy quaternion multiplications yield

$$\begin{aligned}\mathcal{R}(\gamma_1,\gamma_2,\gamma_3) \;=\;& \mathbf{i}(\cos 2\gamma_2 - \cos(2\gamma_1 - 2\gamma_2 + 2\gamma_3))/2 + \\ & \mathbf{j}(\sin 2\gamma_2 - \sin(2\gamma_1 - 2\gamma_2 + 2\gamma_3))/2 + \\ & \mathbf{k}(\sin(2\gamma_1 - 2\gamma_2) + \sin(2\gamma_2 - 2\gamma_3))/2 + \\ & (-\cos(2\gamma_3 - 2\gamma_2) - \cos(2\gamma_2 - 2\gamma_1))/2.\end{aligned} \tag{3.12}$$

Figure 3.7 shows an example of the polarization transformation by the waveplates $\mathcal{Q}(\gamma_1)$, $\mathcal{H}(\gamma_2)$, $\mathcal{Q}(\gamma_3)$, with $\gamma_1 = \pi$, $\gamma_2 = 11\pi/32$, and $\gamma_3 = 0$.

In some experiments, the last quarter-wave plate is rotated *synchronously* with the first quarter-wave plate so that $\gamma_3 = \gamma_1 + \pi/2$ [72, 73]. The whole arrangement now has only two degree-of-freedom. In this case, the total transformation of the cascaded wave-plates is simplified to

$$\begin{aligned}\mathcal{R}(\gamma_1,\gamma_2) \;=\;& \mathbf{i}\cos(2\gamma_2 - 2\gamma_1)\cos 2\gamma_1 + \\ & \mathbf{j}\cos(2\gamma_2 - 2\gamma_1)\sin 2\gamma_1 + \\ & -\mathbf{k}\sin(2\gamma_2 - 2\gamma_1).\end{aligned} \tag{3.13}$$

The above unit quaternion represents a rotation of φ around the axis $\mathbf{\Omega}$ according to

$$\varphi = \pi, \tag{3.14a}$$

$$\mathbf{\Omega} = \begin{bmatrix} \cos(2\gamma_2 - 2\gamma_1)\cos 2\gamma_1 \\ \cos(2\gamma_2 - 2\gamma_1)\sin 2\gamma_1 \\ -\sin(2\gamma_2 - 2\gamma_1) \end{bmatrix}. \tag{3.14b}$$

The retarder acts like a generalized half-wave plate. Its rotation axis $\mathbf{\Omega}$ is endlessly rotatable. It depends on γ_1, γ_2 which do not have any limit and hence require no unwinding.

In another experiment, the quarter-wave plates are rotated *simultaneously* so that $\gamma_3 = \gamma_1$ [69]. This simplifies the total transformation of the cascaded wave-plates to

$$\begin{aligned} \mathcal{R}(\gamma_1, \gamma_2) = {} & \mathbf{i}\sin(2\gamma_2 - 2\gamma_1)\sin 2\gamma_1 + \\ & \mathbf{j}\sin(2\gamma_2 - 2\gamma_1)\cos 2\gamma_1 - \\ & \cos(2\gamma_2 - 2\gamma_1). \end{aligned} \tag{3.15}$$

The above unit quaternion represents a rotation of φ around the axis $\mathbf{\Omega}$ according to

$$\varphi = 2\pi - (4\gamma_1 - 4\gamma_2), \tag{3.16a}$$

$$\mathbf{\Omega} = \begin{bmatrix} \sin 2\gamma_1 \\ -\cos 2\gamma_1 \\ 0 \end{bmatrix}. \tag{3.16b}$$

Here, the retarder acts like a linear retarder with endlessly rotatable eigenmode. The retardation is adjustable via γ_1, γ_2 in the whole range of $0 \ldots 2\pi$.

When the retarder is used in a polarization control system, each waveplate is typically adjusted *independently*, either by an analog lock-in amplifier [72] or a digital feedback controller [73, 69], to maximize (or minimize) the feedback signal. The digital controller is preferred because it is much faster than the analog counterpart.

Simplification for Polarization Tracking with Fixed Input

For polarization tracking with either a fixed input polarization or a fixed output polarization, two quarter-wave plates are sufficient to perform the necessary endless transformation. For example, a quarter-wave plate followed by a half-wave plate can transform a varying input polarization into a fixed linear output polarization [46, 74]. Here it is shown that *with a circular input polarization*, an arbitrary output polarization can be reached by a cascade of only two quarter-wave plates. Transformation of a circular polarization by a quarter-wave plate and a half-wave plate is always a linear polarization, described as

$$H(\gamma_2)\mathcal{Q}(\gamma_1)\mathbf{k}\mathcal{Q}^*(\gamma_1)H^*(\gamma_2) = \begin{bmatrix} -\sin(4\gamma_2 - 2\gamma_1) \\ \cos(4\gamma_2 - 2\gamma_1) \\ 0 \end{bmatrix}. \tag{3.17}$$

Therefore, the cascaded waveplates $H(\gamma_2)\mathcal{Q}(\gamma_1)$ can be replaced by just a single quarter-wave plate $\mathcal{Q}(\widetilde{\gamma_1})$ where

$$\widetilde{\gamma_1} \quad = \quad \pi + 2\gamma_2 - \gamma_1. \tag{3.18}$$

The arrangement $\mathcal{Q}(\gamma_1)$, $\mathcal{H}(\gamma_2)$, and $\mathcal{Q}(\gamma_3)$ is now simplified to $\mathcal{Q}(\widetilde{\gamma_1})$ and $\mathcal{Q}(\gamma_3)$ only. The total transformation is

$$\begin{aligned}\mathcal{R}(\widetilde{\gamma_1}, \gamma_3) \quad = \quad & \frac{1}{2} - \frac{1}{2}\cos(2\widetilde{\gamma_1} - 2\gamma_3) + \frac{1}{2}\mathbf{i}(\cos 2\widetilde{\gamma_1} - \cos 2\gamma_3) + \\ & \frac{1}{2}\mathbf{j}(\sin 2\widetilde{\gamma_1} - \sin 2\gamma_3) + \frac{1}{2}\mathbf{k}\sin(2\widetilde{\gamma_1} - 2\gamma_3).\end{aligned} \tag{3.19}$$

Controller Dead Lock

The use of fractional waveplates with one control loop for each waveplate however present a practical problem. There are always polarization states where the feedback signal is *insensitive* or *less sensitive* to the dithering of one control variable [75]. Such polarization states are often called "dead spots".

For the retarder as described by equation 3.13, when $\gamma_2 = \gamma_1 - \triangle\gamma/2$ with $\triangle\gamma \approx 0$, the transformation of the retarder is approximated as

$$\mathcal{R}(\gamma_2, d\gamma) \quad \approx \quad \mathbf{i}\cos 2\gamma_2 + \mathbf{j}\sin 2\gamma_2 + \mathbf{k}\triangle\gamma. \tag{3.20}$$

The rotation axis of the retarder lies on the S_1S_2 great circle, its azimuth depends on γ_2 . A right circular polarization is rotated by the retarder to

$$\mathcal{R}(\gamma_2, \triangle\gamma)\mathbf{k}\mathcal{R}^*(\gamma_2, \triangle\gamma) \quad = \quad \begin{bmatrix} 2\triangle\gamma\cos 2\gamma_2 \\ 2\triangle\gamma\sin 2\gamma_2 \\ \triangle\gamma^2 - 1 \end{bmatrix}. \tag{3.21}$$

It is very close to the left circular polarization. The controller is to track an elliptical polarization with azimuth $\theta = 0$ and ellipticity $\epsilon = -\pi/4 + \triangle\epsilon/2$ with $\triangle\epsilon \approx 0$, which has the corresponding (approximated) Stokes vector $\begin{bmatrix} \triangle\epsilon & 0 & \triangle\epsilon^2/2 - 1 \end{bmatrix}^T$. The feedback signal is thus

$$\begin{aligned} I(\gamma_2) \quad &= \quad (1 + \begin{bmatrix} \triangle\epsilon & 0 & \triangle\epsilon^2/2 - 1 \end{bmatrix} \begin{bmatrix} 2\triangle\gamma\cos 2\gamma_2 \\ 2\triangle\gamma\sin 2\gamma_2 \\ \triangle\gamma^2 - 1 \end{bmatrix})/2 \\ &= \quad 1 + \triangle\epsilon\triangle\gamma\cos 2\gamma_2 + (\triangle\epsilon^2\triangle\gamma^2/2 - \triangle\gamma^2 - \triangle\epsilon^2/2)/2. \end{aligned} \tag{3.22}$$

Dithering the orientation axis of the half-wave plate (γ_2, together with γ_1) has the purpose of getting the derivative of the feedback signal with respect to γ_2. This can be found from the above equation as

$$\frac{\partial I(\gamma_2)}{\partial \gamma_2} \quad = - \quad \triangle\epsilon\triangle\gamma\sin 2\gamma_2. \tag{3.23}$$

In this case, because $\triangle\gamma \approx 0$ and $\triangle\epsilon \approx 0$, dithering γ_2 produced very little change in the feedback signal which possibly can not be detected properly by the electronic circuit. In addition, the controller may cease to work ("dead lock") as $\partial I(\gamma_2)/\partial\gamma_2$ approaches zero. The worst case is when γ_2 is orthogonal to the optimal orientation axis but can not be corrected by the controller because the factor $\sin 2\gamma_2$ vanishes and $\partial I(\gamma_2)/\partial\gamma_2 = 0$.

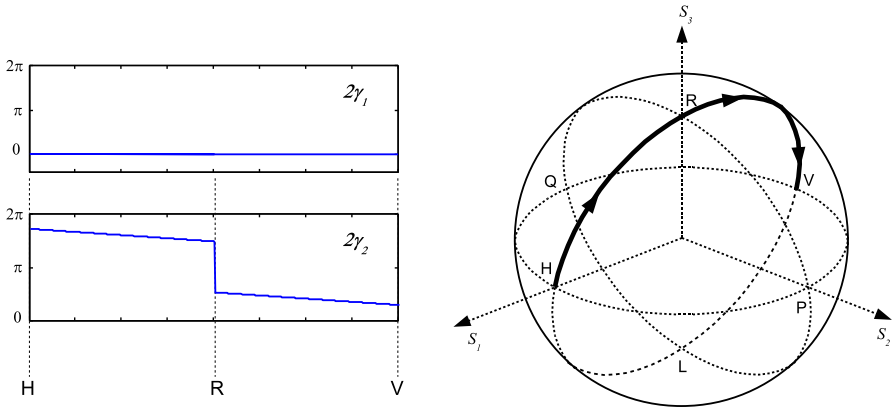

Figure 3.8: Reset scheme for the cascaded fractional waveplates algorithm

Reset Mechanism

The arrangement of fractional waveplates is often claimed to be *reset-free* [69, 72, 73]. This stems from the fact that not a single waveplate needs any unwinding. However, according to the definition of reset described previously, the algorithm that uses this waveplates arrangement is not necessarily reset-free [38, 65]. Abrupt changes in waveplates parameters are still possible under certain circumstances. One example is illustrated graphically in figure 3.8. The trajectory formed by the retarder parameters γ_1, γ_2 (left) corresponds to the bold line on the Poincaré sphere (right), if the waveplates has a left circular polarization at its input and $\gamma_3 = \gamma_1 + \pi/2$. When the controller must track the varying output polarization along the trajectory $H-R-V$ and initially $\gamma_1 = 0, \gamma_2 = 7\pi/4$, it must rapidly change γ_2 by $\pi/2$ just when the output polarization passes the right circular. This proves that the waveplates arrangement *is not reset-free*. It could be shown that the same condition applies for the simplified arrangement of waveplates as described in equation 3.19.

For the case $\gamma_3 = \gamma_1$, the retarder becomes a linear retarder (equation 3.15). Therefore, it subjects to the same limitation and reset mechanism as in the linear retarder algorithm. Again, it means that this arrangement of waveplates ($\gamma_3 = \gamma_1$) is also *not reset-free*.

Tracking Speed Limit

For the case $\gamma_3 = \gamma_1 + \pi/2$, reset is necessary when the input polarization needs to be rotated into target polarization states in the vicinity of its orthogonal. Without loss of generality, the input polarization can be assumed to be right circular and the target polarization states reside on a very small circle with a radius of $\triangle\epsilon \approx 0$ centered at the left circular polarization. Such polarization states have an ellipticity $\epsilon = -\pi/4 + \triangle\epsilon/2$ and can be represented by the Stokes vector $\begin{bmatrix} \triangle\epsilon\cos\alpha & \triangle\epsilon\sin\alpha & \triangle\epsilon^2/2 - 1 \end{bmatrix}^T$ for $\alpha = 0 \ldots 2\pi$. For the retarder as described in equation 3.20, at the points where $\triangle\epsilon/2 \approx \triangle\gamma$, the optimal control variables should be set to

$$\gamma_1 \approx \alpha/2, \tag{3.24a}$$

$$\gamma_2 \approx \alpha/2. \tag{3.24b}$$

The controller must rotate γ_1, γ_2 in the range of $0 \ldots \pi$ for $\alpha = 0 \ldots 2\pi$. As shown in the previous chapter, rotating the axis of a calibrated electro-optic quarter-wave plate

by π (by 2π on the Poincaré sphere) means driving the electrode voltages up to $\pm 30\,V$. For a half-wave plate, the necessary driving voltages are doubled. This is the case even for an infinitesimal $\triangle\epsilon$. A similar problem arises for $\gamma_3 = \gamma_1$ configuration.

3.2 FPGA-Based Controller Implementation

Because of their complexity, polarization control algorithms are typically implemented in digital circuits. There have been reports on digital realization of polarization stabilization using a microprocessor [67], a combination of basic digital blocks [73] and a dedicated digital signal processor [61]. In this dissertation, an implementation of polarization control algorithm in a *field programmable gate array* (FPGA) is described. An FPGA is chosen because it allows a very fast execution of the control algorithm. In addition, it also offers a high degree of parallelism, a feature which can be utilized to implement the tracking algorithm efficiently.

3.2.1 Hardware Components

Several hardware components are needed to implement a polarization controller digitally. The feedback signal (that is, the photo intensity) must be detected by a photo detection circuit and then converted using an *analog-to-digital converter* (ADC) to the discrete binary representation. The driving signal from the controller must be converted using a *digital-to-analog converter* (DAC) so that it can drive the lithium-niobate linear retarder. For faster operation, more than one retarder is used and therefore several DACs are required. For an ultra-fast polarization tracking, the conversion speed and the performance of the ADC and the DACs play an important role.

The controller is implemented in a Xilinx Spartan-3 XC3S1000 FPGA [76]. It comprises 1920 *configurable logic blocks* (CLBs). One block has 8 logic cells, each cell can be flexibly programmed to perform combinational and sequential logic. In total, the logic capability of the Spartan-3 XC3S1000 is equivalent to approximately a million logic gates. For a limited amount of data storage, the Spartan-3 also offers two types of *random access memory* (RAM): distributed RAM [77] and block RAM [78]. In a Spartan-3 XC3S1000 chip, up to 120 Kbits of distributed RAM and 432 Kbits of block RAM are available. In addition, Spartan-3 XC3S1000 has 24 dedicated single-cycle 18-bit hardware multipliers [79] which are useful to carry out complicated calculations.

For development convenience, a prototyping board XSA-3S1000 [80] is used. The prototyping board is equipped with a Spartan-3 XC3S1000 FPGA and two external memory chips: 32 Mbyte synchronous dynamic RAM (Samsung K4S561632ETC75 [81]) and 2 MB Flash RAM (Spansion S29AL016M10TAI020[82, 83]). A video connector and a parallel port are also available on the prototyping board.

The setup for the hardware of the polarization controller is shown schematically in figure 3.9. The ADC and the DACs are connected to the input/output pins of the Spartan-3 FPGA. For troubleshooting and debugging, a video graphics array (VGA) monitor and a computer (or a notebook) are connected to the XSA-3S1000 board through the video connector and parallel port, respectively. The monitor is used to display the status of the controller wheres the computer is important to retrieve additional information and changing the operation of the controller.

The hardware of this polarization controller consists of affordable commercial, off-the-shelf components only. This reduces both the development time and cost. Figure 3.10 shows the picture of the actual controller setup.

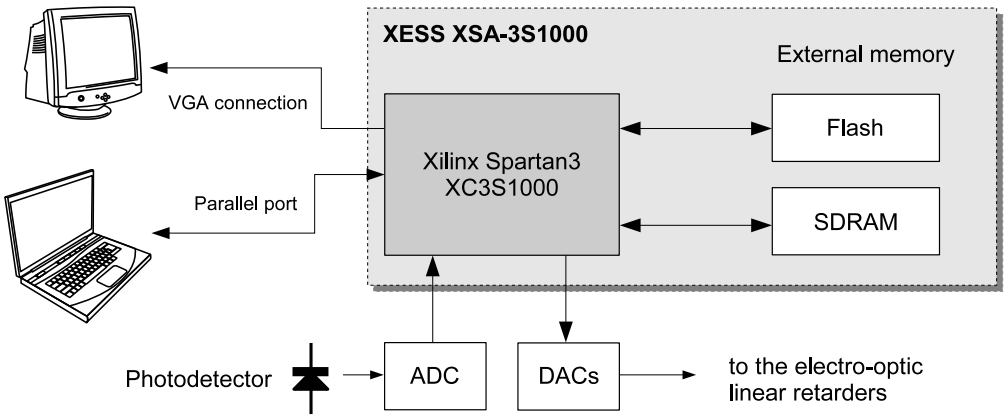

Figure 3.9: Schematic diagram of the hardware

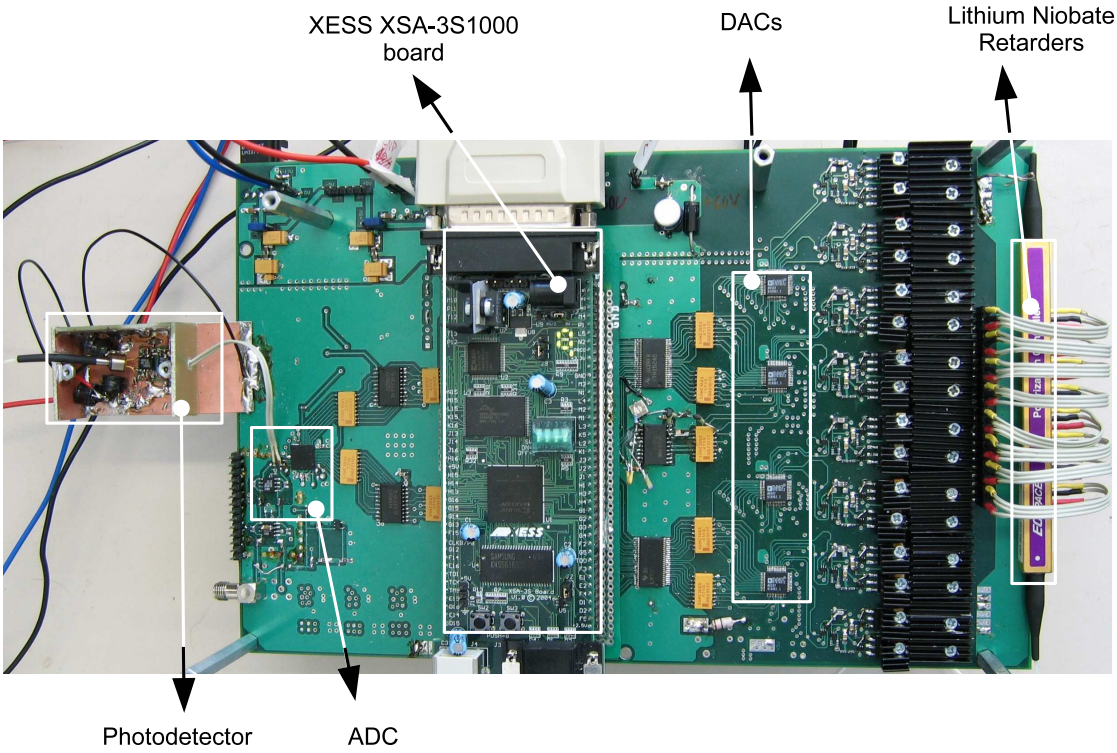

Figure 3.10: Picture of the controller setup

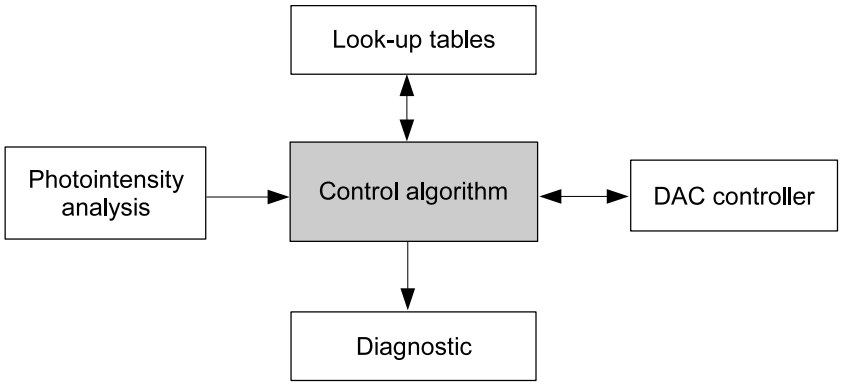

Figure 3.11: Schematic diagram of the control software

3.2.2 Software Modules

The polarization stabilization is implemented in software running on the Spartan-3 FPGA. Figure 3.11 shows the simplified architecture of the software. It is designed to be modular for ease of development and maintenance. Hardware interfacing to the ADC, the DACs and VGA monitor are separated into different modules which allows abstractions and simplification of the main program. Each module is programmed in VHDL (VHSIC[2] hardware description language).

Gradient Descent Controller

The controller implements the linear retarder algorithm (subsection 3.1.2). For the gradient descent method, the controller dithers the driving signals (electrode voltages of the retarders) and measures the intensity to infer the gradient. To reach a maximum performance, the code to perform the gradient algorithm is optimized to get the shortest possible execution time and thus is clocked at 50 MHz (20 ns cycle period). As the result, one control iteration can be carried out in just 7 µs. A later improved version of the code even cuts the iteration time down to 3.5 µs. An even more optimized version brings the iteration time to only 2 µs. This corresponds to polarization tracking up to 140000 iterations/second, 285000 iterations/second, and 500000 iterations/second, respectively. Each iteration is designed to correct $\leq$1 rad of polarization mismatch.

Look-Up Tables

The electro-optic linear retarders used in the controller are characterized and calibrated using the method described in Chapter 2. The calibration data are important for the controller since it allows the control algorithm to treat the utilized retarders as one ideal linear retarder. In this implementation, the calibration data are stored in the memory, not hard-coded in the program. It makes it easy to substitute the electro-optic retarders without the need to modify the program. Because of the size of the data, the program makes use of all types of memory available on the prototyping board: Flash, SDRAM, Block RAM. Flash is important because it is non-volatile and hence it retains the written data even when the system is not powered. SDRAM is slow but it has a big capacity, whereas Block RAM can store only a very limited amount of data but is nevertheless very fast. A combination of these three memory types allows the controller to manage the calibration data effectively.

[2]Very-High-Speed Integrated Circuits

The calibration data is stored in the form of look-up tables [84]. Because the memory capacity is finite, each look-up table has a coarse resolution (granularity). A fast two-dimensional interpolation is carried out to improve the accuracy. For a two dimensional function $f(x, y)$, the look-up table is in the form of $f(x_n, y_n)$ where $x_n, y_n = 1, 2, 3, ...N$ and the linear interpolation is

$$\begin{aligned} f(x,y) \quad \approx \quad & (1-y+y_n)(1-x+x_n)f(x_n,y_n) + \\ & (1-y+y_n)(x-x_n)f(x_n+1,y_n) + \\ & (y-y_n)(1-x+x_n)f(x_n,y_n+1) + \\ & (y-y_n)(x-x_n)f(x_n+1,y_n+1), \end{aligned} \tag{3.25}$$

with $x_n \leq x < x_n + 1$ and $y_n \leq y < y_n + 1$. If $x_u = x - x_n$ and because x_n is an integer, x_u is simply the fractional part of x. If $x_v = 1 - x + x_n$, then x_v is obtained by using the relation $x_u + x_v = 1$. Thus, this approximation is implemented by using the most significant bits of x, y as indices to the table and the rest of the bits for the interpolation.

A less accurate but faster version

$$f(x,y) \quad \approx \quad f(x_n,y_n) + (x-x_n)\frac{\partial f(x,y)}{\partial x} + (y-y_n)\frac{\partial f(x,y)}{\partial y}, \tag{3.26}$$

where $\partial f(x, y)/\partial x, \partial f(x, y)/\partial y$ are precomputed off-line, is also used under certain circumstances.

Photointensity Analysis

The photodetection circuit and the corresponding ADC deliver the feedback signal to the control algorithm. To reduce the effect of the measurement noise, the ADC is clocked at a frequency 50 MHz that is faster than the dithering in the gradient descent controller. The measured photointensity is downsampled before being processed by the controller.

To analyze the tracking performance of the controller, the photointensity is analyzed in a histogram module. The histogram module counts the "occurrences" for various photointensities. The result can be retrieved from a computer/notebook. If this is carried out during a continuous polarization tracking, the amount of polarization mismatch can be concluded by the probability density function of the intensity.

For the characterization purpose (as described in subsection 2.2.4), it is necessary to record the photointensity at the highest possible sampling frequency. When this is performed for a duration of several milliseconds, the amount of the sampled data is quite large. Thus, the data can be saved only to the SDRAM which has a massive total capacity of 32 MB. This however presents a challenge because the SDRAM can not continuously be written due to its intermittent refresh procedure. The refresh of the SDRAM can be as long as 120 ns and occurs at least every 8 µs. The solution is to use a cache buffer [85] between the ADC and the SDRAM, as depicted in figure 3.12. The RAM controller always tries to fill the SDRAM as fast as possible but whenever the SDRAM is in the "busy" state (while performing the refresh), the samples are temporarily stored in the buffer. This buffer will be quickly emptied as soon as the SDRAM finishes with the refresh. This caching technique allows storing the photointensity (from the ADC) to the SDRAM at a constant rate of up to 25 MHz.

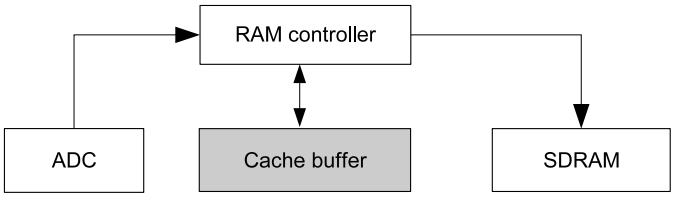

Figure 3.12: Buffering to overcome SDRAM refresh

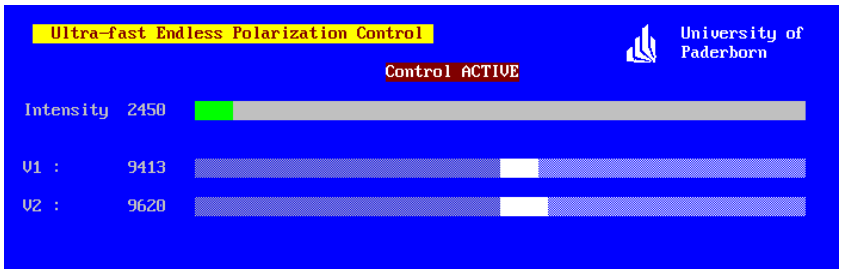

Figure 3.13: Screenshot of the status information

Troubleshooting

Two means for troubleshooting are built in the control program: remote debugging and status information. For remote debugging, the program can communicate to a client tool running on a computer/notebook connected to the controller hardware using a parallel port. This is useful in the early stage of development, for example to verify the result of the calculation performed on the FPGA (programmed in VHDL) and compare it against the reference version (written as MATLAB script). Data transfer is done using a compact and error-tolerant protocol. However, the speed is limited by the parallel port interface so it does not permit real-time monitoring.

To display the important status of the controller, a video controller module has been developed. This module sends VGA-compatible signals to an external monitor. The photointensity and the electrode voltages of the retarders can be observed on the monitor, as shown in figure 3.13.

3.3 Tracking Experiments

3.3.1 Experiment Setup

The speed of a polarization controller can be objectively measured when the controller is stabilizing rapidly varying polarization states. Random changes to polarization state are possible to realize by passing a fixed polarization through a *polarization scrambler*.

Figure 3.14 shows the structure of a simple polarization scrambler using cascaded rotating fractional waveplates. The quarter-wave plates were made from endlessly rotatable fiber loops. A stepper motor was used to drive each fiber loop, the speed and direction were determined by the microcontroller-based driving circuit. The quarter-wave plates run at different rates between –6 Hz and +6 Hz. The half-wave plate was made from a commercial bulk optic waveplate and rotated by a DC motor. It can reach a maximum speed of 23000 rotations per minute.

The maximal polarization rotation speed is obtained when a linear polarization passes the half-wave plate. Without loss of generality, assuming this linear polarization is a

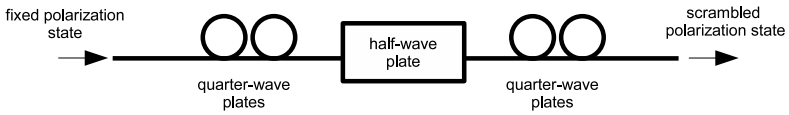

Figure 3.14: Polarization scrambler using rotating waveplates

horizontal polarization, after rotated by the half-wave plate it becomes (obtained using equation 2.18)

$$H(\gamma)\mathbf{i}H^*(\gamma) \quad = \quad \begin{bmatrix} \cos 4\gamma \\ \sin 4\gamma \\ 0 \end{bmatrix}. \tag{3.27}$$

Within one revolution of the half-wave plate, γ changes from 0 to 2π and the horizontal input polarization is transformed into a linear polarization that traces the S_1S_2 great circle (on the Poincaré sphere) with an azimuth angle from 0 to $4(2\pi)$. This means, when the half-wave plate is rotated at the rate of 280 Hz, it causes a maximal polarization change of 7000 rad/s on the Poincaré sphere. Practically, the polarization change does not always reach the maximal speed at all times since the polarization state at the input of the half-wave plate is not always linear. The quarter-wave plates in front of the half-wave plate distribute the polarization states on the Poincaré sphere and thus vary the total polarization rotation speed. The additional quarter-wave plates after the half-wave plate ensure that the rotation trajectories seen by the polarization controller are randomly reoriented. Figure 3.15 shows the result of the rotating waveplates simulation. The polarization changes distribution function (top) and its complementary cumulative distribution function (bottom) indicate that the mean of the polarization changes is indeed about 5500 rad/s and most of the time almost maximum polarization changes are generated by rotating waveplates.

Figure 3.16 shows the scrambling result on the Poincaré sphere, taken with a polarimeter in a time period of 5 minutes. With polarization changes up to 100 rad/s (left), the trajectories are still visible. However, with very fast scrambling up to 3600 rad/s (right), the Poincaré sphere is filled only with points because the sampling rate of the polarimeter is too slow compared to the scrambling speed. This validates the operation of the polarization scrambler.

The performance of the polarization controller was analyzed using the setup shown in figure 3.17 (top). An optical signal from a laser at 1551 nm was passed through the polarizer, the polarization controller and then the polarization scrambler. The feedback signal for the controller was obtained after the polarization beam splitter (PBS) and an optical attenuator. The controller was set to minimize this feedback signal. Here a PBS was used instead of a polarizer so that the maximized optical signal was available at the other output of the PBS as well. The attenuator was inserted because the photodetector circuit was able to work with a maximum of -11 dB optical power. Instead of an attenuator, an optical coupler (5% or 10%) could also be used if both outputs of the PBS are needed, for example in a polarization demultiplex system.

To verify the gradient algorithm in the digital controller, first the scrambler was turned off and its waveplates were manually adjusted until a maximum feedback signal was obtained. The output of the PBS was connected to a polarimeter for monitoring purpose. The polarization controller was deliberately modified until its control speed was only one iteration per second. The controller was then enabled and it automatically transformed

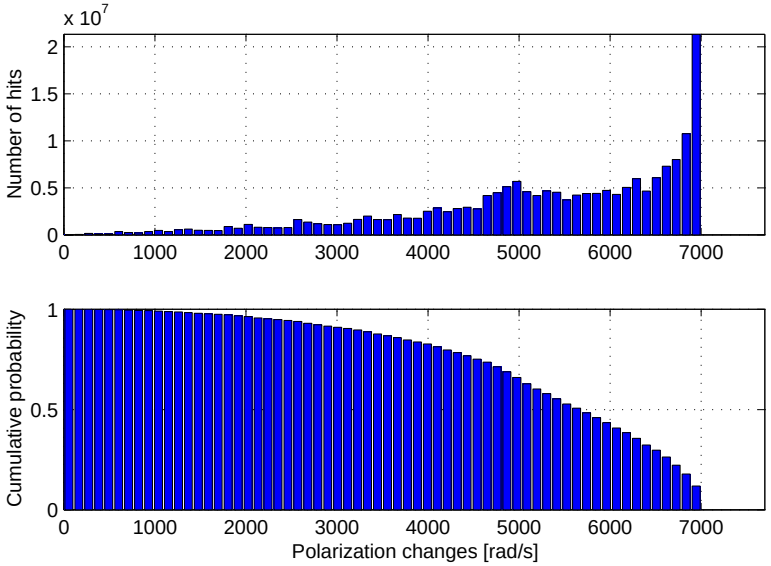

Figure 3.15: Distribution function (top) and complementary cumulative distribution function (bottom) of the polarization changes

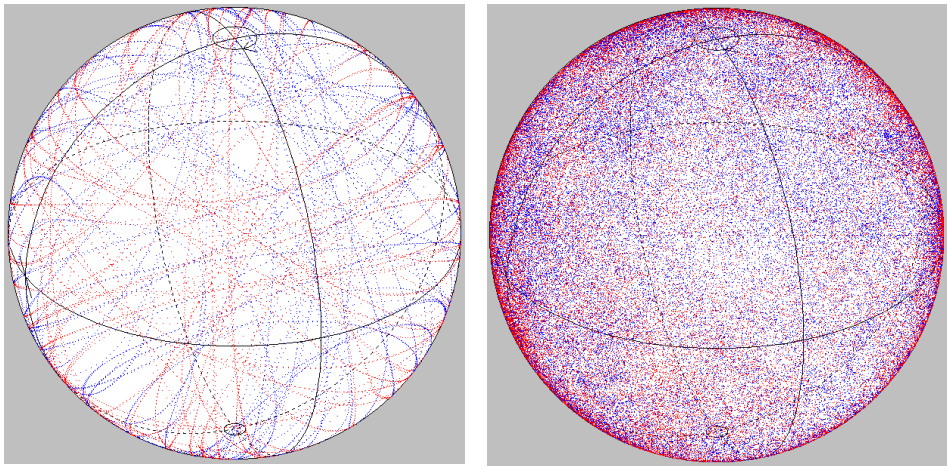

Figure 3.16: Poincaré sphere with scrambling up to 100 rad/s (left) and 3600 rad/s (right)

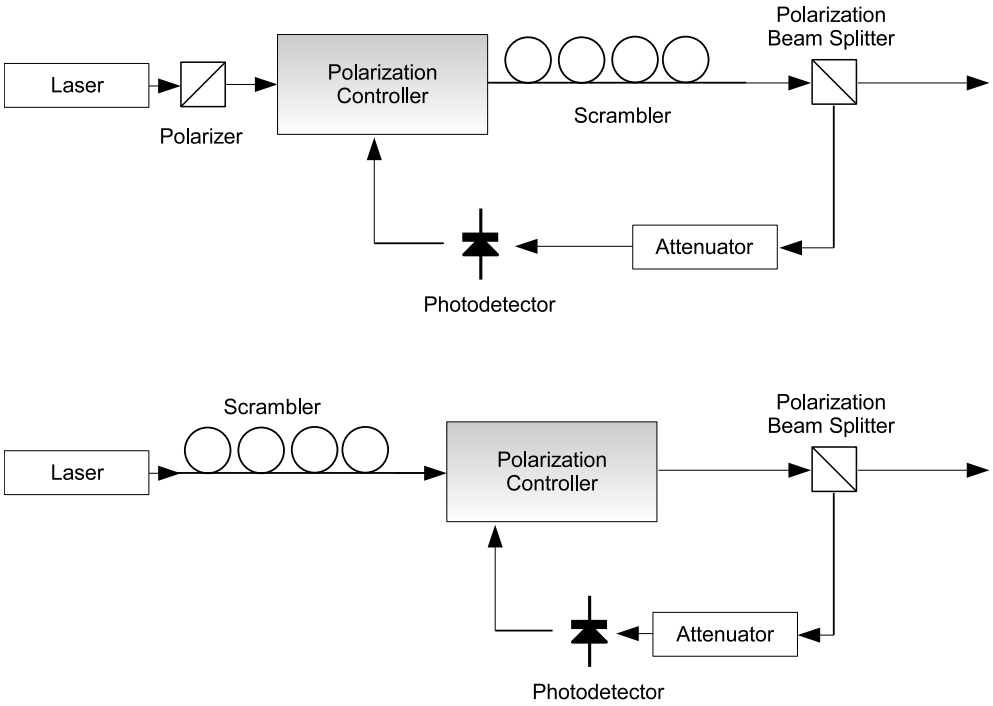

Figure 3.17: Polarization tracking experiment setup with varying output polarization (top) and varying input polarization (bottom)

the polarization until the feedback signal reached its minimum point. Due to the slow control speed of the controller, the changes of the control voltages could be observed clearly and this is used to confirm the tracking of the controller [84].

The controller was brought back to its maximum control speed. The scrambler was switched on and set to produce polarization rotation up to 3600 rad/s on the Poincaré sphere. The performance of the controller was checked on the polarimeter. Figure 3.18 shows the difference in the polarization changes on Poincaré sphere when the controller is inactive (left) and active (right), taken in a time period of 5 minutes. Without any control, the Poincaré sphere was randomly filled with points. With automatic control, the polarization states were successfully confined in a circle with an approximate radius of only 0.1 rad.

The experiment setup was modified to check the controller for stabilizing a varying output polarization, as in figure 3.17 (bottom). With polarization scrambling and active control, essentially identical result was obtained. That is, the stabilized polarization states were within a 0.1 rad radius circle on the Poincaré sphere.

3.3.2 Tracking Results

The experiment setup was used to test the performance of the FPGA-based polarization controller, for the "slow" version (7 µs iteration time), the "fast" version (3.5 µs iteration time), and the "ultrafast" version (2 µs iteration time), for different scrambling speeds. The maximum tracking error could not be determined using the polarimeter because the polarimeter was too slow to catch the fastest glitches. Therefore, the feedback signal received by the digital controller was recorded every 1.4 µs and then analyzed. For each scrambling configuration, the intensity analysis was carried out for a 30 minutes' continuous tracking. The maximum tracking speed was determined by the scrambling

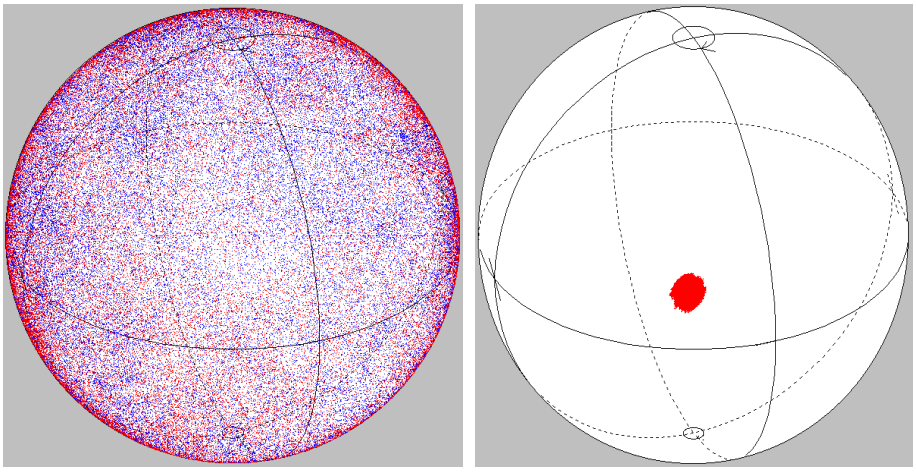

Figure 3.18: Poincaré sphere when controller is inactive (left) and active (right)

speed for which the intensity error did not exceed 1%.

5000 rad/s Tracking Experiment [86, 87]

With 7 µs control iteration time, the test was conducted with a rotation rate of the half-wave plate up to 200 Hz. Figure 3.19 shows the cumulative density function $F(I)$ of the intensity, that is, the time-averaged probability that the intensity becomes worse than the value given in the abscissa. The intensity measurement error was not excluded, as shown by the reference measurement without light (optical signal), which indicated that the true results were likely to be better. For a half-wave plate (HWP) rotation rate of 200 Hz (polarization changes up to 5000 rad/s), the controller was able to perform tracking with a maximum intensity error of <1%. The probability that the intensity error was larger than 0.73% was only 1%. Even with a half-wave plate rotation rate of 280 Hz (polarization changes up to 5000 rad/s) the controller can still perform the tracking although the maximum intensity error >1% was reached. In figure 3.20, the intensity error (right scale) and the corresponding calculated polarization error (left scale) are displayed as a function of the maximum polarization changes. The mean polarization error was always <0.063 rad. At 5000 rad/s, the maximum polarization and intensity errors were 0.17 rad and 0.73%, respectively. For the maximized signal exiting at the other PBS output, this corresponds to a loss of $-10 \cdot \log(1 - (< 0.0073)) =< 0.032$ dB.

9000 rad/s Tracking Experiment [88]

A faster version of the software, with 3.5 µs iteration time, was also tested using the experiment setup. Since now the controller is twice as fast, the maximum rotation rate of the half-wave plate was doubled as well.

Figure 3.21 shows the cumulative density function $F(I)$. For a half-wave rotation of 360 Hz (polarization changes up to 9000 rad/s), the controller was able to perform tracking with a maximum intensity error of <0.5%. The probability that the intensity error was larger than 0.25% was only 1%. In figure 3.22, the intensity error (right scale) and the corresponding calculated polarization error (left scale) are displayed as a function of the maximum polarization changes. The mean polarization error was always < 0.06 rad. At 9000 rad/s, the maximum polarization and intensity errors were 0.13 rad and 0.43%, respectively. For the maximized signal exiting at the other PBS output, this

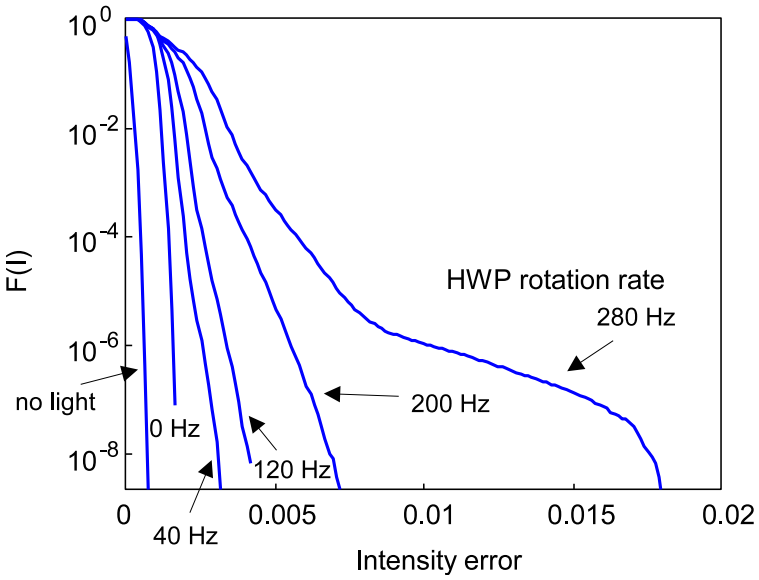

Figure 3.19: Cumulative intensity distribution function during polarization tracking with 7 µs iteration time

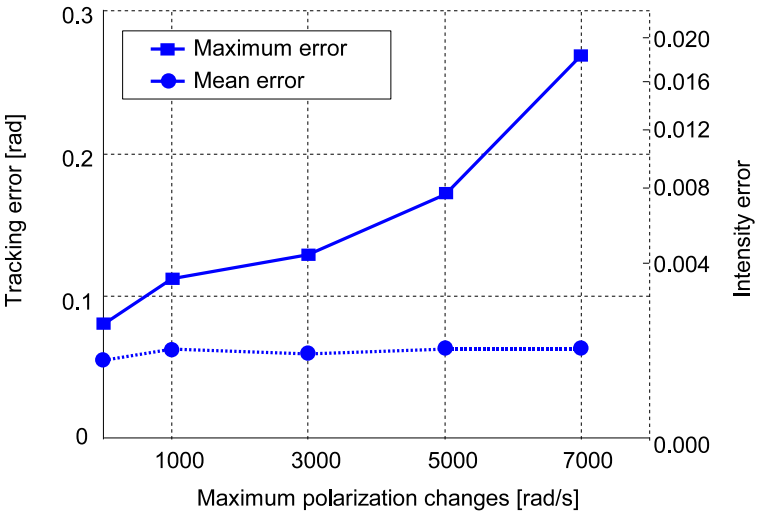

Figure 3.20: Tracking error for different polarization changes (with 7 µs control iteration time)

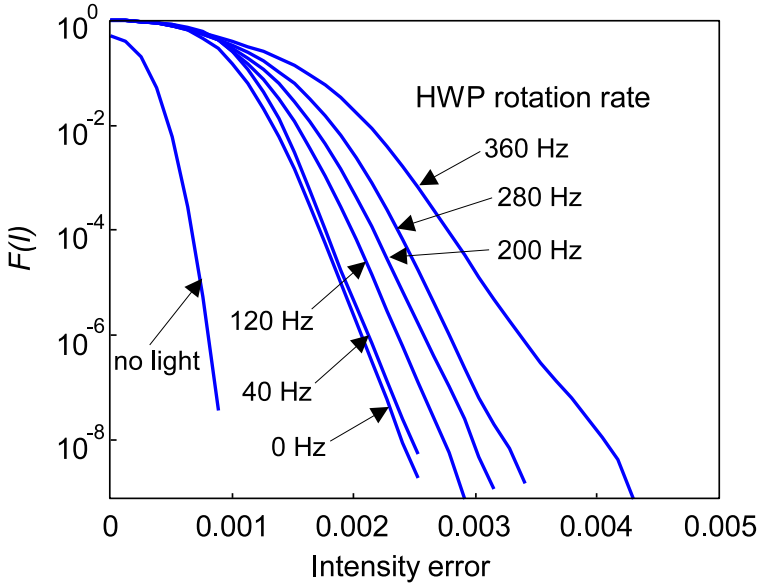

Figure 3.21: Cumulative intensity distribution function during polarization tracking with 3.5 µs iteration time

corresponds to a loss of $-10 \cdot \log(1 - (< 0.0043)) =< 0.019$ dB.

15000 rad/s Tracking Experiment [89]

The fastest version of the software, with only 2 µs iteration time, was tested using the experiment setup. The maximum rotation rate of the half-wave plate was suitable increased to 600 Hz.

Figure 3.23 shows the cumulative density function $F(I)$. For a half-wave rotation of 600 Hz (polarization changes up to 15000 rad/s), again the controller was able to perform tracking with a maximum intensity error of <0.5%. During this 30-minute period, the total accumulated polarization changes is > 20 Mrad. Figure 3.22 shows the intensity error (right scale) and the corresponding calculated polarization error (left scale) displayed as a function of the maximum polarization changes. The mean polarization error was always < 0.061 rad. At 15000 rad/s, the maximum polarization and intensity errors were 0.14 rad and 0.48%, respectively. For the maximized signal exiting at the other PBS output, this corresponds to a loss of $-10 \cdot \log(1 - (< 0.0048)) =< 0.021$ dB.

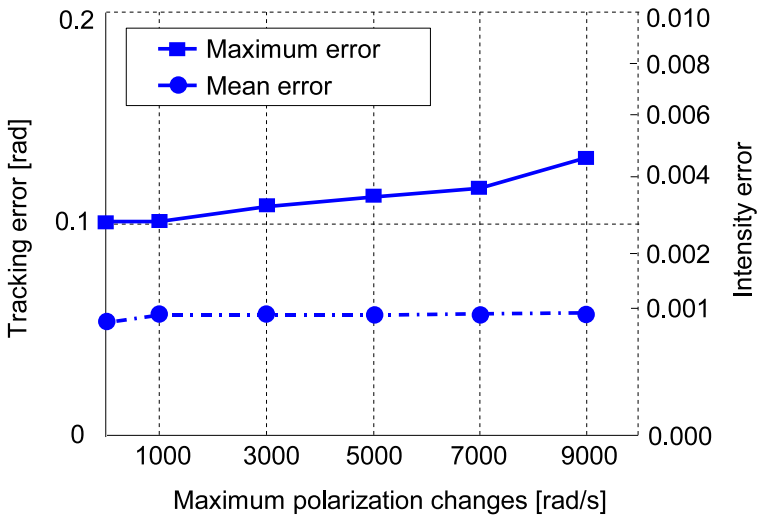

Figure 3.22: Tracking error for different polarization changes (with 3.5 µs control iteration time)

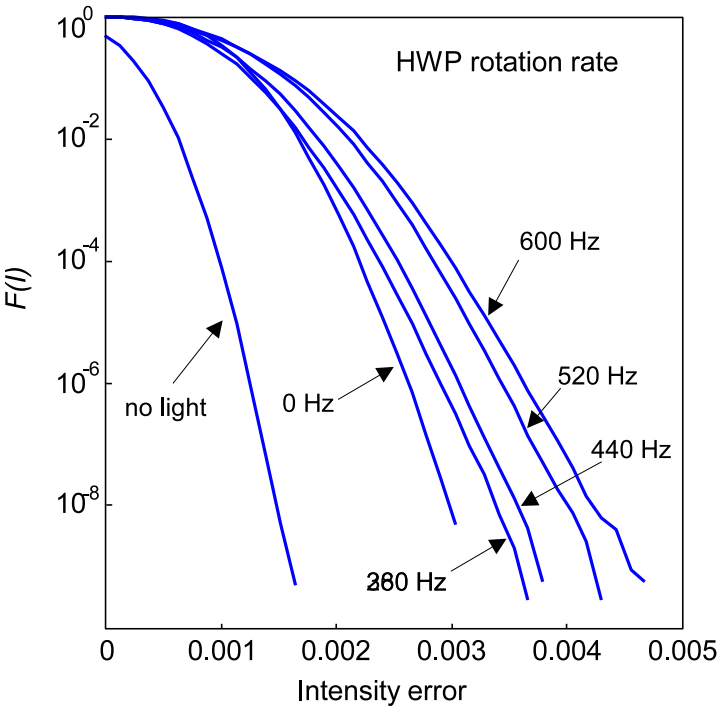

Figure 3.23: Cumulative intensity distribution function during polarization tracking with 2 µs iteration time

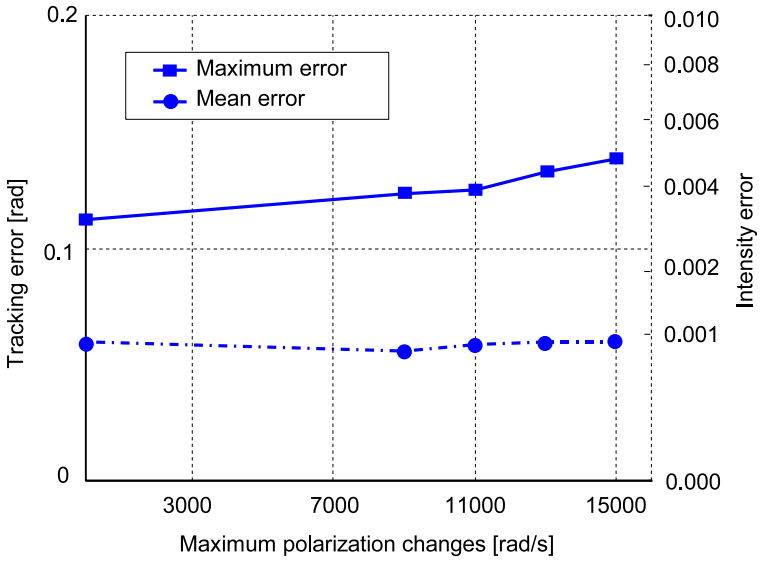

Figure 3.24: Tracking error for different polarization changes (with 2 µs control iteration time)

Chapter 4

Summary

An ultra-fast automatic polarization controller designed for polarization demultiplexing and PMD compensation has been developed in this work. The controller employs commercial electro-optic retarders, runs on an FPGA, tracks the polarization changes endlessly and reaches the control speed of 15000 rad/s.

Retarder Characterization

In Chapter 2, the operating principle of optical retarders is analyzed using quaternion algebra. Specifically, a quaternion model for an electro-optic lithium niobate linear retarder is then formulated. Since commercial retarders might exhibit non-ideal characteristics, a thorough characterization of the retarders is more useful than just a parametric model. During the characterization procedure, a polarimeter is used to record the Stokes parameters for different driving voltages applied to the linear retarder. Using a quaternion-based optimization, the polarization transformation of the retarder can be inferred accurately.

Based on the characterization result, a retarder can be calibrated so that it can be operated as a linear retarder or a fractional waveplate, already taking into account any of retarder's non-ideal characteristics. Later in the polarization controller, the calibration data are entered as look-up tables for very fast access. Because such an electro-optic retarder has a finite response time, a state-space model of the retarder is presented as well. The model parameters are estimated using the subspace identification algorithm.

The extensive use of quaternion analysis for electro-optic retarder characterization and calibration has never been reported before. The state-space modeling and identification have never been attempted either.

Endless Polarization Controller

Chapter 3 starts with a detailed description of the two common polarization control algorithms: the linear retarder algorithm and the cascaded fractional waveplates algorithm. Again, quaternion is used as the tool to analyze the general performance of both algorithms.

Because the aim of this work is to realize the fastest possible polarization controller, a hardware-based digital controller is designed and implemented. The hardware comprises an FPGA with a million gates of logic capability, a high-speed ADC to sample the feedback signal and several DACs to drive the electro-optic retarders. The software is programmed with VHDL, it relies also on the calibration data stored in the memory. The linear retarder algorithm is chosen for the controller. The implementation is highly optimized, achieving a control iteration cycle of only 7 µs. Two faster versions can even run with a control iteration cycle of 3.5 µs and 2 µs. All versions are tested in polarization tracking experiments. A maximum tracking speed of 15000 rad/s is reached. With faster hardware, the tracking speed can be further increased. From the retarder

characterization procedure, non-ideal behavior of the linear retarder was found to be minimum, which made the good experiment results possible.

Compared to any other polarization tracking reports that have been published before, the results presented in this work clearly show that this FPGA-based digital controller is able to track faster polarization changes with much better performance (maximum and mean tracking errors) and guaranteed endless operation. The tracking is recorded and verified for 30 minutes, which is the longest endless polarization control experiment reported to date. The controller only gives a polarization mismatch of at most 0.14 rad on the Poincaré sphere corresponding to a negligible intensity error of only 0.02 dB.

Appendix A

Basic Quaternion Algebra

Quaternion, first devised by Sir William Rowan Hamilton in 1843 [25], is a hyper-complex number of rank 4. The set of all quaternions is a vector space with the dimension of 4 and contains the complex numbers.

A quaternion $\mathcal{Q}$ is represented the scalar part q_0 and the vector part $\mathbf{Q} = \mathbf{i}q_1 + \mathbf{j}q_2 + \mathbf{k}q_3$

$$\mathcal{Q} = q_0 + \mathbf{Q} = q_0 + \mathbf{i}q_1 + \mathbf{j}q_2 + \mathbf{k}q_3 \tag{A.1}$$

with q_0, q_1, q_2, q_3 are all real numbers and $\mathbf{i}, \mathbf{j}, \mathbf{k}$ satisfy

$$\mathbf{i}^2 = \mathbf{j}^2 = \mathbf{k}^2 = \mathbf{ijk} = -1 \tag{A.2}$$

Furthermore, the following *Hamilton's rules* must hold for multiplications of $\mathbf{i}, \mathbf{j}, \mathbf{k}$

$$\mathbf{ij} = \mathbf{k} \qquad \mathbf{ji} = -\mathbf{k} \tag{A.3a}$$
$$\mathbf{jk} = \mathbf{i} \qquad \mathbf{kj} = -\mathbf{i} \tag{A.3b}$$
$$\mathbf{ki} = \mathbf{j} \qquad \mathbf{ik} = -\mathbf{j} \tag{A.3c}$$

The Pauli spin matrices $= \boldsymbol{\sigma} = (\sigma_1, \sigma_2, \sigma_3) = (\begin{bmatrix} 1 & 0 \\ 0 & -1 \end{bmatrix}, \begin{bmatrix} 0 & 1 \\ 1 & 0 \end{bmatrix} \begin{bmatrix} 0 & -\mathbf{i} \\ \mathbf{i} & 0 \end{bmatrix})$ are related to the quaternion elements $\mathbf{i}, \mathbf{j}, \mathbf{k}$ by [90]

$$\mathbf{i} = -i\sigma_1 \tag{A.4a}$$
$$\mathbf{j} = -i\sigma_2 \tag{A.4b}$$
$$\mathbf{k} = -i\sigma_3 \tag{A.4c}$$

A *pure quaternion* is a quaternion whose $q_0 = 0$. A vector $\mathbf{v} \in R^3$, where $\mathbf{v} = (x, y, z)$, can be represented by the pure quaternion $\mathcal{Q} = \mathbf{i}x + \mathbf{j}y + \mathbf{k}z$.

The *complex conjugate* of quaternion $\mathcal{Q}$, denoted $\mathcal{Q}^*$, is given as

$$\mathcal{Q}^* = q_0 - \mathbf{Q} = q_0 - (\mathbf{i}q_1 + \mathbf{j}q_2 + \mathbf{k}q_3) \tag{A.5}$$

The inverse of quaternion $\mathcal{Q}$, denoted $\mathcal{Q}^{-1}$, is the complex conjugate

$$\mathcal{Q}^{-1} = \mathcal{Q}^* \tag{A.6}$$

If c is a scalar, then

$$c\mathcal{Q} = cq_0 + c\mathbf{Q} = cq_0 + \mathbf{i}cq_1 + \mathbf{j}cq + \mathbf{k}cq_3 \tag{A.7}$$

Let quaternions $\mathcal{P}$ and $\mathcal{Q}$

$$\begin{aligned}\mathcal{P} &= p_0 + \mathbf{P} = p_0 + \mathbf{i}p_1 + \mathbf{j}p_2 + \mathbf{k}p_3 \\ \mathcal{Q} &= q_0 + \mathbf{Q} = q_0 + \mathbf{i}q_1 + \mathbf{j}q_2 + \mathbf{k}q_3\end{aligned}$$

then the binary operations of $\mathcal{P}$ and $\mathcal{Q}$ are given as

$$\mathcal{P} + \mathcal{Q} = (p_0 + q_0) + (\mathbf{P} + \mathbf{Q}) \tag{A.8}$$

$$\mathcal{P} - \mathcal{Q} = (p_0 - q_0) + (\mathbf{P} - \mathbf{Q}) \tag{A.9}$$

$$\mathcal{P}\mathcal{Q} = p_0 q_0 - \mathbf{P} \cdot \mathbf{Q} + p_0\mathbf{Q} + q_0\mathbf{P} + \mathbf{P} \times \mathbf{Q} \tag{A.10}$$

The *norm* of quaternion $\mathcal{Q}$, denoted $|\mathcal{Q}|$, is

$$|\mathcal{Q}| = \sqrt{\mathcal{Q}^*\mathcal{Q}} \tag{A.11}$$

$$|\mathcal{Q}|^2 = q_0^2 + q_1^2 + q_2^2 + q_3^2 \tag{A.12}$$

Quaternion $\mathcal{Q}$ is called a *unit quaternion* if $|\mathcal{Q}| = 1$. The product of two or more unit quaternions is always a unit quaternion.

A rotation of θ about the axis presented by the vector $\mathbf{u}$ can be represented by the quaternion

$$\mathcal{Q} = \cos\frac{\theta}{2} + \sin\frac{\theta}{2}\mathbf{u} \tag{A.13}$$

Rotation of a vector $\mathbf{v} \in \boldsymbol{R}^3$ by the unit quaternion $\mathcal{Q}$ gives a vector $\mathbf{w}$ according to

$$\mathbf{w} = \mathcal{Q}\mathbf{v}\mathcal{Q}^* \tag{A.14}$$

The orthogonal matrix corresponding to a rotation by the quaternion $\mathcal{Q}$ is given by

$$\mathbf{G} = \begin{bmatrix} q_0^2 + q_1^2 - q_2^2 - q_3^2 & 2(q_1q_2 - q_0q_3) & 2(q_0q_2 + q_1q_3) \\ 2(q_0q_3 + q_1q_2) & q_0^2 - q_1^2 + q_2^2 - q_3^2 & 2(q_2q_3 - q_0q_1) \\ 2(q_1q_3 - q_0q_2) & 2(q_0q_1 + q_2q_3) & q_0^2 - q_1^2 - q_2^2 + q_3^2 \end{bmatrix} \tag{A.15}$$

The 2×2 complex matrix corresponding to a rotation by the unit quaternion $\mathcal{Q}$ is given by

$$\mathbf{J} = \begin{bmatrix} q_0 + \mathbf{i}q_1 & q_2 + \mathbf{i}q_3 \\ -q_2 + \mathbf{i}q_3 & q_0 - \mathbf{i}q_1 \end{bmatrix} \tag{A.16}$$

Spherical linear interpolation (*slerp*) between $\mathcal{Q}_1$ to $\mathcal{Q}_2$ with a parameter $u = 0 \ldots 1$ can be obtained as [91]

$$slerp(\mathcal{Q}_1, \mathcal{Q}_2; u) = \frac{\sin(1-u)\delta}{\sin\delta}\mathcal{Q}_1 + \frac{\sin u\delta}{\sin\delta}\mathcal{Q}_2 \tag{A.17}$$

where

$$\cos\delta = \mathcal{Q}_1 \cdot \mathcal{Q}_2$$

The result of spherical linear interpolation inherently is always a quaternion, unlike interpolation of two rotation matrices by linear interpolation of the elements which possibly yields a non-orthogonal matrix.

Appendix B

Non-Iterative Solutions for Absolute Orientation Problem

Given two corresponded point sets $\{\mathbf{x}_i\}$ and $\{\mathbf{y}_i\}$, $i = 1..N$, which are N vectors in $\mathbb{R}^3$ arranged in $3 \times N$ matrices, such that they are related by:

$$\mathbf{y}_i = \mathbf{R}\mathbf{x}_i + \mathbf{T} + \mathbf{V}_i \tag{B.1}$$

where $\mathbf{R}$ is a rotation, $\mathbf{T}$ is a translation and $\mathbf{V}_i$ is a noise vector, then the optimal rotation $\hat{\mathbf{R}}$ and translation $\hat{\mathbf{T}}$ can be found by minimizing the *least square error criterion*:

$$\Sigma^2 = \sum_{i=1}^{N} \left| \mathbf{y}_i - \hat{\mathbf{R}}\mathbf{x}_i - \hat{\mathbf{T}} \right|^2 \tag{B.2}$$

This problem is known as the *absolute orientation problem*. It can be solved using iterative methods or non-iterative methods. Two non-iterative closed-form methods, using unit quaternion and matrix analysis, are described below. The unit quaternion method is faster and simpler than the matrix analysis method.

Both of these methods make use the 3×3 correlation matrix defined by:

$$\mathbf{H} = \sum_{i=1}^{N} \mathbf{x}_{c,i} {\mathbf{y}^T}_{c,i} \tag{B.3}$$

with

$$\mathbf{x}_{c,i} = \mathbf{x}_i - \frac{1}{N} \sum_{i=1}^{N} \mathbf{x}_i \tag{B.4}$$

$$\mathbf{y}_{c,i} = \mathbf{y}_i - \frac{1}{N} \sum_{i=1}^{N} \mathbf{y}_i \tag{B.5}$$

Unit Quaternion Method

This method was developed by Horn [92]. Using this method, the rotation and the translation are represented by the unit quaternion $\hat{\mathcal{Q}}$ and the vector T respectively.

Let the correlation matrix $\mathbf{H}$ be written as:

$$\mathbf{H} = \begin{bmatrix} H_{00} & H_{01} & H_{02} \\ H_{10} & H_{11} & H_{12} \\ H_{20} & H_{21} & H_{22} \end{bmatrix}$$

A new 4×4 matrix is first constructed from the correlation matrix $\mathbf{H}$ as:

$$\mathbf{P} = \begin{bmatrix} H_{00}+H_{11}+H_{22} & H_{12}-H_{21} & H_{20}-H_{02} & H_{01}-H_{10} \\ H_{12}-H_{21} & H_{00}-H_{11}-H_{22} & H_{01}+H_{10} & H_{20}+H_{02} \\ H_{20}-H_{02} & H_{01}+H_{10} & H_{11}-H_{00}-H_{22} & H_{12}+H_{21} \\ H_{01}-H_{10} & H_{20}+H_{02} & H_{12}+H_{21} & H_{22}-H_{11}-H_{00} \end{bmatrix} \tag{B.6}$$

The optimal rotation $\hat{\mathcal{Q}}$ is given as the eigenvector corresponding to the largest positive eigenvalue of $\mathbf{P}$.

The optimal translation vector is given as:

$$\hat{\mathbf{T}} = \frac{1}{N}\sum_{i=1}^{N}\mathbf{y}_i - \hat{\mathcal{Q}}\frac{1}{N}\sum_{i=1}^{N}\mathbf{x}_i\hat{\mathcal{Q}}^* \tag{B.7}$$

Matrix Analysis Method

This method was developed by Arun, Huang, and Blostein [93]. Using this method, the rotation and the translation are represented by the 3×3 orthonormal matrix $\hat{\mathbf{R}}$ and the vector T respectively.

From the correlation matrix $\mathbf{H}$, singular value decomposition yields:

$$\mathbf{H} = \mathbf{U} \wedge \mathbf{V} \tag{B.8}$$

The optimal rotation matrix is given as:

$$\hat{\mathbf{R}} = \mathbf{U}\mathbf{V}^{\mathrm{T}} \tag{B.9}$$

The optimal translation vector is given as:

$$\hat{\mathbf{T}} = \frac{1}{N}\sum_{i=1}^{N}\mathbf{y}_i - \hat{\mathbf{R}}\frac{1}{N}\sum_{i=1}^{N}\mathbf{x}_i \tag{B.10}$$

Appendix C

Multichannel Polarization Division Multiplexing Transmissions

The need for an automatic, ultra-fast polarization controller arose from the experiments to push the transmission capacity in an optical communication system. The combination of differential quadrature phase-shift keying (DQPSK) and polarization division multiplexing (PolDM) proves to be an effective way to quadruple the bit rate. At 40 Gbaud, this corresponds to a 160 Gb/s channel capacity. For this modulation format, an automatic polarization demultiplexer at the receiver is necessary. With wavelength division multiplexing (WDM), the total capacity is further multiplied by the number of transmitted channels. Some recent experiments using DQPSK and PolDM that were conducted in a multichannel WDM transmission system are described in this appendix.

Experiment Setup

Figure C.1 shows the transmitter setup. N signals from lasers with 100 GHz frequency spacing are combined with equal polarizations in an optical multiplexer. These WDM channels are modulated together in a dual-drive differential phase-shift keying (DPSK) modulator. The transmitted bits are a non return-to-zero (NRZ) pseudo-random binary sequence (PRBS) data with a periodic bit length of 127. A DQPSK signal is generated by combining the DPSK signal in a fiber-based Mach-Zender delay interferometer (MZDI) with a differential delay of 75 ps (3-symbol durations). The laser frequencies are fine-tuned to an integer multiple of the interferometer delay in order to achieve a proper DQPSK signal in each channel. The return-to-zero (RZ) signal is generated using another dual-drive modulator clocked at 20 GHz that acts as a pulse carver. The PolDM signal is realized by combining two RZ-DQPSK signals with orthogonal polarization. To ensure decorrelation between the two polarization channels, one channel is delayed by 2.8 ns (112-symbol durations) before being recombined with the other one. The optical signal is then amplified and launched to the transmission line.

Figure C.2 shows the receiver setup. The received optical signal from the transmission line is preamplified and then one of the channels is selected using an optical demultiplexer and an optical switch. Per-channel chromatic dispersion compensation is applied before the signal is polarization demultiplexed in a lithium niobate polarization transformer driven by a controller that minimizes the broadband interference between the two polarization channels. The DQPSK signal is demodulated using a fiber-based Mach-Zender interferometer. For proper decoding of in-phase and quadrature data channels, the differential delay of the interferometer is set to $\pi/4$ or $3\pi/4$. The interferometer outputs are connected to the clock and data recovery circuit. The decoded data are analyzed in a bit error rate (BER) tester which is suitably programmed with the expected bit pattern. This receiver setup allows only a measurement of one polarization and one quadrature at a time. Thus, four separate measurements are needed for each WDM channel.

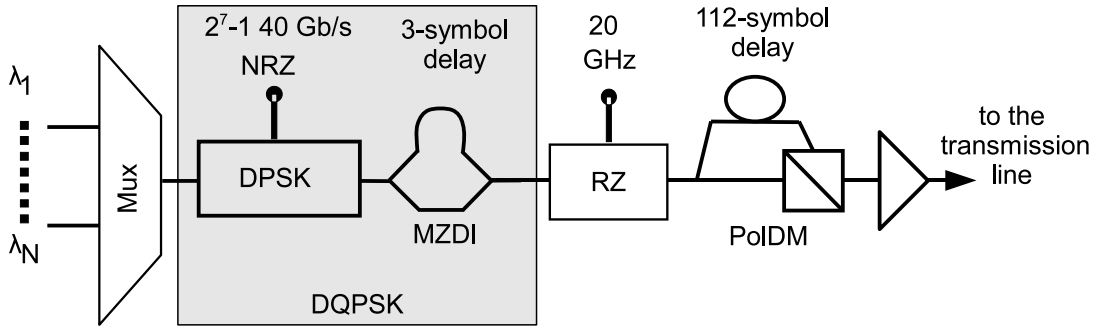

Figure C.1: Setup for the WDM transmitter

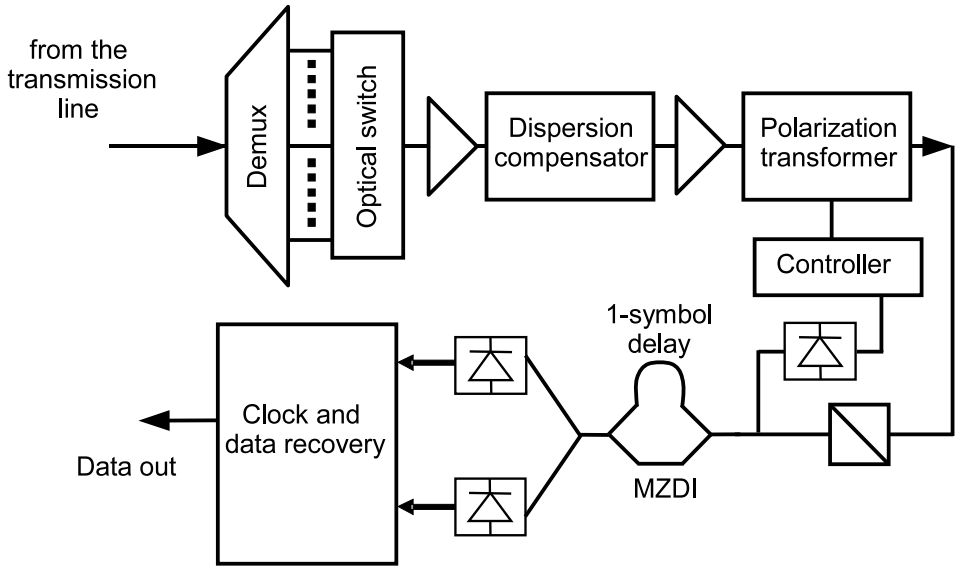

Figure C.2: Setup for the WDM receiver

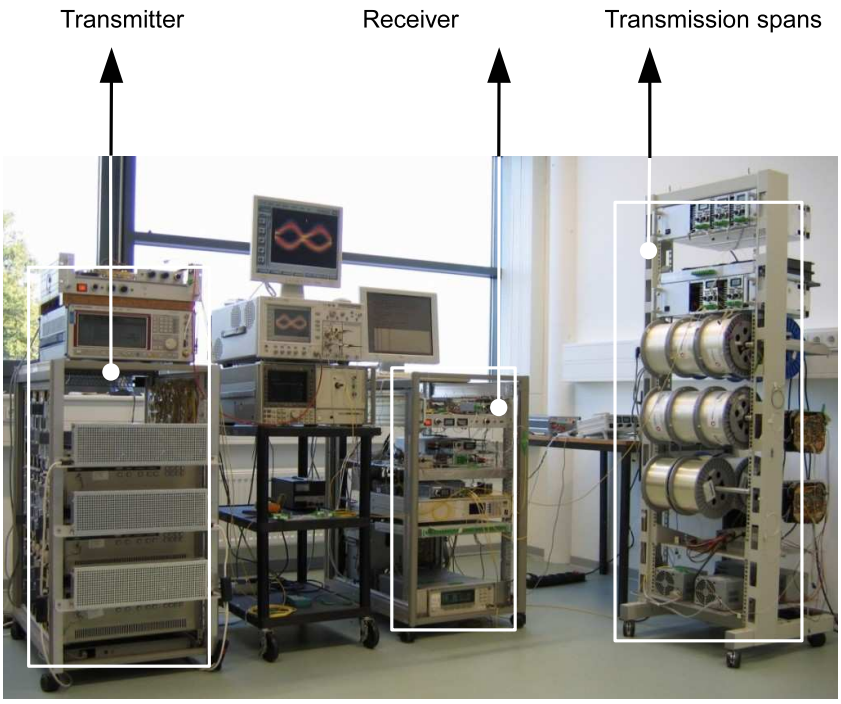

Figure C.3: Picture of the experiment setup

To allow semi-automatic measurement, almost all equipments and instruments are connected to a desktop computer running a control software specifically developed to carry out the following tasks:

- to switch on and off all lasers
- to continuously monitor and adjust the laser frequencies
- to choose one specific WDM channel to measure
- to adjust dispersion compensation applied to the selected WDM channel
- to trigger the clock and data recovery
- to load the received pattern into the BER tester
- to get the BER from the BER tester
- to perform automatic Q-factor and sensitivity measurement

In all cases, polarization control was slow and thus it limits the practical uses of the transmission system outside the laboratory experiments. This shows the need for a a fast automatic polarization controller so that any polarization fluctuations along the transmission line due to the temperature, vibration and other mechanical disturbances on the transmission fiber can be tracked.

Figure C.3 shows the picture of the experiment setup.

Measurement Results

In each experiment, bit error rate (BER) at the receiver was measured for each in-phase/ quadrature and two polarizations data channels, denoted as I/Q and X/Y in the figure. The corresponding Q factor is calculated from the BER with the relation

$$Q = \sqrt{2} \cdot erf^{-1}(1 - 2 \cdot BER) \tag{C.1}$$

In commercially available transmission systems, Forward Error Correcting (FEC) is employed to improve the system performance [94]. In the following experiments, an FEC decoder was assumed to process the raw demodulated data. The net error-free transmission capacity was thus calculated by excluding the FEC overhead. Using the latest generation FEC with 7% redundancy, a corrected BER of $< 10^{-13}$ would be reached with a raw BER of $< 3.9 \cdot 10^{-3}$ [6]. The BER of $3.9 \cdot 10^{-3}$ hereby will be referred as the *FEC limit*.

16 Channels over 273 km Experiment

In this experiment, 16 WDM channels in the range of 192.2 THz to 193.7 THz were launched into a transmission line that comprised 4 fiber spans: 81 km, 69 km, 60 km, and 63 km. Each span had mixed standard single mode fiber (SSMF) and non-zero dispersion shifted fiber (NZDSF). An Erbium-doped fiber amplifier (EDFA) and a dispersion compensating fiber (DCF) were inserted before each span. Figure C.4 shows the measured BERs at the receiver, and the corresponding Q factors, for in-phase/ quadrature at both polarizations. After 273 km a BER $< 8 \cdot 10^{-4}$ (exceeding the FEC limit) was observed in all cases. The total raw transmission capacity was 2.56 Tb/s. A net error-free transmission capacity of 2.38 Tb/s was reached [95].

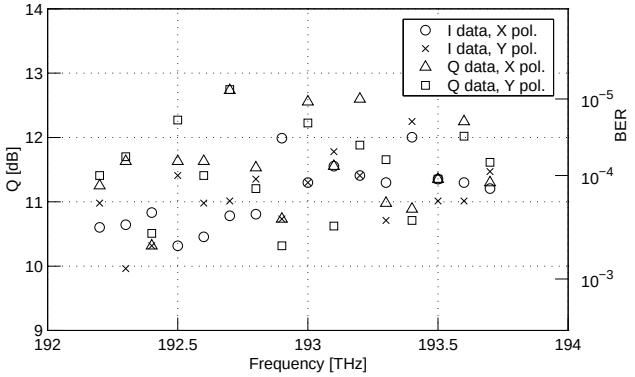

Figure C.4: Measured BER and the corresponding Q-factor as a function of frequency for 16 channels over 273 km experiment

16 Channels over 292 km Experiment

In this experiment, 16 WDM channels in the range of 192.2 THz to 193.7 THz were launched into a transmission line that comprised 3 fiber spans: 101 km, 98 km, and 92 km. DCF and EDFA were inserted before each span. No Raman amplifier was inserted in the fiber span at all. Figure C.5 shows the measured BERs at the receiver, and the corresponding Q factors, for in-phase/ quadrature at both polarizations. After 292 km a BER $< 3 \cdot 10^{-3}$ (exceeding the FEC limit) was observed in all cases. The total raw

transmission capacity was 2.56 Tb/s. A net error-free transmission capacity of 2.38 Tb/s was again reached [96].

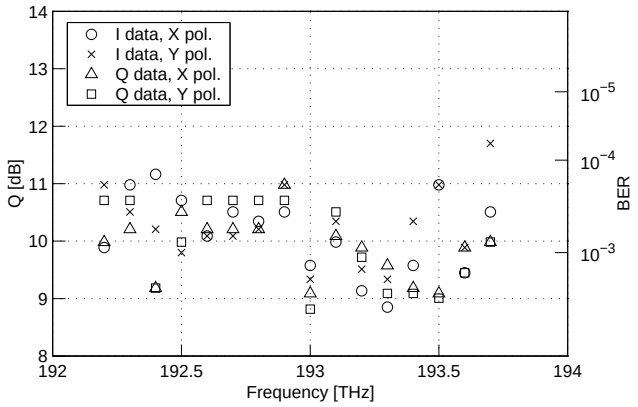

Figure C.5: Measured BER and the corresponding Q-factor as a function of frequency for 16 channels over 292 experiment

32 Channels over 323 km Experiment

In this experiment, 32 WDM channels in the range of 192.1 THz to 195.3 THz were launched into a transmission line that comprised 4 fiber spans: 81 km, 80 km, 82 km and 80 km. DCF and EDFA were inserted in each span. No Raman amplification was used inside the span. Figure C.6 shows the measured BERs at the receiver, and the corresponding Q factors, for in-phase/ quadrature at both polarizations. After 323 km a BER $< 9 \cdot 10^{-4}$ (exceeding the FEC limit) was observed in all cases. The total raw transmission capacity was 5.12 Tb/s. A net error-free transmission capacity of 4.76 Tb/s was reached [97].

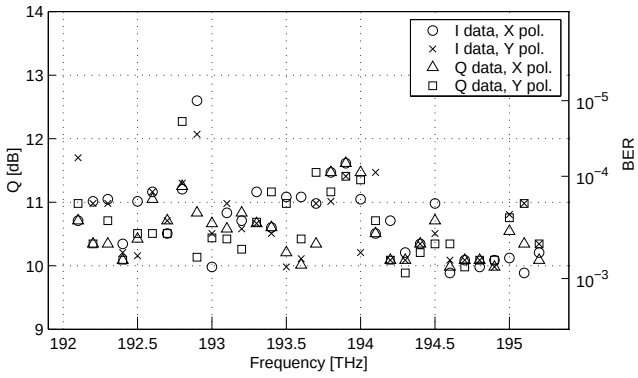

Figure C.6: Measured BER and the corresponding Q-factor as a function of frequency for 32 channels experiment

40 Channels over 324 km Experiment

In this experiment, 40 WDM channels in the range of 192.1 THz to 196.0 THz were were launched into a transmission line that comprised 4 fiber spans: 81 km, 80 km, 82 km and 81 km. DCF was inserted in the span right before EDFA. Additionally, a backward-pumped Raman amplifier in each span was used to reduce the span loss. Figure C.7

shows the measured BERs at the receiver, and the corresponding Q factors, for in-phase/ quadrature at both polarizations. After 324 km a BER $< 8 \cdot 10^{-4}$ (exceeding the FEC limit) was observed in all cases. The total raw transmission capacity was 6.4 Tb/s. A net error-free transmission capacity of 5.94 Tb/s was reached. The same setup was also successfully used to test a commercial fiber Bragg grating multichannel dispersion compensator [98, 99].

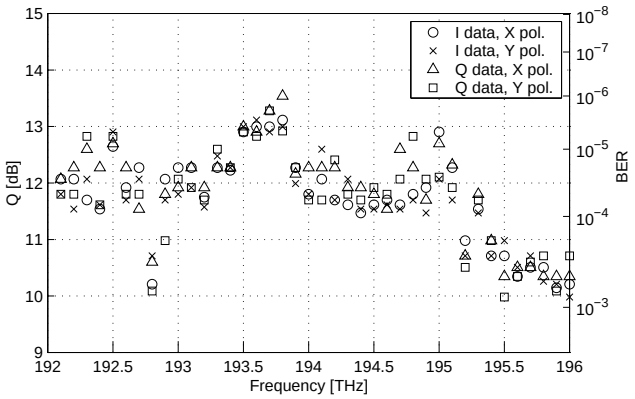

Figure C.7: Measured BER and the corresponding Q-factor as a function of frequency for 40 channels experiment

Bibliography

[1] G. Agrawal, *Fiber Optic Communication System, 2nd Edition.* John Wiley Sons, 1997.

[2] K. Fukuchi, T. Kasamatsu, M. Morie, R. Ohhira, T. Ito, K. Sekiya, D. Ogasahara, and T. Ono, "10.92 Tb/s (273 × 40-Gb/s) triple-bandultra-dense WDM optical-repeatered transmission experiment," in *Proceedings of the Optical Fiber Communication Conference (OFC 2001), Anaheim, USA*, 2001, Paper PD24-1.

[3] R. A. Griffin and A. C. Carter, "Optical differential quadrature phase-shift key (oDQPSK) for high capacity optical transmission," in *Proceedings of the Optical Fiber Communication Conference (OFC 2002), Anaheim, USA*, pp. 367–368, Paper WX6.

[4] A. Gnauck and P. Winzer, "Optical phase-shift keyed transmission," *Journal of Lightwave Technology*, vol. 23, no. 1, January 2005.

[5] K. Ho, *Phase-Modulated Optical Communication Systems.* Springer, 2005.

[6] G. Charlet, P. Tran, H. Mardoyan, M. Lefrancois, T. Fauconnier, F. Jorge, and S. Bigo, "151×43 Gb/s over 4,080km based on return-to-zero differential quadrature phase-shift keying," in *Proceedings of European Conference on Optical Communication (ECOC 2006), Nice, France*, 2006, Paper Th4.1.3.

[7] P. M. Hill and R. Olshansky, "Optical polarization division multiplexing at 4Gb/s," *IEEE Photonics Technology Letters*, vol. 4, no. 5, pp. 500–502, May 1992.

[8] R. Noe, D. Sandel, and F. Wüst, "Polarization mode dispersion tolerance of bandwidth-efficient multilevel modulation schemes," in *Proceedings of the Optical Fiber Communication Conference (OFC 2000), Anaheim, USA*, paper WL4.

[9] C. Wree, N. Hecker-Denschlag, E. Gottwald, P. Krummrich, J. Leibrich, E.-D. Schmidt, B. Lankl, and W. Rosenkranz, "High spectral efficiency 1.6-b/s/Hz transmission (8×40 Gb/s with a 25-GHz grid) over 200-km SSMF using RZ-DQPSK and polarization-multiplexing," *IEEE Photonics Technology Letters*, vol. 15, no. 9, pp. 1303–1305, 2003.

[10] B. Milivojevic, A. F. Abas, A. Hidayat, S. Bhandare, D. Sandel, R. Noé, M. Guy, and M. Lapointe, "1.6-b/s/Hz 160-Gb/s 230-km RZ-DQPSK polarization multiplex transmission with tunable dispersion compensation," *IEEE Photonics Technology Letters*, vol. 17, no. 2, pp. 495–497, 2005.

[11] A. Gnauck, G. Charlet, P. Tran, P. Winzer, C. Doerr, J. Centanni, E. Burrows, and T. Kawanishi, "25.6-Tb/s C+L-band transmission of polarization-multiplexed RZ-DQPSK signals„" in *Proceedings of the Optical Fiber Communication Conference (OFC 2007), Anahaim, USA*, 2007, Paper PDP19.

[12] S. Ryu, *Coherent Lightwave Communication Systems.* Artech House, 1995.

[13] R. Noe, H. J. Rodler, A. Ebberg, G. Gaukel, B. Noll, J. Wittmann, and F. Auracher, "Comparison of polarization handling methods in coherent optical systems," *Journal of Lightwave Technology*, vol. 9, no. 10, pp. 1353–1366, 1991.

[14] P. J. Winzer, G. Raybon, and M. Duelk, "107-Gb/s optical ETDM transmitter for 100G Ethernet transport," in *Proceedings of European Conference on Optical Communication (ECOC 2005), Glasgow, United Kingdom*, 2005, paper Paper Th4.1.1.

[15] J. P. Gordon and H. Kogelnik, "PMD fundamentals: Polarization mode dispersion in optical fibers," in *Proceedings of the National Academy Sciences USA*, vol. 97, pp. 4541–4550.

[16] R. Noé, "In-service PMD monitoring and compensation," in *Proceedings of Ninth Optoelectronics and Communications Conference/Third International Conference on Optical Internet (OECC/COIN 2004), Yokohama, Japan*, 2004, Tutorial 14C2.1.

[17] R. Noé, D. Sandel, S. Hinz, M. Yoshida-Dierolf, V. Mirvoda, G. Feise, H. Herrmann, R. Ricken, W. Sohler, F. Wehrmann, C. Glingener, A. Schöplin, A. Färbert, and G. Fischer, "Integrated optical $LiNbO_3$ distributed polarisation mode dispersion compensator in 20Gbit/s transmission system," *Electronics Letters*, vol. 35, no. 8, 1999.

[18] P. M. Krummrich and K. Kotten, "Extremely fast (microsecond timescale) polarization changes in high speed long haul WDM transmission systems," in *Proceedings of the Optical Fiber Communication Conference (OFC 2004), Los Angeles, USA*, February 2004.

[19] P. M. Krummrich, E. D. Schmidt, W. Weiershausen, and A. Mattheus, "Field trial results on statistics of fast polarization changes in long haul WDM transmission systems," in *Proceedings of the Optical Fiber Communication Conference (OFC 2005), Annaheim, USA*, March 2005.

[20] R. Noé, "Optische Nachrichtentechnik," 2001, Lecture Notes, Dept. of Electrical Engineering, University of Paderborn.

[21] R. C. Jones, "A new calculus for the treatment of optical systems (part 1)," *Journal of Optical Society of America*, vol. 31, pp. 488–503, 1941.

[22] G. G. Stokes, "On the composition and resolution of streams of polarized light from different sources," *Transactions of the Cambridge Philosophical Society*, vol. 9, pp. 399–416, 1852.

[23] H. Mueller, "The foundation of optics," *Journal of Optical Society of America*, vol. 38, p. 661, 1948.

[24] H. G. Jerrard, "Transmission of light through birefringent and optically active media: the poincaré sphere," *Journal of Optical Society of America*, vol. 44, no. 8, pp. 634–640, 1954.

[25] W. R. Hamilton, *Elements of quaternions*, 3rd ed. Chelsea Publishing Company, 1969.

[26] C. Huygens, *Treatise on light*, english translation ed. University of Chicago Press, 1950.

[27] A. Bravais, "Description d'un nouveau polariscope, et recherches sur des doubles réfractions peu énergiques," *Comptes Rendus Hebdomadaires des Seances de l'Academie des Sciences*, vol. 32, pp. 115–, 1851.

[28] Soleil, "Nouvel appareil propre a la mesure des deviations dans les expériences de polarisation rotatorie," *Comptes Rendus Hebdomadaires des Seances de l'Academie des Sciences*, vol. 21, pp. 426–427, 1846.

[29] H. G. Jerrard, "Optical compensators for measurement of elliptical polarization," *Journal of Optical Society of America*, vol. 38, no. 1, pp. 35–59, 1948.

[30] M. Johnson, "In-line fiber-optical polarization transformer," *Applied Optics*, vol. 18, no. 9, pp. 1288–1289, 1979.

[31] H. C. Levefre, "Single-mode fibre fractional wave devices and polarisation controller," *Electronics Letters*, vol. 16, no. 20, pp. 778–780, 1980.

[32] S. Thaniyavarn, "Wavelength independent, optical damage immune z-propagation $LiNbO_3$ waveguide polarization converter," *Applied Physics Letters*, vol. 47, no. 7, pp. 674–677, 1985.

[33] H.Heidrich, C. von Helmolt, D. Hoffmann, H.-J. Hensel, and A. Kleinwaechter, "Polarisation transformer on $Ti : LiNbO_3$ with reset-free optical operation for heterodyne/homodyne receivers," *Electronics Letters*, vol. 23, no. 7, pp. 335–336, 1987.

[34] R. Noé, D. Sandel, and V. Mirvoda, "PMD in high-bit-rate transmission and means for its mitigation," *IEEE Journal of Selected Topics in Quantum Electronics*, vol. 10, no. 2, March/April 2004.

[35] A. van Haasteren, J. van der Tol, O. van Deventer, and H. Frankena, "Modeling and characterization of an electrooptic polarization controller on $LiNbO_3$," *Journal of Lightwave Technology*, vol. 11, no. 7, pp. 1151–1157, 1993.

[36] N. G. Walker and G. R. Walker, "Polarization control for coherent communications," *Journal of Lightwave Technology*, vol. 8, no. 3, pp. 438–458, 1990.

[37] J. Kennedy and R. Eberhart, "Particle swarm optimization," in *Proceeding of IEEE International Conference on Neural Networks 1995, Perth, Australia*, vol. 4, 1995, pp. 1942–1948.

[38] D. Sandel and R. Noé, "Truly endless polarization control with I & Q mode converter in X-cut, Y-propagation lithium niobate," in *Proceedings of the European Conference on Optical Communication (ECOC 2003), Rimini, Italiy*, 2003.

[39] R. Kalman, "A new approach to linear filtering and prediction problems," *Transactions of the ASME: Journal of Basic Engineering*, vol. 1960, pp. 35–45, March 1960.

[40] R. Noé, H. Heidrich, and D. Hoffmann, "Automatic endless polarization control with integrated-optical $Ti : LiNbO_3$ polarization transformers," *Optics Letters*, vol. 12, no. 6, pp. 527–529, 1988.

[41] L. Ljung, *System Identification: Theory for the User*. Prentice-Hall, 1999.

[42] P. V. Overschee and B. D. Moor, "N4SID - subspace algorithms for the identification of combined deterministic-stochastic systems," *Automatica*, vol. 30, no. 1, pp. 75–94, 1994.

[43] ——, *Subspace Identification for linear systems: Theory - Implementation - Applications*. Kluwer Academic Publishers, 1996.

[44] R. Ulrich, "Polarization stabilization on single-mode fiber," *Applied Physics Letters*, vol. 35, no. 11, pp. 840–842, 1979.

[45] Y. Kidoh, Y. Suematsu, and K. Furuya, "Polarization control on output of single-mode optical fibers," *Journal of Quantum Electronics*, vol. 17, no. 6, pp. 991–994, 1981.

[46] T. Imai, K. Nosu, and H. Yamaguchi, "Optical polarization control utilising an optical heterodyne detection scheme," *Electronics Letters*, vol. 21, pp. 52–53, 1985.

[47] R. Noé, "Endless polarisation control in coherent optical communications," *Electronics Letters*, vol. 22, no. 15, pp. 772–773, 1986.

[48] F. Heismann, P. B. Hansen, S. K. Korotky, G. Raybon, J. J. Veselka, and M. S. Whalen, "Automatic polarization demultiplexer for polarization-multiplexed transmission systems," *Electronics Letters*, vol. 29, no. 22, pp. 1965–1966, 1993.

[49] S. Hinz, D. Sandel, R. Noé, and F. Wüst, "Optical NRZ 2×10 Gb/s polarization division multiplex transmission with endless polarization control driven by correlation signals," *Electronics Letters*, vol. 16, no. 36, pp. 1402–1403, 2000.

[50] S. Hinz, D. Sandel, F. Wüst, and R. Noé, "Polarization multiplexed 2×10 Gb/s RZ transmission using interference detection," in *Proceedings of the Optical Fiber Communication Conference (OFC) 2003, Atlanta, USA*, March 2001.

[51] R. Noé, "Endless polarisation control experiment with three elements of limited birefringence range," *Electronics Letters*, vol. 22, no. 25, pp. 1341–1343, 1986.

[52] N. G. Walker and G. R. Walker, "Endless polarization control using four fibre squeezers," *Electronics Letters*, vol. 23, no. 6, pp. 290–292, 1987.

[53] M. Kubota, T. Oohara, K. Furuya, and Y. Suematsu, "Electro-optical polarisation control on single-mode optical fibres," *Electronics Letters*, vol. 16, no. 15, p. 573, 1980.

[54] F. Heismann and R. C. Alferness, "Wavelength-tunable electrooptic polarization conversion in birefrigent waveguides," *Journal of Quantum Electronics*, vol. 24, no. 1, pp. 83–93.

[55] F. Heismann, "Integrated-optic polarization transformer for reset-free endless polarization control," *Journal of Quantum Electronics*, vol. 25, no. 8, pp. 1898–1906.

[56] S. H. Rumbaugh, M. D. Jones, and L. W. Casperson, "Polarization control for coherent fiber-optic systems using nematic liquid crystals," *Journal of Lightwave Technology*, vol. 8, no. 3, pp. 459–465, 1990.

[57] D. Sandel, S. Hinz, M. Yoshida-Dierolf, J. Gräser, R. Noé, L. Beresnev, T. Weyrauch, and W. Haase, "10-Gb/s PMD compensation using deformed-helical ferrorelectric liquid crystals," in *Proceedings of the European Conference on Optical Communication (ECOC 1998), Madrid, Spain*, 1998, pp. 555–556.

[58] T. Chiba, Y. Ohtera, and S. Kawakami, "Polarization stabilizer using liquid crystal rotatable waveplates," *Journal of Lightwave Technology*, vol. 17, no. 5, pp. 885–890, 1999.

[59] T. Saitoh and S. Kinugawa, "Magnetic field rotating-type faraday polarization controller," *IEEE Photonics Technology Letters*, vol. 15, no. 10, pp. 1404–1406.

[60] J. Prat, J. Comellas, and G.Junyent, "Experimental demonstration of an all-fiber endless polarization controller based on faraday rotation," *IEEE Photonics Technology Letters*, vol. 12, no. 7, pp. 1430–1432, 1995.

[61] *A3000 Polarization Controller*, Adaptif Photonics GmbH, retrieved November 2007. [Online]. Available: http://www.adaptifphotonics.com/Download/ProductInfo/Adaptif_Flyer3000.pdf

[62] *NRT: Polarization Controller Development Platform*, New Ridge Technologies, retrieved October 2007. [Online]. Available: http://www.newridgetech.com/html/polcon.html

[63] R. Noé, "Entwurf und Aufbau von unterbrechungsfreien Polarisationsnachführungen im optischen überlagerungsempfang," Ph.D. dissertation, Technical University of Munich, Germany, 1987.

[64] L. J. Rysdale, "Method of overcoming finite-range limitation of certain state of polarisation control devices in automatic polarisation control schemes," *Electronics Letters*, no. 2, pp. 100–103, 1986.

[65] R. Noé, D. Sandel, M. Yoshida-Dierolf, S. Hinz, V. Mirvoda, A. Schöpflin, C. Glingener, E. Gottwald, C. Scheerer, G. Fischer, T. Weyrauch, and W. Haase, "Polarization mode dispersion compensation at 10, 20, and 40 Gb/s with various optical equalizers," *Journal of Lightwave Technology*, vol. 17, no. 9, pp. 1602–1616, Sep 1999.

[66] P. Oswald and C. K. Madsen, "Deterministic analysis of endless tuning of polarization controllers," *Journal of Lightwave Technology*, vol. 24, no. 7, pp. 2932–2939, July 2006.

[67] R. Noé, H. Heidrich, and D. Hoffmann, "Endless polarization control systems for coherent optics," *Journal of Lightwave Technology*, vol. 6, no. 7, pp. 1199–1208, 1988.

[68] N. G. Walker, G. R. Walker, and J. Davidson, "Endless polarisation control using an integrated optic lithium niobate device," *Electronics Letters*, vol. 24, no. 5, pp. 266–268, 1988.

[69] F. Heismann, "Analysis of a reset-free polarization controller for fast automatic polarization stabilization in fiber-optic transmission systems," *Journal of Lightwave Technology*, vol. 12, no. 4, pp. 690–699, 1994.

[70] M. Martinelli and R. A. Chipman, "Endless polarization control algorithm using adjustable linear retarders with fixed axes," *Journal of Lightwave Technology*, vol. 21, no. 9, pp. 2089–2096, 2003.

[71] C. K. Madsen, P. Oswald, M. Cappuzzo, E. Chen, L. Gomez, A. Griffin, A. Kasper, E. Laskowski, L. Stulz, and A. Wong-Foy, "Reset-free integrated polarization controller using phase shifters," *IEEE Journal of Selected Topics in Quantum Electronics*, vol. 11, no. 2, pp. 431–438, 2005.

[72] F. Heismann and M. S. Whalen, "Broadband reset-free automatic polarisation controller," *Electronics Letters*, vol. 27, no. 4, pp. 377–379, 1991.

[73] ——, "Fast automatic polarization control system," *IEEE Photonics Technology Letters*, vol. 4, no. 5, pp. 503–505, May.

[74] H.Heidrich, D. Hoffmann, C. von Helmolt, and H.Ahlers, "Lithium niobate guided-wave network for a coherent receiver," *Optics Letters*, vol. 14, pp. 99–101, 1989.

[75] W. Shieh and H. Kogelnik, "Dynamic eigenstates of polarization," *IEEE Photonics Technology Letters*, vol. 13, no. 1, pp. 40–42, January 2001.

[76] *Spartan-3 FPGA Family: Complete Data Sheet*, Xilinx, Inc., January 2005. [Online]. Available: http://direct.xilinx.com/bvdocs/publications/ds099.pdf

[77] *Application Note 464: Using Look-Up Tables as Distributed RAM in Spartan-3 Generation FPGAs*, Xilinx, Inc., 2005. [Online]. Available: http://direct.xilinx.com/bvdocs/appnotes/xapp464.pdf

[78] *Application Note 463: Using Block RAM in Spartan-3 Generation FPGAs*, Xilinx, Inc., 2005. [Online]. Available: http://direct.xilinx.com/bvdocs/appnotes/xapp463.pdf

[79] *Application Note 467: Using Embedded Multipliers in Spartan-3 FPGAs*, Xilinx, Inc., May 2003. [Online]. Available: http://direct.xilinx.com/bvdocs/appnotes/xapp467.pdf

[80] *XSA-3S1000 Board V1.1: User Manual*, XESS Corporation, September 2007. [Online]. Available: http://xess.com/manuals/xsa-3S-manual-v1_1.pdf

[81] *256 Mb E-die SDRAM Specification*, Samsung Corporation, May 2004.

[82] *S29AL016M 16 Megabit 3.0 Volt-only Boot Sector Flash Memory*, Spansion Corporation, April 2004. [Online]. Available: http://www.amd.com/us-en/assets/content_type/white_papers_and_tech_docs/S29AL016M.pdf

[83] *XSA Board SDRAM Controller*, XESS Corporation, July 2005. [Online]. Available: http://www.xess.com/appnotes/an-071205-xsasdramcntl.pdf

[84] B. Koch, "FPGA-basiertes Polarisationsregelsystem," Diploma thesis, Department of Electrical Engineering, University of Paderborn, Germany, 2007.

[85] J. S. Liptay, "Structural aspects of the System/360 Model 85, Part II: The cache," *IBM Systems Journal*, vol. 7, no. 1, pp. 15–21, 1968.

[86] A. Hidayat, B. Koch, V. Mirvoda, H. Zhang, S. Bhandare, S. Ibrahim, D.Sandel, and R. Noé, "Fast optical endless polarization tracking with $LiNbO_3$ component," in *Proceedings of the Optical Fiber Communication Conference (OFC 2008), San Diego, USA*, February 2008.

[87] A. Hidayat, B. Koch, V. Mirvoda, H. Zhang, M. Lichtinger, D.Sandel, and R. Noé, "Optical 5 krad/s endless polarisation tracking," *Electronics Letters*, vol. 44, no. 8, pp. 546–548, 2008.

[88] B. Koch, A. Hidayat, H. Zhang, V. Mirvoda, M. Lichtinger, D. Sandel, and R. Noé, "Optical endless polarization stabilization at 9 krad/s with FPGA-based controller," *IEEE Photonics Technology Letters*, vol. 20, no. 12, pp. 961–963, 2008.

[89] ——, "FPGA-basierte schnelle endlose Polarisationsregelung mit Lithiumniobatbauelement," in *ITG-Fachtagung Photonische Netze, Leipzig, Germany*, April 2008.

[90] M. Karlsson, "Quaternion approach to PMD and PDL phenomena in optical fiber systems," *Journal of Lightwave Technology*, vol. 22, no. 4, pp. 1137–1146, 2004.

[91] K. Shoemake, "Animating rotation with quaternion curves," in *Proceedings of the 12th annual conference on Computer graphics and interactive techniques*, 1985, pp. 245–254.

[92] B. K. P. Horn, "Closed-form solution of absolute orientation using unit quaternions," *Journal of Optical Society of America*, vol. 4, no. 4, pp. 629–633, April 1987.

[93] K. Arun, T. Huang, and S. D. Blostein, "Least-squares fitting of two 3-D point sets," in *IEEE Transactions on Pattern Analysis and Machine Intelligence*, vol. 9, no. 5, 1987, pp. 698–700.

[94] T. Mizuochi, "Forward error correction in optical communication systems," in *Proceedings of the European Conference on Optical Communication (ECOC 2007), Berlin, Germany*, 2007, Tutorial Mo 2.2.1.

[95] A. F. A. Ismail, D. Sandel, A. Hidayat, B. Milivojevic, S. Bhandare, H. Zhang, and R. Noé, "2.56 Tbit/s, 1.6 bit/s/Hz, 40 Gbaud RZ-DQPSK polarization division multiplex transmission over 273 km of fiber," in *Proceedings of Ninth Optoelectronics and Communications Conference/Third International Conference on Optical Internet (OECC/COIN 2004), Yokohama, Japan*, 2004, Paper PD1-4.

[96] A. F. Abas, A. Hidayat, D. Sandel, S. Bhandare, and R. Noé, "2.38 Tb/s (16×160 Gb/s) WDM transmission over 292 km of fiber with 100 km EDFA-spacing and no Raman amplification," in *Proceedings of the European Conference on Optical Communication (ECOC 2006), Nice, France*, 2006, Paper Tu1.5.2.

[97] A. F. Abas, "Chromatic dispersion compensation in 40 Gbaud optical fiber WDM phase-shift-keyed communication systems," Ph.D. dissertation, University of Paderborn, Germany, 2006.

[98] A. Hidayat, A. F. Abas, D. Sandel, S. Bhandare, H. Zhang, F. Wüst, B.Milivojevic, R. Noé, M. Lapointe, Y. Painchaud, and M. Guy, "5.94 Tb/s capacity of a multichannel tunable -700 to -1200 ps/nm dispersion compensator," in *Proceedings of European Conference on Optical Communication (ECOC 2005), Glasgow, United Kingdom*, 2005, Paper We1.2.5.

[99] A. Hidayat, A. Abas, D. Sandel, S. Bhandare, H. Zhang, F. Wüst, B. Milivojevic, R. Noé, M. Lapointe, Y. Painchaud, and M. Guy, "5.94 Tb/s capacity of a multi-channel tunable -700 to -1200 ps/nm dispersion compensator," *Journal of Optical Communications*, vol. 27, no. 1, pp. 17–19, 2006.

Acknowledgement

In the name of God, Most Gracious, Most Merciful

I would like to thank Prof. Dr.-Ing. Reinhold Noé who has accepted me five years ago to carry out my doctorate research in his research group. He has been very helpful since the beginning; his insights, supervision, and guidance have been very important for me throughout the course of this work. I would also like to thank Prof. Dr.-Ing. Rolf Schuhmann for acting as a second reviewer and for Prof. Dr.rer.nat. Franz Josef Rammig, Prof. Dr.-Ing. Ulrich Rückert, Prof. Dr.-Ing. Andreas Thiede, and Prof. Dr. Wolfgang Sohler for being in my examination committee.

I am also grateful to all of my research colleagues and the technical staff at the research group of Optical Communications and High Frequency Engineering for the enormous help I received during my stay. I would also like to express my gratitude to all the staff of the International Graduate School "Dynamic Intelligent Systems" for their indispensable support.

Last but not least, special thanks to my family and my friends for their constant love and encouragement.